The Focal Reducing Imager and Spectrograph F O R S ,
built for the optical 16-metre 'Very Large Telescope'
of the 'European Southern Observatory'

Vorgelegt von
Harald Nicklas
aus Prüm

Göttingen 2005

D 7

Referent: Prof. Dr. Klaus Fricke

Korreferent: Prof. Dr. Ralf Bender

Tag der mündlichen Prüfung: 04. Juli 2005

ABSTRACT

This thesis describes the opto- and electro-mechanical concept of a modern astronomical spectrograph with imaging capabilities as it is realised in the *ultraviolet-visual FOcal Reducer / low dispersion Spectrograph* – FORS. The focal reducing optics reimages the telescopic focal plane onto the CCD detector with a demagnification that is required to match the detector's pixel size with the natural stellar seeing disk. This focal reducer is converted from an imaging photometer into a spectrometer by inserting dispersive optical elements between collimator and camera optics into the parallel beam.

FORS became the very first instrument at the optical 16–m 'Very Large Telescope' of the European Southern Observatory. The four 8–m telescopes of the VLT have turned meanwhile into a world-class observatory on the 2 600 m high Paranal mountain in the coastal range of Northern Chile. The FORS imager and spectrograph is realised in two copies FORS1 and -2 for the Cassegrain foci of the VLT unit telescopes Antu (UT1) and Kueyen (UT2) which offer the deepest look from earth into space due to its optics layout, the focus position in lack of a prime focus and the supreme site conditions.

The FORS imager and spectrographs are multi-mode instruments offering up to ten different observing modes in numerous configurations. Direct imaging as well as spectroscopy are the prime modes. Additionally, the FORS instruments - located at the Cassegrain foci - offer the only opportunity at the VLT for linear and circular polarimetry as well as spectro-polarimetry. Due to the multi-purpose observational applications and functions, the imager and spectrographs have become a 3 m large instrument of 2 metric tonnes. Their position at the Cassegrain focus requires special solutions in structural stiffness due to the slew range and aspect angle change in the gravitational field during tracking on celestial objects.

The thesis will give the scientific rationale for building such instruments. It describes the conceptual design in order to solve the specific problems of this kind of imager and spectrograph. It covers the construction, realization and the results of testing thoroughly the instrument mechanics. Those were performed with the aid of a telescope and star simulator and later confirmed through its performance at the real telescope.

The thesis addresses as well the scientific aims and programmes that followed the *1st Scientific Light* of the ESO-VLT in the night of September 15th, 1998. One science programme, called the FORS DEEP FIELD, became common to all three partner institutions of the 'VLT Instrument Consortium'. The program was performed during the 'Guaranteed Observing Time' period to get answers on the tantalizing question; *how the universe looked like when it was still very young during the period of galaxy formation* which probably could be answered at least partially by the combination of the new powerful telescopes with high-performance instruments. Both machines appeared adequate in performing such a programme by taking very deep images and follow-up spectrograms.

FORS also stands for an ambitious project, performed by a consortium of three astronomical institutes in Germany, namely the University Observatories of Göttingen and München and the State Observatory Heidelberg. Building the workhorse for the new astronomical observatory of the European Astronomical Community put a heavy load of responsibility onto the consortium. The enormous effort in designing, constructing, testing and installing the two copies at the VLT amounts to about 180 man-years, equivalent to about 12 Million EURO including all the hardware costs.

Contents

List of Figures

List of Tables

.

Chapter 1

Introduction

The development of today's large telescopes and of modern electronic detectors is running diametrically. The size of the optical telescopes, that determines the light collecting power, is growing since its invention by Galileo. Contrary to the growing diameter of the primary mirrors with ever larger imaging scales, the linear size of the resolution elements of modern electronic CCD detectors is getting smaller and smaller due to the technical progress of integrating the circuits to higher and higher degree and the requests by commercial markets. Therefore, the main problem in imaging the sky directly onto a detector is matching the telescope's imaging scale with the detector's resolution element. Solving this matching problem ensures the most efficient use of the light that is collected by the expensive telescopes and leads to maximum sensitivity for the combined system of a) gathering and b) analysing optics. Matching will result in maximum depth of penetration into space that can be reached with today's technology.

Since the detector's pixel size is fixed and too small for the focal length of modern telescopes at the given 1/2 arcsec image blur due to atmospheric seeing, one has to adapt the telescopic image scale by auxiliary optics. Designed in the right way, this optics will simultaneously correct telescopic aberrations and allow for analysing the incoming light in a spectral and/or in a polarizing sense. Those spectrographs are often called 'focal reducer' because they match the imaging scale by reducing the focal length of the telescope. The first proposal for building a focal reducer with an afocal design was given by Meinel [1] in the year 1956 in order to obtain a large field of view for the given size of the old photographic plates, not for solving the matching problem. Later, a focal reducing system for imaging purposes was build for almost every large optical telescope.

In 1987, the Council of the 'European Southern Observatory' – established 1962 in order to operate an astronomical observatory in the southern hemisphere and supported by eight countries – decided to build the world's largest optical telescope. The effort that the European astronomical community spend in setting-up this world leading facility became similar to the struggling of the astronomers and engineers in building the Palomar two-hundred-inch telescope [2]. The VLT project was like constructing the Palomar telescope 50 years ago that became a real success. Two years after the council's decision, a call for proposals followed for equipping this 16-metre 'Very Large Telescope' (Fig.1.1) with adequate instrumentation. Several institutes for astronomical research presented proposals to the representatives of the community. One design, proposed by a consortium of German institutes, asserted against the competing proposals since it did offer very versatile functions. This design proposal led to the construction of two copies of the **FO**cal

Reducer/low dispersion **S**pectrograph Fors for the ESO-VLT (Fig. 1.2) in order to observe in the UV-visual range at low (filtering) and moderate (dispersing) spectral resolution.

The design, realization and thorough testing of a Focal Reducer-Spectrograph that satisfies all observational requirements of a modern astronomical instrument is the main issue described in this thesis. The scientific aim for building such instruments will be addressed as well.
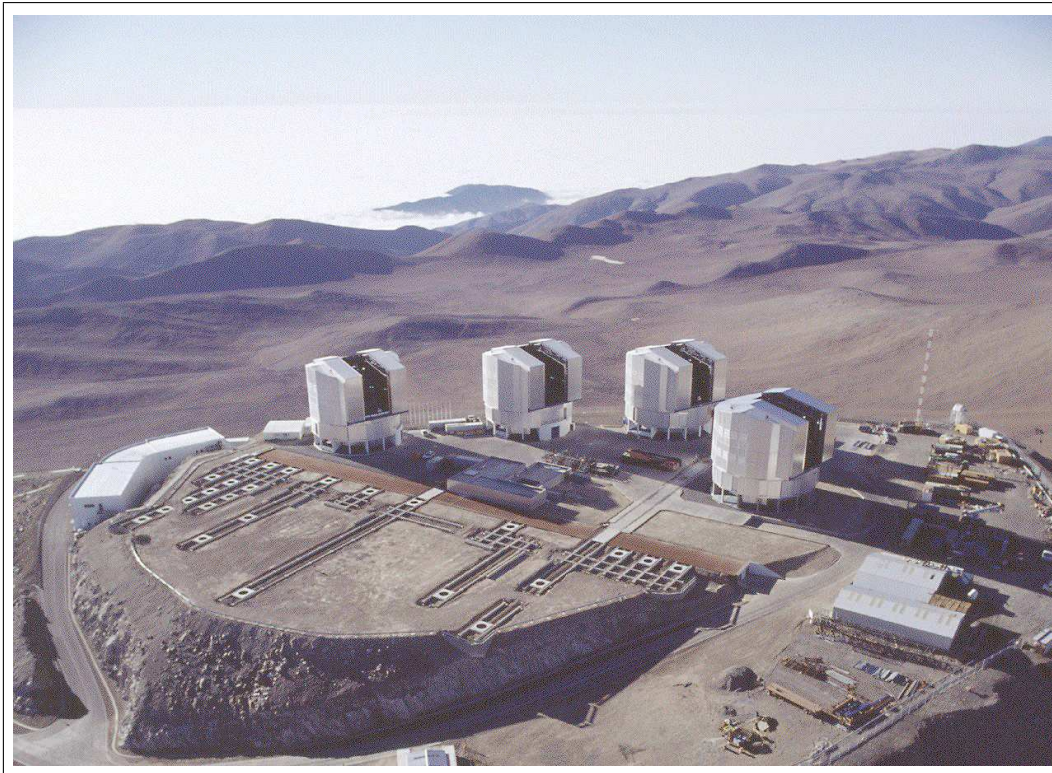
Figure 1.1: Bird's eye view of the Paranal Observatory, still under construction at the time of commissioning the two Fors instruments. This was in 1998. In the meanwhile, all four 8-m Unit Telescopes where put into operation. The VLT Interferometer with its numerous docking stations for the 2-m Auxiliary Telescopes along the linear tracks is also in operation and combines the light of different telescope configurations (including the large 8m-UTs) via 200 metre long delay lines interferometrically in the laboratory, located at the centre of the flat mountain top. The central control room is in the building to the left whereas the meteorological tower with the seeing monitor is visible in the background at right, facing the prevailing wind direction. The observatory is located in the heart of the Atacama desert in Northern Chile, next to the coast of the Pacific Ocean which is in the background covered by clouds due to the cold ocean current along the coast. The latter leads to the perfectly clear sky and the superb observing conditions of this special site.

The first chapter will address the scientific rationale in order to build such kind of instruments. It will present the classes of possible targets and the kind of astrophysical problems that are expected to be solved at the VLT with Fors. In the following, the observational constraints and the requirements in technical specification are derived from that. The third chapter presents the design concept and its realization in order to meet those specifications. One crucial step in developing such complex and sensitive instruments is the analysis of structural behaviour which has to be performed by finite-element calculation. Therefore, a chapter is dedicated to that

analysis. The following chapter will present the results that were obtained with the prototypes and the final hardware. These hardware tests ran in parallel during the course of the project, beginning with the assembly, followed by the section integration and later the full assembly at the dedicated telescope simulator. Those tests were essential in order to detect problems in a stage of the project as early as possible and to ensure that the technical specifications are met, an important aspect, especially for such a remote site as Cerro Paranal in Northern Chile is. The last chapter will give an outlook into the future where instrumental developments are expected to go.
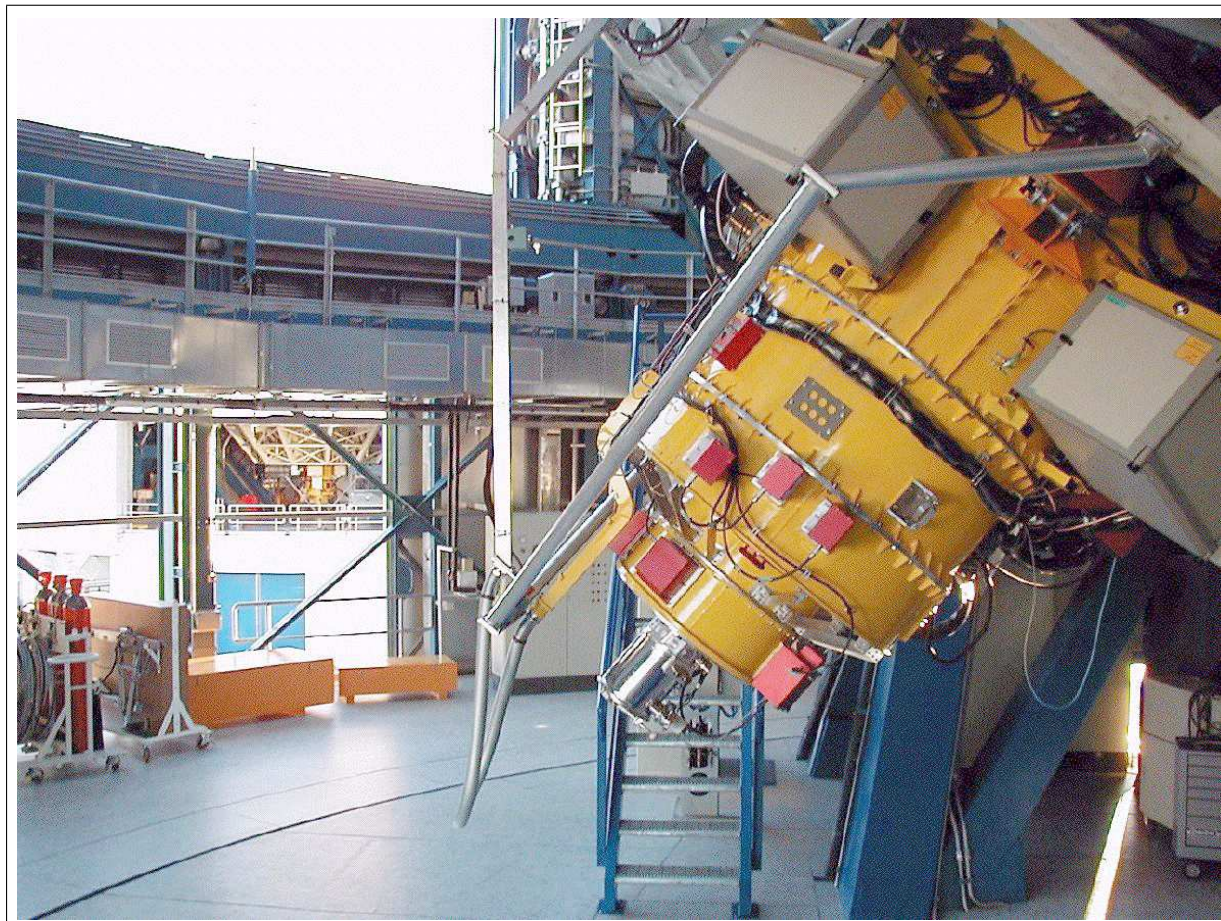
Figure 1.2: The FORS twins at the Very Large Telescope. FORS2 is mounted to Unit Telescope 2 in the foreground, while FORS1, attached to UT-1, becomes visible in the background below the large structure of the primary mirror cell.

Chapter 2

Scientific rationale and targets

2.1 Scientific rationale for building focal-reducing systems

Building an optical telescope is constrained by several factors forming a mixed bunch of technical feasibility aspects and physical constraints. One of the primary problems is the quality of the telescopic image which regards mostly the sharpness and the flatness of the imaged field. The other imaging error, affecting most of the telescopes of the last centuries, the chromatic aberrations, were overcome by the solely use of reflecting optics for large telescopes. This problem had to be solved when the refracting objectives reached their physical limit of about one metre in diameter at the beginning of the 20th century in a sense that they became so large that larger objectives would deform themselves under their own weight to an amount which would be not tolerable for the required imaging quality. Reflecting optics can be supported from its backside rather than its periphery and is achromatic by nature. The problem of image sharpness and flatness still awaits its complete solution and demands compromise. A relatively well corrected and today widely used optical train is the Ritchey-Chrétien or RC-System which should correctly be named Schwarzschild-System according to its ingenious inventor Karl Schwarzschild [10]. This system corrects the first two of the five principle aberrations of imaging, that is spherical aberration and coma, due to the use of two well corrected aspherical mirrors. But astigmatism i.e. field curvature and distortion is still a lack of the RC system. Those aberrations are a function of focal length and are inverse proportional to the F-number of the primary mirror [9]. Their elimination stresses any correcting optics following the primary mirror in the telescope's optical train. Therefore from the physical point of view, it is not very favourable to keep the primary's and thus the telescope's focal length as short as possible. It additionally adds problems in producing and testing steep aspherical mirrors. The feasibility in manufacturing mirrors of the required size and excellent quality is today constrained to F-numbers not shorter than F/1.1 for huge 8 m reflectors. The resulting focal length of today's telescopic systems leads to imaging scales of typically $500\,\mu$m/arcsecond. This ratio is to be set into relation to the prevailing seeing and to the pixel size of available detectors.

The seeing of excellent earthbound sites ranges from about 1 arcsec down to some 0.25 arcsec with a median around 0.45–0.65 arcsec. The pixel size of modern electronic detectors (Charge Coupling Devices CCD) amounts typically to $24\,\mu$m down to $7\,\mu$m depending on how many chips the manufacturer wants to cut out from the silicon waver blank. Combining those two values for

typical seeing and pixel size will spread the light of point sources over at least 10^2pixel at median seeing for the larger pixel and becomes even worse for the smaller ones. As a consequence, the rare photons of dim astronomical objects will not be used very efficiently because the detector adds readout noise to the signal at each single pixel.

The main driver for building focal-reducing systems – due to the lack of prime foci with their short focal lengths in modern optical telescopes – is to solve this matching problem between image scale and pixel size. According to the sampling theorem (cf [4], [5]) a specific function is fully described by its Fourier transform if it is sampled with a frequency which is twice of the critical value the so-called Nyquist frequency [3]. This condition is valid for both, temporal as well as spatial sampling. Therefore, an image is spatially well and fully described when it is sampled with at least twice of the critical frequency. In other words, the optimum between sampling and light detection is obtained when a point source at a given seeing spreads over 2x2 pixel. Thus the matching problem is solved if the full width at half maximum (FWHM) of the gaussian point spread function (PSF) is equal to the linear size of two pixel. If the FWHM covers more than 2 pixel then the image is oversampled. For some rare observations, an observer can gain from such oversampling. But for standard observing conditions, the observer aims for the optimum matching with 2x2 pixel. This ensures the most efficient use of the photons and therefore deepest penetration into space or vice versa high time-resolution for some brighter objects.

Matching the scale to the pixel size leads automatically to a larger field of view due to the reduction of the focal length which is the second important aspect. The detector's physical size of typically one to a very few square-centimeter would pick up little more than 1 arcmin^2 out of a 200 arcmin^2 field size that is supported and reasonably corrected by the telescope optics. Such small FOV would limit the investigation to point-like objects and their surroundings in the milky way or to the core of nearby galaxies for instance. The observation of smaller and distant galaxies that fit into the frame would become already problematic since enough sky background will be lacking for the necessary data reduction. Focal reduction will largely increase the FOV to the effect that the information content available to the observer will increase about 16–25 fold.

As a side effect, a focal-reducer can also be used in order to reduce or fully correct residual aberrations of the telescope optics like astigmatism, distortion and – due to a small mismatch of the aspheric mirrors at the UT's Cassegrain focus – also coma. Other impurities of the optical train like curvature of the detector 'plane' can also be compensated. The biggest advantage of this auxiliary optics is nevertheless the opportunity of producing a parallel beam into which different kinds of analysing optics can be inserted, especially those which are sensitive to the oblique rays in a conic beam like prisms, gratings, interference filters or Fabry-Perot etalons. These analysing optics can be in a simple version broad- and narrow-band filters which give a zero order spectral information about the objects. One problem with using interference filters in the parallel beam - the field dependence - and its solution will be addressed later. Inserting dispersive elements into the parallel beam converts the imaging instrument into a spectrograph. The achievable spectral resolution which depends on the availability of gratings and refractive materials will be addressed later.

Since astronomy has only a small or negligible influence on industrial developments of photo-electronic detectors for the commercial market – which asks for smaller and smaller pixel – the development of focal-reducing techniques and the construction of those instruments plays an important role in order to fully exploit the capabilities of the current and of the future

generation of large optical telescopes. The importance of focal reducing techniques becomes obvious when looking into programmes that are proposed for the next generation telescopes. Numerous workshops were held on the scientific use of the new VLT observatory which went into operation with the commissioning of FORS1 in 1998. One of these workshops can be regarded as representative, that is the workshop on 'Science with the VLT' in 1994 [6]. The programmes, mentioned in that conference, did cover to a large amount the extragalactic domain and proposed the use of focal-reducing technique which reflects directly the importance of this instrument type. Also other large telescope projects like the highly-segmented 10 m Keck telescope with its 'Low-Resolution Imaging Spectrometer LRIS' [7], the 8 m Subaru with the 'Faint Object Camera And Spectrograph FOCAS' [8] or the proposed 'German Large Telescope DGT' [42] rely on those capabilities. The pressure factor on booking existing focal-reducers shows that this era has already started. Two realizations that gain observational loads of overbooking factors of 2–3 are the focal-reducers EFOSC-1 and -2 which were build for the ESO La Silla telescopes.

A compressed but still rather comprehensive overview about focal reducing techniques, their justification and realization can be found in [51].

2.2 Observational targets for focal-reducing techniques

The observational tasks for focal-reducers range from solar system objects to the horizon of the known universe. The following table gives a compressed but not necessarily complete list of research programmes that promise essential progress in answering scientific issues. Part of the programmes rely either on the imaging or on the spectroscopic capabilities of focal-reducers, others on both, imaging and low dispersion spectroscopy. The list also covers those programmes that will be carried out by the VIC consortium itself during the so-called guaranteed time which will be granted for building the two workhorse instruments. These programmes are emphasized as Guaranteed Time Observations (GTO) and outlined in detail at [34].

- Solar system objects
    - Comets
        * imaging of cometary outbursts, material distribution and density in coma and tail require quite large field size
        * spectroscopic studies on chemical composition of coma and tail in MOS mode
    - Trans-neptunian objects
        * discover those objects on deep exposures as spin-off due to image contamination
        * statistical sampling giving hints on the origin of our solar system
        * estimation of mass, size and density of TNO's which are unknown yet
        * probing the inventory of minor bodies in the outer solar system to confirm their affiliation to the Kuiper belt as a source for short period comets (GTO)

- Galactic objects
    - Stars
        * magnetic white dwarfs; imaging the magnetic field topology of white dwarfs with circular spectro-polarimetry (GTO)

* Be star Hα emission lines (GTO)

– Nebulae

* nebulae within the milky way fit well into the FOV of focal-reducers; 2-dimensional velocity profiles and dispersions can be efficiently obtained with the insert of Fabry-Perot etalons

– Exotic stars e.g. X-ray binaries, neutron, pulsars, CV's

* pulsars - especially Crab - are extensively studied objects but no phase-resolved optical flux distribution is available so far; new tools uncover this the first time due to the light power required for high-time resolved 1msec spectroscopy(GTO)
* polarimetry of pulsars (GTO)
* magnetic CV's; high-time resolved spectroscopy in order to map sub-regions in the flowing stream from the magnetosphere onto the white dwarf surface (GTO)
* neutron stars

– Circumstellar disks

* doppler tomography; method for mapping the geometrical and physical structure of accretion disks on small scales $\geq 10^3$ km
* accretion disks; determining the viscosity of the disks through high-time-resolved 1 sec spectroscopy of the down to 10sec Keplerian orbiting sub-regions (GTO)
* echo mapping with very high-time (5 millisec) resolved spectroscopy to determine locations, temperatures, ionization and densities of re-processing sites (GTO)

– Black Holes

* Black Hole candidate identification programmes
* identification of an orbiting black-hole binary via deriving the mass-function of the secondary star in a X-ray transient from the reddened spectrum (GTO)

• Extragalactic objects

– Stellar observations

* determination of stellar populations in external galaxies outside of the local group in widely spread range of types like early type, radio or merger galaxies
* detecting the stellar content and population analysis of the halo of Cen A addressing radial gradients in hot systems, the tip of the red-giant branch and probing population to planetary nebulae relations (GTO)
* spectroscopy of supergiants in nearby galaxies addressing the windmomentum-luminosity-relation with intrinsic luminosity determination and re-calibrating the Cepheid distance scale (GTO)

– Galaxies and clusters

* fundamental plane; determining the FP at high redshifts allowing to constrain ages and metallicities of ellipticals as well as the luminosity evolution (GTO)
* planetary nebulae; going deep enough with focal-reducer exposures will determine the luminosity function of PN's (flattening at the faint end ?) allowing kinematic studies of galaxies and test PN's as reliable distance indicator (GTO)

– Gamma-ray bursts

* GRB's are least understood astrophysical phenomena; their transient occurrence is not predictable and is therefore a first-class Target of Opportunity for faint low-dispersion spectroscopy (GTO)

– Large scale structures

* two-dimensional imaging of sub-structures of the large scale structuring in the universe
* determination of the vertical structuring i.e. in the third dimension by deepest imaging exposures, cf Deep Field Programmes
* determination of the vertical structuring i.e. in the third dimension by spectroscopy, cf Deep Field Programmes

- Cosmological issues

   – Galaxy formation

   * probing SO galaxy formation with globular clusters (GTO)

   – Deep Field programmes

   * FORS Deep Field – FDF
      · photometric redshifts (GTO)
      · galaxy clustering evolution (GTO)
      · Tully-Fisher relation evolution (GTO)
   * Hubble Deep Field North & South – HDFN & HDFS
      · follow-up spectroscopy to the faint end

   – Gravitational lensing telescopes

   * galaxy cluster lensing; focal-reducers' field size and speed is ideal for observing lensing phenomena
   * arcs and arclets are clear indicators for gravitational telescopes; highly redshifted galaxies (z=3-5) will be lensed that the focus effect bring them into the sight of today's observing tools allowing for determining the star formation rate when the universe was very young 15 % or $3 * 10^9$y $[h = 0.7, \Omega_\circ = 0.3, \Omega_\lambda = 0.7]$ (GTO)

   – Cosmological distance indicators

   * supernovae; improving the period-luminosity-relation of the SNe Ia, providing probably the today's closest value to pin down the Hubble constant H
   * fundamental plane; this plane in 3D-space($log\ L, log\ I, log\ \sigma$) will give further distance indicator if properly calibrated with the Mgb line strength – σ relation
   * planetary nebulae; efficient detection of PN's in extragalactic systems by narrowband filtering their strong emission-lines (GTO)

   – Cosmological expansion and constant

   * planetary nebulae; the strength of the new tools allow detection of very faint PN's due to high contrast of emission lines as an indicator for a diffuse intracluster stellar population as part of the missing mass that adjust the visible to dark matter ratio (GTO)
   * cosmic shear; field size and speed of focal-reducers forces them for imaging the weak lensing and thereafter determining the cosmic shear and the dark matter amount

∗ cosmological constant; today wild speculations are going on if the so-called cosmological constant i.e. an accelerating factor in the universe really exist.

The listing above indicates that the primary fields where focal reducing techniques will improve the scientific data basis fall into the extragalactic and cosmological domain. This is not surprising since both research fields profit at most from the primary properties of focal-reducers which is their speed and their large size of the field of view.

Chapter 3

Observational drivers

3.1 Focal reducer's principle layout

The justification is outlined in the preceding chapter why focal reduction is mandatory for the new generation of large optical telescopes and which characteristics make them a powerful substitute for any missing prime focus. In the following we want to address some very specific features which are not focal-reducer's standard equipment but are all integrated into the FORS Focal Reducer/Spectrographs of the ESO/VLT.

Those features are offered as individual observing modes to the astronomers' community. Any combination of single modes is further possible as long as each mode is realized in a different section out of the three, the focal plane, the collimating, and the filter/camera section (Fig. 3.1). Offering these additional modes was a great benefit of the design proposal which at the end of a competing process led to the contract for building the two FORS instruments for the European astronomical community by the VIC consortium. The realization of the proposed design took about a decade in total for designing, manufacturing and procurement, integration and testing and for the final installation and commissioning at the telescopes of the two instrument units.

The principle layout of a focal reducing optical setup can offer both, a solution *with* and one *without* an intermediately formed image. We will concentrate our discussion on the first, the solution with an intermediate image, which is the preferred one with striking advantages such as re-imaged pupil, collimated parallel beam etc. Without the telecentric arrangement, the latter layouts are suffering due to the separation from the telescope's exit pupil. More details, requirements and (also reflective) layouts are discussed in [11].

The top section at the front end does not contain optics. From an imaging point of view, this section is only a structural mechanical part that fixes the collimating optics with respect to the front optical train and serves for attaching the instrument to the telescope mounting flange. But the fact that this section surrounds the focal plane of the telescope, which is a real image of the portion of the sky the telescope is looking at, makes this section most interesting to observers. At this location very different kinds of mechanics can be inserted in order to mask out those objects on which the scientist is focussing his interest.

The collimating section contains the auxiliary optics for transforming the conical telescope beam into a parallel beam for the analysing optics. It also forms a re-imaged pupil where parasitic
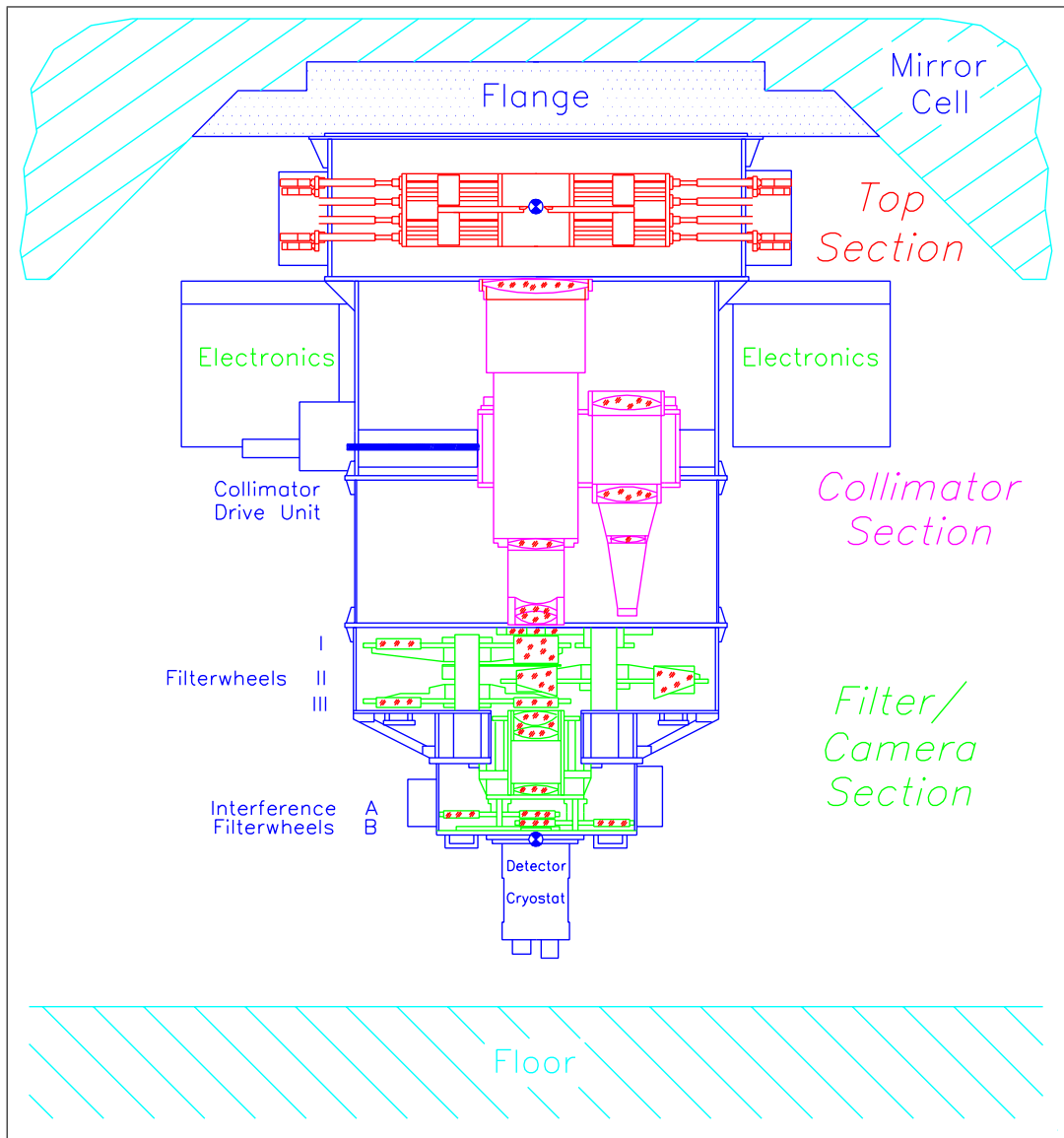
Figure 3.1: Schematic layout of a focal reducing opto-mechanical system outlined in an example of the FORS instruments. Three main sections are indicated: the top or focal plane section, the central collimating section and finally, the filter/camera section with the detector attached.
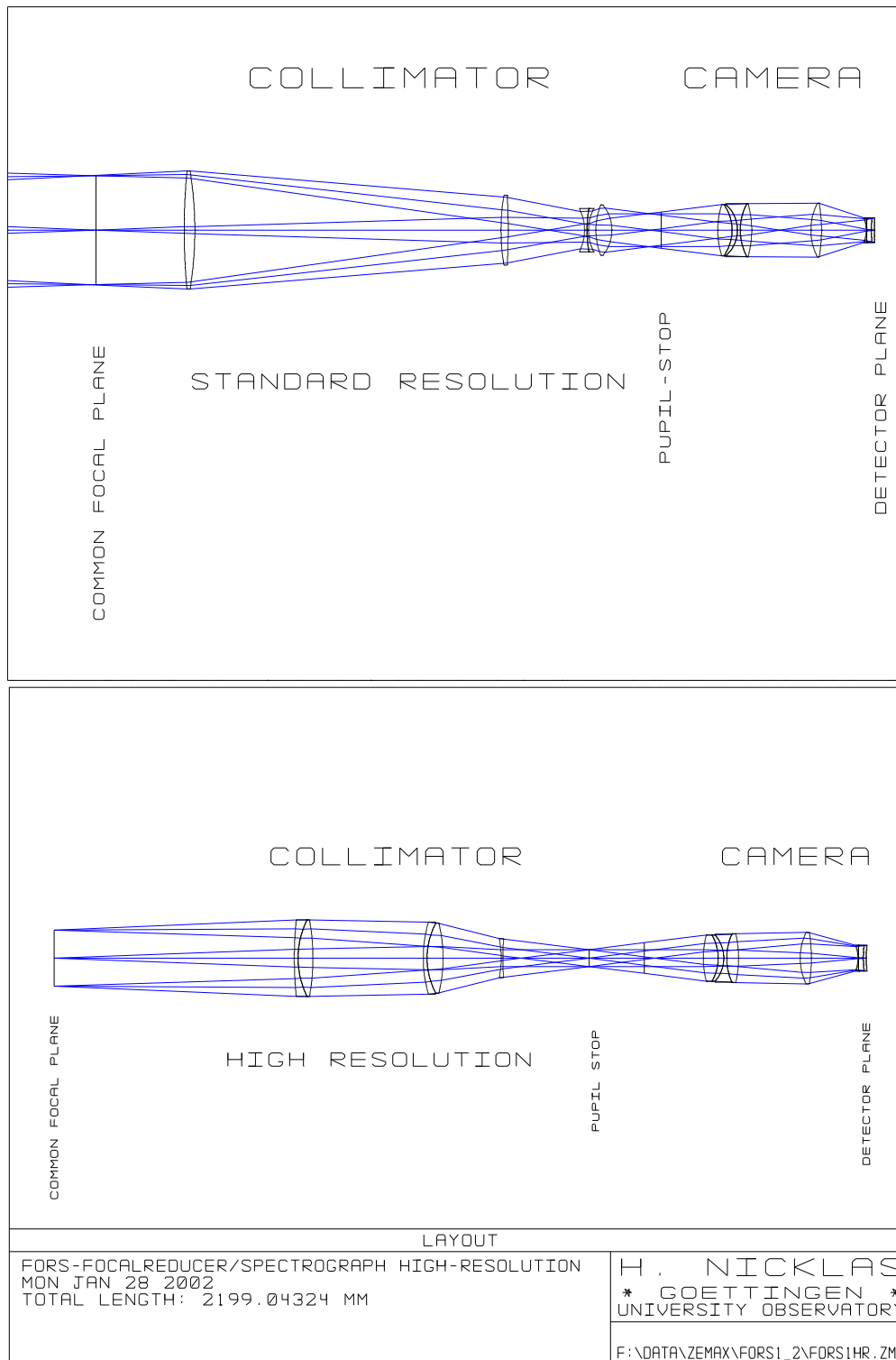
Figure 3.2: Example layout of focal reducing optics. The Fors realization offers two imaging modes, a standard and a high spatial resolution observing mode. Both modes share the same camera and detector. The smaller size of the celestial field and of the parallel beam diameter is clearly visible due to the shorter focal length of the HR collimator.

stray- and skylight will be masked out. The enormous progress in the development of astronomi-
cal observing tools becomes obvious with this section because the size of today's auxiliary optics
has become such large that the same refracting optics would have been a very large telescope
at the frontier of observing astronomy about one century ago.

The filter/camera section contains the collimated parallel beam section with the insert mech-
anisms for the spectral analysing optics as well as the focussing mechanism for the camera
optics that re-images the field with a faster F-number. The steepness of this last conical beam
determines the speed of the entire optical system.

The basic parameters of focal reducers are the following:
The reduction factor m in focal length is the ratio

$$m = \frac{f_{Collimator}}{f_{Camera}} \ .$$

The parallel beam and pupil size p of the analysing optics calculates with the relative aperture
or F-number N to

$$p = \frac{f_{Collimator}}{N_{Telescope}}$$

The final total focal length of the system becomes

$$f_{total} = \frac{f_{Camera} \cdot f_{Telescope}}{f_{Collimator}} \ = \ \frac{1}{m} \cdot f_{Telescope} \ .$$

3.2   Multiple-Object-Spectroscopy mode

Offering the Multi-Object-Spectroscopy (MOS) mode is nowadays a stringent requirement that
has to be fulfilled from any instrument. It enhances the efficiency of the telescope drastically
due to the opportunity of investigating numerous celestial objects simultaneously in one single
exposure. The efficiency gain compares to the multiplexing information of e.g. 2-dimensional
imaging by etalons with spectroscopy in the 3rd axis. Different approaches for masking out the
interesting objects exist. The FORS instruments offer two of them; the adjustable positioning of
several slitlets and the insert of a pre-cut mask into the focal plane.

3.2.1   Adjustable slitlets

This realization of focal plane selective masking uses individually movable slitjaws that can be
moved linearly within the FOV, forming tiny slitlets of individual width and position. The
slitjaws move on linear carriages and serve a field of 225mm x 225mm. The carriages were
stacked as close as possible resulting in a slitlength of 12 mm each. The 12 mm dimension is
dictated by the bending of the slitjaw carrier due to its 250 mm length in the clearance of the
telescope focal plane. The slit quality i.e. parallelism of the jaws is specified to $\pm\,3\,\mu$m over
its total 12 mm length leaving only 1.5 μm for each individual carrier. Because gravity vector
forces the carrier of opposite jaws to form a wedge shaped slit the quality specification could
only be met with a complicate and lightweight cross-section. According to these constraints,
an efficiency factor of 19 could be obtained for the MOS mode with 19 x 12 mm slitlets in the
telescope's focal plane.

The individual slitlet positioning solution has the following advantages.

- Each single slitlet can be adjusted in width and position up to the very last moment of observation according to actual seeing parameters or object data errors providing optimum match to the observation with high spectroscopic data quality.

- It offers greatest observing flexibility due to last-moment object selection.

- The image of an interesting field with undetected objects – due to the faintness at smaller 4m-class telescopes – can be obtained with a spectroscopic analysis following up immediately thereafter.

- The polished slit jaws provide a cleaner slit profile for accurate sky subtraction and improved photometry.

3.2.2   Mask exchange unit

The exchange mechanism for inserting pre-manufactured masks into the focal plane is an add-on to the movable slitlets to further improve the multi-object capability for specific observing programmes. Up to more than a 100 tiny slits can be laser-cut into a metal sheet which will be inserted into the instrument for one of the following nights. This method will lack the flexibility of the slitlets but magnifies the scientific throughput of the facility dramatically. That was the main driver for the later incorporation of a mask unit into an existing instrument which raised major manufacturing problems. Cutting a large slit into an annealed and readily machined housing may introduce irreversible deformations at the mounting surfaces due to stress release in the structure. A procedure was found that reduces the risk to an acceptable amount. Any welding was forbidden and the reinforcement at the replacement slit bases on gluing and screwing any structural parts. Another issue was the space constraint in a readily designed top section. A maximum storage capacity of ten masks could be obtained with a reasonable thick frame as mounting for the thin masking plate.

The original decision of ESO for the movable slitlets was driven by their advantages (cf Tab. 3.1) and by operational constraints that aimed for a minimum of man-power for observation preparation. Nevertheless, several scientific programmes gain more on high throughput for statistical purposes than on the slit quality or on sky-subtraction. Which of the two offered techniques is most appropriate to the observing programme depends on the scientific aim and is the duty of the observer to decide and apply for.

3.3   High-Spatial-Resolution mode driver

The seeing of the earth's atmosphere varies on time scales of minutes to days ranging from several arcseconds diameter down to about $0\rlap{.}''25$ or even better at such excellent sites as Hawaiian Mauna Kea and Cerro Paranal in the Chilean Atacama desert. The main driver for focal reducing is optimal pixel matching to the spread of the seeing disk as outlined above. This optimum is then achieved for one specific seeing which has to be defined as standard seeing and is regularly chosen just below the median value from the statistics of seeing monitoring. Because extraordinarily good scientific output can be achieved at the rare moments of exceptionally good seeing – about

	Movable Slitlets	Pre-cut Masks
Throughput efficiency	+	+++
Adjustability to observing conditions	+++	−−
Seeing and error adaptation	++	−
Flexibility in observing scheduling	+++	−−
Short term follow-up observing	+	∼
Slit quality profile	++	−−
Sky subtraction	++	∼
Personnel interaction	++	−−−

Table 3.1: Comparative listing of the specifics of the two MOS modes, movable slitlets and pre-cut mask, both implemented in the FORS instruments.

a 5 percentile at the upper end of the statistical distribution – the observing programmes often request to fully exploit the capabilities of the facility. The choice for optimum pixel matching by changing the imaging scale into a higher spatial resolution is very reasonable.

This mode is realized in the FORS instruments with a separate collimating optics of only half of the focal length of the standard collimator. The switching from one imaging scale to the other is achieved via inserting the high-resolution (called High-Res or HR) collimator into the beam and exchanging the standard collimator. This has to be done with moderate precision of one tenth of a millimetre but the stability of the position within the beam has to be maintained within microns for the 200 kg optical unit due to image motion and spread of image quality on the detector.

3.4 Interference-filter constraints

The big advantage of focal-reducers is their provision of a parallel beam section for inserting analysing optics which allows switching between imaging and spectroscopy mode. In principle also interference filters can be inserted there for narrowband observations. All rays are parallel in that section but the oblique angle at the pupil varies with the position in the field. Due to that effect, the transmission curve of the IF-filters varies with field position leading to circular rings of constant filter transmission around the optical axis. The inclination angles in that section increase that much that the transmission curve for the outer regions of the field will be shifted by an amount toward the blue that an overlap between original and shifted transmission curve even for moderate narrowband filtering of 50 Å no longer exists. Additionally, the transmission curves will be deformed and widened for any oblique ray.

These effects of deforming, widening and shifting can largely be compensated by inserting the IF-filter into the camera beam just in front of the detector's field lens. At this location, the rays of all objects fall with more or less identical conical beams onto the detector. The transmission curve becomes therefore field-independent. The relative aperture of the focused conical beam leads also to a small deformation and blue-shift of the transmission. But they amount only to a fraction of those in the parallel beam and appear acceptable. They are either negligible for the science programme or they can be taken into account by post-detection compensation.

The request is that the transmission window is the same for all objects in the field leading to complete detection without any selective effect.

A price had to be payed by the instrument mechanics to overcome these effects. The camera optics of former instruments was bolted in most cases directly onto the detector flange for two good reasons. First, any motion between camera and detector due to mechanical flexure results in a 1:1 motion of the image and spreading of the PSF among more pixels. Second, the required re-positioning accuracy of the detector after de-/attachment can be high in the order of tens of microns in case of field lenses and curved detector planes. Both mechanical properties have to be assured in order not to risk any loss in instrumental performance.

The FORS design takes this into account and is extensively analyzed in that specific respect. Solving it with the design was a mechanical issue but the technical solution is proven with hardware to fulfil all requirements according to specification. A sophisticated design connects the camera focussing mechanism with the attachment flange for the detector for rigidity and positioning accuracy although both are cut into separate sections due to the location and size of the two filterwheels for accommodating up to eight IF-filters.

3.5   Polarimetry and spectro-polarimetry driver

The Cassegrain focus of a telescope beats all other foci with two advantages, except for the prime focus which is not realized in the Unit Telescopes of the VLT. It realizes minimum light loss due to less reflections and lowest instrumental polarization due to nearly perpendicular reflections at the primary and secondary mirror. These are two striking reasons to implement the polarimetric observing mode in the FORS imager and spectrographs. The FORS instruments offer according to the current instrumentation plan of ESO the only opportunity for polarimetric work of all 17 focal stations of the VLT. This opens the chance for insights into very interesting processes like the physics of accretion disks around black holes or the energy-mass transfers on exotic objects like neutron stars, cataclysmic variables, magnetic white dwarfs and others.

The focal-reducers are designed that the observer can alternate between $\lambda/4$- or $\lambda/2$-plates in the parallel beam for phase retardation of either linear or circular polarized light. The analysing is done with a Wollaston prism, next to the retarder plates. Due to splitting the beam into ordinary and extraordinary light, half of the FOV has to be masked out to prevent overlap of the beams. Due to the two focal lengths of the standard and high resolution imaging modes, two masks of different separation became necessary. The space constraints in the focal plane were solved by generating a strip mask with an alternate setting of the MOS slitlets for the standard mode and by inserting a separate strip mask for the high-resolution mode. Due to the combination with dispersing elements in the parallel beam section, the observer has the choice between four modes, imaging- and spectro-polarimetry in both, linear and circular polarized light.

3.6   High-Time-Resolution mode driver

The high-time-resolution HIT mode is a very specific observing technique. The ultra-fast clock rate of the CCD detector with an open exposure shutter is used here. The telescope keeps the

object of interest tracked within a small slit at the edge of the field. The detector controller shifts the charge of the point image or of the small spectrum by one or a few pixel into the next pixel row. A 2kx2k pixel detector can thus add up to 2 000 spectra with an exposure time as short as one millisecond or less, depending on the photon flux produced by the source brightness, the telescope's collecting power and the clock rate of the order of Megahertz. After a maximum of 2 000 charge shifts the full CCD detector is red out and the cycle of integration and shift can start again.

This technique allows the detection of spurious events such as the very short term variability within accretion disks, thus resolving spatially very small regions of the order thousands of kilometer. Another object with very short variability are pulsars which could be resolved so far only in the radio frequency domain. It is now for the first time possible to detect those pulses in the optical regime in real time due to collecting power of the 8m UT's.

Chapter 4

Opto- and electro-mechanical constraints and specifications

4.1 Optical quality and performance

4.1.1 Gain of Active Optics

The classical telescope mirrors did already suffer gravitational bending under their own weight. This was compensated to a large amount by the intrinsic stiffness of the blank in combination with a sophisticated support system. Numerous designs were developed over the centuries for the latter, ranging from lever (Lassel and others) over whiffletree to hydraulic (e.g. ZEISS) systems. Their specific design regarding density, friction etc. did depend on the stiffness of the blank itself which was primarily determined by the blank's thickness, secondly by the material's choice. The simple plate of equal stiffness scales very roughly with D^4/d^2. Producing nowadays 8–10 metre blanks would then lead to blanks that are larger in thickness than in diameter. Taking into account classical mirror support systems would reduce this tremendous thickness to typically 50–60 cm which measures for instance the mirror of the 3.5-m Calar Alto telescope – in contrast to the modern 8.2-m VLT primary mirror that measures no more than 17.5 cm at the same support density, roughly determined by $D^2/(d \cdot n) \approx 70$ cm for n supports [9].

It is obvious from manufacturing, structural, optical and thermalization reasons – which shall not be discussed here – that such thick blanks could no longer fulfil their requirements. It became clear, that the telescope builders had to depart from that classical approach and work started in the late 70's on developing active optics with laboratory tests on a 1 metre mirror [14].

The term 'active' optics denotes that the optics of the telescope is permanently maintained in two respects, a) optical surfaces are corrected to a tolerable deviation from the perfect figure and b) position of the optics is corrected in shift and tilt to tolerances given by an error budget. Altogether determine the optical quality of the telescope that is specified by a light concentration ratio (relative to an undisturbed perfect one) or better by a central intensity ratio.

The first telescope, that was built with an active optics system, was the ESO New Technology Telescope (NTT) that went into operation in 1989 at the La Silla Observatory. The image quality of this telescope, that was obtained already with the first light, was astonishingly and unrivaled

at that time. The 3.5 m NTT was in fact the test bed for the active optics of the much larger VLT. Nevertheless, numerous analyses were necessary in advance to built the active optics of the VLT properly. For instance, thorough investigations turned out that the large primary mirror could suffer from wind buffeting across its 8 m diameter by differential atmospheric pressure. This had to be taken into account in designing the control loop system [15].

The closed loop control system works against image degradations that are caused by slowly varying gravitational, thermal and wind buffeting loads. It is therefore quite slowly and stops typically around 1–10 Hz where a transition zone in the frequency domain exists. At control frequencies of closed loop correction of higher than 1 Hz, the domain is called 'adaptive' instead of 'active' optics. It works very fast – up to the limits of the currently existing technology in control and computer hardware – and does not aim for a perfect mirror surface but deforms a flexible reflector in a controlled way and amount that the wavefront deformations, imprinted by the earth's atmosphere [18], will be optically balanced out. This enables astronomers to overcome atmospheric seeing limitation with groundbased telescopes and opens up incredible observational potentials.

4.1.2 Wavefront aberration and Strehl ratio

Rayleigh criterion and wavefront aberration

The classical Rayleigh criterion is no longer sufficient in order to specify the telescopic optics for the requested imaging quality.

$$d_{Rayleigh} = 2 \times 1.22 \, \frac{\lambda}{D} \, 206\,265 \, arcsec$$

It corresponds with the well-known quarter-wave criterion and the 80% encircled energy in light concentration [13]. These specifications do not take into account all kind of optical aberrations, especially not any high-frequency ripple structure on the reflecting surface.

These terms of specification have been sufficient for characterizing optical performances in the past when optical surfaces had been ground and polished with a tooling dish of identical size as the mirror blank itself. The manufacturing of large optical surfaces have changed significantly. It has become a generating process of larger, deeper and steeper optical surfaces with smaller and smaller tools. These tools tend to introduce ripples of high spatial frequencies due to their relatively small size and flexibility. Such kind of reflecting surface deformation would deposit quite large amounts of photonic energy in the wings of the point spread function (PSF). This could led to a widening of the PSF profile – similar to a peak within a wide halo – which would not safely be detected by the encircled energy criterion. The latter is based on a PSF with more or less a Gaussian profile. Larger departure from Gaussian profile would result in inadequate specification of optical performance in respect of light concentration.

The impact factor of ripple becomes obvious in the ratio between the aberration coefficients, measured either as peak-to-valley or as root-mean-square amplitude. Table 4.1 lists the primary optical aberrations with their functional dependance on radius and azimuth as well as the coefficient ratio between peak-to-valley and rms-values of the same optical effect. Coma and astigmatism are both quite insensitive, followed by defocus and tilt. Even the best-known

Aberration term	Wavefront Function	Ratio $\frac{PTV}{RMS}$
Defocus	$\kappa_D \; \rho^2$	$3.46 = \sqrt{12}$
Tilt	$\kappa_T \; \rho \; cos\,\phi$	$4.00 = 2\,\sqrt{4}$
Spherical	$\kappa_S \; \rho^4$	$3.35 = \sqrt{11.25}$
Coma	$\kappa_C \; \rho^3 cos\,\phi$	$5.66 = 2\,\sqrt{8}$
Astigmatism	$\kappa_A \; \rho^2 cos\,2\phi$	$4.90 = 2\,\sqrt{6}$
Sinusoidal Ripple	$\kappa_Z \; cos\,(\frac{\rho}{\lambda_Z})$	$2.83 = 2\,\sqrt{2}$

Table 4.1: Primary optical aberrations, also called Seidel or classical aberrations, supplemented by the modern ripple defects. Their surface deviation will be imprinted onto the wavefront according to their dependance on radius ρ and azimuth angle ϕ. Their amount is usually given in waves or nanometre as either peak-to-valley PTV or as root-mean-square RMS error. Both errors have a fixed ratio for each type of aberration. A rigorous deduction in terms of Zernicke polynomials led to the ratios, given above [14].

spherical aberration has lower impact on optical quality than ripple errors. This means, for a constant amplitude of wavefront or reflecting surface error, ripples will lead to the highest rms-errors, affecting the optical quality at the most. Therefore, one has to guarantee that the specification of the quality of optical telescopes detects the most prominent error of modern manufacturing methods.

Strehl intensity ratio

In 1902, K. Strehl introduced a general optical quality criterion, the Strehl Intensity Ratio SIR. It denotes an arbitrary criterion definition, that the central peak intensity I(Q) should not fall below 80% of the level of a perfect imaging system I_0 by any aberration. It is linked to the wavefront aberration accordingly to

$$S_{IR} = \frac{I(Q)}{I_0} = 1 - \left(\frac{2\pi}{\lambda}\right)^2 W_{rms}^2$$

leading to a total wavefront error of maximal $\lambda/14$ rms for a 0.2 reduction of the central peak. This criterion becomes identical to the classical $\lambda/4$ Rayleigh criterion for the primary Seidel aberrations of defocus, spherical aberration, coma and partly to astigmatism, but not for ripples on optical surfaces. In these cases of concentric sinusoidal zones, the rms wavefront aberration has to be tightened to $\lambda/10$ for 0.8 central peak intensity. The 0.8 Strehl ratio has become an accepted standard criterion for qualifying optical transfer systems.

Central intensity ratio

The Central Intensity Ratio CIR is an extension to the SIR. It is a kind of Strehl Ratio for optics working in a turbulent atmosphere like earthbound telescopes [17].

$$CIR = 1 - 2.89 \left(\frac{\sigma}{\theta_0}\right)^2$$

with θ_0 the FWHM of the atmospheric seeing angle and the rms *slope error* σ of the wavefront. With $\theta_0 = 0.976 \frac{\lambda}{r_0}$ and r_0 the so-called Fried parameter or time-averaged atmospheric coherence length and the *normalized* wavefront error σ the CIR drop becomes

$$\Delta CIR \approx \left(\frac{r_0 \, \sigma}{\lambda}\right)^2$$

The individual errors of each attributing optical component i add to the overall optical quality performance according to

$$1 - CIR = \sum_{i=1}^{N} (1 - CIR_i) \ .$$

If the telescope optics is specified correctly according to the prevailing seeing then a telescope with a CIR=0.8 would introduce a loss of about 10% in the observed FWHM or encircled-energy diameter.

4.1.3   Maintaining the telescope imaging quality

The optical quality of the VLT Unit Telescope is specified to have a

- $CIR_{total} = 0.804$ at Nasmyth focus   and

- $CIR_{total} = 0.789$ at Cassegrain focus

where the FORS instruments are located. The latter differ to a small amount 0.985 from Nasmyth focus due to a conversion error of 0.975 and the lack of the figuring error of 0.990 of the tertiary mirror.

This 0.8 specification means that the image quality in the Cassegrain focal plane, that will be picked up by the FORS optics, is totally seeing dominated. The profile of the PSF is therefore clearly defined without major uncertainties from optical fabrication or alignment. It is fully described by the optical transfer function $T(u)$ of spatial frequency u

$$T(u) = e^{-3.44 \left(\frac{\lambda u}{r_0}\right)^{\frac{5}{3}}}$$

leading to the point spread function by the Hankel transform or Fourier-Bessel transform $\langle |T|^2 \rangle$

$$I(r) = e^{-6.88 \left(\frac{r}{r_0}\right)^{\frac{5}{3}}}$$

which is reasonably close to a Gaussian function in the core due to the $\frac{5}{3} \sim 2$ exponent according to the pioneering work, done by Kolmogorov and Fried [18]. The variable r_0 is known as the Fried parameter and describes the effect of the earth's atmosphere in optical terms. It characterizes the atmosphere with a scale length of its turbulence and has the same effect on the diffraction limit as an aperture stop and replaces the stop diameter D in the Raleigh criterion.

It is far out of the scope of this thesis to describe the operation of 'adaptive' optics or even its potentials. On the other hand, it is not necessary to do this here in the context of instrument specification since both FORS instruments are mounted to the Cassegrain foci of the VLT that are not supported by an adaptive optics system, contrary to the Nasmyth and Coudé foci.

4.1.4 Compensating the telescope's astigmatism

The superb imaging quality of the VLT's Unit Telescopes was outlined in the previous sections. The FORS instrument optics, mechanics and electronics was built in a way that it is able not only to maintain this imaging quality of the telescope, but moreover, it removes also the residual imaging errors of the telescope. The second and the third of the five Seidel or principle aberrations are affecting the Cassegrain focus of the VLT-UT telescopes. The latter, the astigmatic error is intrinsic to the Ritchey-Chrétien system that is designed to compensate the first two principle aberrations, spherical aberration and coma. This ingenious design, the combined correction through two aspheric mirrors, was rigorously formulated for the first time by Karl Schwarzschild in his aberration theory of the year 1905, director of the Göttingen Observatory at that time. His theory was based on the Eikonal function and did cover the five Seidel imaging errors [10].

The VLT unit telescopes suffer a small residual coma which is not a standard imaging error of RC-systems. This error is originated by a mismatch of the aspheric primary and secondary mirror at the Cassegrain focus since the telescope optics is primarily designed for the Nasmyth foci. These foci are located at a larger distance from secondary mirror than the Cassegrainian which is lifted from its nominal position, congruent to the Nasmyth focus, to a more convenient upward position on the azimuth platform. This shift of a focus without major image deterioration has become possible for the first time due to the active optics of the 8 m primary mirror by adding more curvature to the mirror. But, this shift by curvature adaptation leads to a small mismatch error between the aspheric constant of the primary and secondary mirror.

Introducing additional refractive power into the optical train – for instance through focal reducing optics – opens up the opportunity for compensating both errors, astigmatism and mismatch coma. Thus, the lens system is designed in a way that it removes the residual comatic error as well as the intrinsic astigmatism which is mandatory to image the 7' FOV with sufficient quality in ray concentration onto a flat CCD detector.

The optical quality specification for the single UT led to an image spread of 0.″077 rms geometrical radius or 236 nm rms wavefront error at 3' field radius due to these residual aberrations. This imaging quality corresponds to a CIR of 0.91 of the original 80% on the optical axis [16]. This was the contractual specification for the opto-mechanical combination in the error budget.

The specification for the imaging quality by the instrument onto the detector was set to a concentration of 70% within 1 pixel *and* >90% within 2x2 pixels within a field radius of 4 arcmin in SR and 2 arcmin in HR imaging mode including the broadband Bessel-U, B, V, R, I and

Parameter	Standard spatial resolution mode	High spatial resolution mode
Image scale	$0\rlap{.}''2$/pixel	$0\rlap{.}''1$/pixel
Linear scale	$120\,\mu\mathrm{m}$/arcsec	$240\,\mu\mathrm{m}$/arcsec
Image quality EE	80% in $0\rlap{.}''2$	80% in $0\rlap{.}''1$
Collimator focal length	$1233\,\mathrm{mm}$	$616.5\,\mathrm{mm}$
Camera focal length	$280.4\,\mathrm{mm}$	$280.4\,\mathrm{mm}$
Parallel beam/pupil diameter	$90.6\,\mathrm{mm}$	$45.3\,\mathrm{mm}$
Reducing factor	$m = 4.4 = 1/0.22$	$m = 2.2 = 1/0.45$
Focal length f_{total}	$25\,000\,\mathrm{mm}$	$50\,000\,\mathrm{mm}$
Rel. aperture or speed	F / 3.13	F / 6.25
Field of view	$6\rlap{.}'83$ x $6\rlap{.}'83$	$3\rlap{.}'41$ x $3\rlap{.}'41$
Focal plane size (telescope)	$218\,\mathrm{mm}$ x $218\,\mathrm{mm}$	$109\,\mathrm{mm}$ x $109\,\mathrm{mm}$
Focal plane size (detector)	$49.2\,\mathrm{mm}$ x $49.2\,\mathrm{mm}$	$49.2\,\mathrm{mm}$ x $49.2\,\mathrm{mm}$
CCD detector type	$2\,048$ x $2\,048$ pixel	manufactured by 'Site'
Pixel size	$24\,\mu\mathrm{m} \cong 0\rlap{.}''2$	$24\,\mu\mathrm{m} \cong 0\rlap{.}''1$
Quantum efficiency	min. 44% (U) $\rightarrow$	max. 75% (R)
Spectral resolution (RS product)	$185 - 2\,700$ per $1''$ slit $\Rightarrow$	$5.4 - 0.7$Å/pixel

Table 4.2: Optical parameters of the verified design of the Fors focal reducing imager and spectrographs for both, the standard and the high spatial resolution imaging mode.

Gunn-z filter. The relevant optical parameters of the Fors instruments are listed in Table 4.2.

4.1.5 Mechanical constraints of optical matching

Manufacturing accuracies of lateral and longitudinal lens positioning

The goal for yielding such high optical quality in imaging defined the constraints for the mechanical mounts and the positioning of the optics within the light beam. A tolerance analysis with a ray-tracing program, calculated by our consortium partners, estimated the general positioning accuracy for the individual lenses or lens groups of maximal 0.1 mm in lateral and 0.25 mm in longitudinal shift and $60''$ in tilt with respect to the optical axis. A Gaussian distribution of the positioning errors from the perfect one was the underlying assumption. These general tolerances were not applicable at the following locations. The second doublet of the HR-collimator required 0.05 mm and 0.1 mm in lateral and longitudinal position accuracy, respectively. This was caused by the refractive power of that doublet which was even beaten by the lens power of the four-lens group of the camera optics. The latter required a positioning accuracy of 0.025 mm for lateral shift and less than $30''$ tilt with respect to the beam.

These tolerances did not share their amount with other errors in a budget. Therefore, they had to be met with absolute accuracy by manufacturing the parts of the optical bench. The lens mounts and connecting tubes were machined on milling and turning machines to that accuracy. The lenses and lens groups were inserted into their mounts without any opportunity of adjustment. Finally, a light concentration of 80% – above the specified 70% – ensquared energy EE in a single

$24\,\mu$m pixel could be achieved with that method and was demonstrated with the hardware on an optical test bench.

Focusing accuracy

The focusing mechanism was an issue in several respects. A focusing range of $12\,$mm had to be bridged with a positioning accuracy of $1\,$micron. This huge focusing range, when compared to the standards of tenths of a millimetre, became necessary through the insert of the narrow-band filters as plane-parallel plates into the camera beam, as outlined in the previous chapter. The required performance was achieved with a design of an eccentric disk drive, together with a direct linear encoding at $0.5\,\mu$m resolution. The linear stage of the focusing mechanism was spring loaded against a large circular ball bearing that is mounted eccentrically onto the motor driving shaft, thus avoiding any hysteresis or other effects.

Stability issues

The stability of the refractive optical components within the beam was a real challenging issue. The optical elements had to be kept in position within fractions of those tolerances, mentioned above, primarily remnants from the manufacturing process. Those would affect image quality alone. The wandering of the image on the detector – caused by the bending of the not perfectly stiff optical bench by the load change during observing – was still not covered by them, but will be addressed next.

The tolerance in image shift during an 0.5–2 hour exposure of a quarter pixel – in other words $6\,\mu$m – did allow only 10–20 μm lateral shift or $5\,$arcsec tilt of any single optical component. A combination of these errors would reduce those tolerances down to fractions of this amount, the order of microns and arcseconds. The FORS design did avoid this, but utilized another advantageous fact. Combining these misalignments in a correct way would relax those tolerances significantly which we called the flexure compensation.

The FORS performance did largely profit from this flexure compensation. It's one of the greatest successes of the project that this compensation could be designed, thoroughly analyzed and validated in its realization. Due to its large impact on the design and the instrument performance, this flexure compensation is outlined in a separate chapter.

4.2 Mechanics specification

4.2.1 Design drivers for the mechanics

The following section lists the performance specifications that formed the framework in which the design and realization of the instrument mechanics took place. It is only an excerpt of the specifications, fixed by the ESO contract, that were related to the instrument mechanics, the responsible part of the Göttingen Observatory. The listing gives an overview on the design issues but does not cover all the internal specifications which were deduced from the numerous opto- and electro-mechanical interfaces.

In the course of the project, it could be demonstrated that all these specifications have been fulfilled successfully. This statement can be reviewed through a comparison of the specifications, listed here, with the real instrument parameters and test results, obtained in the end after the design, manufacturing, test and improvement phases, which are given in Section 5.2.3 about the realization and the performance characteristics.

4.2.2 Top-Section with focal plane equipment

- Multiple Object Spectroscopy – MOS focal plane mode

  - FOV: supporting the total 7 arcmin FOV in SR (incl. HR) mode
  - slit number: 19 moveable, adjustable and remotely controllable slitlets
  - slit length: $19''$ to $25''$
  - setting time for slit pattern: in total ≤ 25 seconds
  - setting accuracy: $\leq \pm 13\,\mu\text{m}$ or $\pm 0\!''\!025$
  - slit widths: minimum $150\,\mu\text{m}$ or $0\!''\!3$
  - width accuracy: $\leq \pm 5\%$ or $\pm 10\,\mu\text{m}$
  - slit edges straightness: $\leq \pm 3\,\mu\text{m}$
  - slit edges parallelism: $\leq \pm 5\,\mu\text{m}$

- Mask Exchange Unit – MXU focal plane mode (FORS2 only)

  - function: insert and replacement of pre-cut slit mask
  - FOV: mask with slit pattern covering the entire FOV in SR (incl. HR) mode
  - slit quality: depends from the laser cutting device, the Mask Manufacturing Unit MMU of the Paranal Observatory
  - storage capacity: at least for one observing night within instrument without further replacement, minimum 9 masks in the existing housing
  - reliability: fail safe interlock system

- Longslit spectroscopy mode

  - longslit number: at least 3 separately longslits to select
  - longslit widths: between $0\!''\!5$ to $1\!''\!5$
  - longslit lengths: at least $4'$
  - longslit straightness: $\leq \pm 15\,\mu\text{m}$
  - longslit parallelism: $\leq \pm 10\,\mu\text{m}$

- Polarimetry focal plane mask for

  - standard spatial resolution imaging and spectroscopy
  - high spatial resolution imaging (and spectroscopy with FORS2)

- Special mask for the HIT-mode i.e. doing high time resolution observing

- Illuminating and imaging units with internal calibration sources

4.2.3   Collimator-/Filter-/Camera-Section with optics

- Mounts and optical benches for

  - collimator optics with imaging scale in standard spatial resolution
  - collimator optics with imaging scale in high spatial resolution
  - camera optics

- Motion drives for

  - collimator exchange
  - camera focusing

- Three filter wheels at the parallel beam section for accommodating at least seven analyzing optics each

- Two filter wheels at the camera beam for accommodating at least four narrowband interference filters each

- Camera exposure shutter with

  - exposure time: 1 second at the minimum
  - photometric accuracy: $\leq 1\%$

- Parasitic light suppression along the light beam through

  - careful baffling of focal plane units, collimator and camera tubes
  - adjustable pupil stop

4.2.4   Technical constraints

- Mass, momentum and torque limit

  - weight: $\leq 2\,500\,\mathrm{kg}$
  - momentum: $\leq 20\,000\,\mathrm{Nm}$
  - torque: balanced to $\leq 500\,\mathrm{Nm}$

- Earthquake loads: withstand up to $5g$

4.2.5   Maintenance and reliability

- Operational lifetime: at least 10 years

- Reliability

  - 3 months period: $\leq 3^{h}$ repair time
  - 6 months period: $\leq 1^{d}$ repair time
  - 12 months period: $\leq 2^{d}\!-\!3^{d}$ repair time

- Maintainability: no major overhaul.

- Safety according to the applicable regulations during all operations and maintenance

  - mechanical safety for the observatory staff
  - electrical safety for the observatory staff

Chapter 5

Design concepts and realisation

5.1 Design specifics

Addressing all design features, requirements, issues and solutions would go far beyond the scope of this thesis. Therefore, the features that are very specific for the FORS design and their performance will be outlined and discussed in the following.

5.1.1 Image motion compensation, passively maintained

Compensating the wandering of the image on the detector is one of the central achievements that distinguishes the FORS from other focal-reducers. A fully *passive* compensation could be achieved that works absolutely fail-safe when properly designed and adjusted at initialization. This kind of operation on instrument level is similar to the compensation that was once developed by M. Serrurier [24] when constructing the truss work of the Palomar 5 m telescope tube. Serrurier had to beat (like us) gravity, displacing the opto-mechanical components. His ingenious idea was to build the structure not absolutely rigid, but to allow the optics a tremendous decentring shift, expressed in optical units, but reached a perfect alignment by managing those shifts, first to their amount and second by a parallel sag at both ends of the truss. He utilized the effect that the heavy primary mirror can be counter-balanced by the lighter secondary to the identical amount if he designed the truss work, extending from opposite sides of the centre piece, with appropriate structural stiffness.

The situation at Cassegrain instruments differs from this because they are bolted with their front end to the attachment flange of the telescope. Thus, relative simple counter-balancing at the right stiffness would not work in our case. Therefore, the image motion compensation by flexural adjustment departs from Serrurier's compensation principle in a sense that we utilize directly the structural bending behaviour instead of avoiding the flexural tilt, as Serrurier did through transforming the bending forces into tension and compression of a rod equal to push-pull forces along the struts with a tremendous increase in overall stiffness. Thus, he transformed the load from flexure load into the more resistant shear strain of the right yield together with a sophisticated truss geometry that ensured the parallel shift of both, the large mirror cell and the top front ring, carrying the secondary mirror via the spider.

Setting up the compensation by passive means is supported through the optical properties of focal reducing systems if designed properly. When setting up a solely dioptric system, three major components may contribute to image motion on the detector due to tilting or lateral translating the optical components. The three components, that are affected, are the collimating and the camera optics and the detector itself. In the following, positioning errors in lateral shift and tilt are assumed to such small amount that image quality will be un-affected.

Tilting the collimator within this constraint has no effect as well as decentring the camera/detector unit. But, lateral movement of the collimator against the optical axis results in tilting the parallel beam which leads to an image shift on the detector

$$dy_1 = \frac{f_{camera}}{f_{collimator}} \cdot dy_{collimator} = \frac{1}{m} \cdot dy_{collimator}$$

inversely proportional to the focal reducing factor m, the ratio of collimator and camera in focal length. On the other hand, tilting the camera/detector unit will originate an image shift of

$$dy_2 = - f_{camera} \cdot d\alpha_{camera}$$

if the unit turns in a sense that the collimator is effectively shifted in the same direction as the previously mentioned translation.

Structural bending supports now fortunately that translation and the rotation of a cantilevered beam follow in principal the above relationship [12]. Additional image motion will be introduced by any displacement of the detector against the camera optics in a one-by-one relation of

$$dy_3 = -dy_{detector} \,.$$

All these image shifts add up to an effective motion on the detector which can be compensated theoretically down to zero. The issue is now to design the stiffness of the main structure and all related parts that collimator translation and camera tilt matches each other. The second condition is that the connection between camera and detector is designed stiff enough that both behave as a single unit that no detector displacements relative to the camera takes place. The latter had become challenging in the FORS design because both, camera and detector, were separated into two units since two large filterwheels had been inserted into the camera focusing beam, outlined in previous chapters.

A rigorous analytical formulation of image motion due to lateral translations, tilts and refractive power of the elements is given in the following. The collimator and camera itself are assumed to be totally rigid units due to their stiff tube structure neglecting any bending effects. But their linear extension along the beam is taken into account. This assumption could be fully confirmed because the calculation, taking into account the shift of each optical element in a ray-tracing program led to the same results as a manual calculation according to the formulation, given below.

A closer look onto imaging properties of extended optical systems reveals that tilting a collimator leads to an oblique beam if the system is not turned about its so-called ' neutral axis', thus shifting to image by tilt. Where this neutral rotation axis is located depends on the refractive power of the individual optical elements and has to be determined for each collimating system individually. This longitudinal decentring effect is taken into account with the neutral axis coefficient $c_{n.axis}$ which accounts for the effective shift of this axis, introduced by tilting the

collimator. Another correction is already mentioned, the displacement of the detector relative to the camera's optical axis. The latter is applied through subtracting the amount $dy_{opt.axis}$ according to the camera tilt $d\alpha$ and the detector separation Δz from the camera's exit lens.

The focal reducing factor $m = \frac{f_{collimator}}{f_{camera}}$ together with

$$dy_{collimator} = dy_{coll.entrance} + c_{n.axis} \cdot (dy_{coll.exit} - dy_{coll.entrance})$$

$$dy_{opt.axis} = dy_{cam.exit} + d\alpha_{camera} \cdot (\, z[detector] - z[cam.exit] \,)$$

leads to an image move on the detector of

$$dy_{total} = \frac{1}{m} \cdot dy_{collimator} - f_{camera} \cdot d\alpha_{camera} - (dy_{detector} - dy_{opt.axis})\,.$$

This expression was found to be fully sufficient for addressing the effective image shift on the detector. The accuracy obtained this way was within 1 micron of the residual shift. Table 5.1 lists a sample of decenter and tilt, out of dozens of calculated design modifications, and the residual image shift that was obtained with two different methods, the analytical approach (done by us) and the detailed ray-tracing of our colleagues in Heidelberg taking into account each single optical element. The latter estimate is based on the finite-element and ray-tracing analyses, done with the ALGOR and ANSYS software in combination with the CODE-V and ZEMAX ray tracing program. The optical design software accounts for each three-dimensional position and tilt error, affecting image shift as well as image quality.

From the designer's point of view, the passive compensation should work with the correct stiffness properties in the housing structure as outlined in the next chapter.

Model	Obs.	Collimator		Camera		Detector	Image shift	Ray trace
No.	mode	dy_{entr}	dy_{exit}	$d\alpha$	dy_{exit}	dy	analysis	result
D200FSP	SR	26.2μm	51.2μm	7''9	64.9μm	72.9μm	-1.38μm	-1.28μm
D200FSN	SR	-18.7μm	-43.2μm	-7''9	-64.9μm	-72.9μm	+3.20μm	+3.07μm
D2P9FSP	SR	22.6μm	45.9μm	7''3	64.4μm	71.3μm	-1.13μm	-0.87μm
D2P9FSN	SR	-22.4μm	-45.9μm	-7''3	-64.4μm	-71.3μm	+1.13μm	+0.87μm
T200FHP	HR	20.2μm	32.3μm	7''9	64.9μm	72.9μm	-3.13μm	-3.28μm
T200FHN	HR	-39.7μm	-50.8μm	-7''9	-64.9μm	-72.9μm	-5.77μm	-5.47μm
T2P9FHP	HR	27.9μm	40.0μm	7''3	64.4μm	71.3μm	+1.77μm	+1.59μm
T2P9FHN	HR	-28.3μm	-40.0μm	-7''3	-64.4μm	-71.3μm	-1.96μm	-2.17μm

with f_{SR}=1232 mm, f_{HR}=616 mm, f_{camera}=280 mm and Δz=177 mm and

neutral-axis coefficients $c_{n.axis}$= 0.809 in SR and $c_{n.axis}$= $-$ 0.066 in HR mode.

Table 5.1: Residual image shift of the flexure compensation in the analytical approach, compared with the ray-tracing results. Both types of analysis lead to identical residuals within tenths of a micron. The value of the neutral-axis coefficient indicates the bias that collimator tilt causes due to separation of neutral axis from the collimator entrance lens and to the effective refractive power. In case of the HR-collimator, the neutral rotation axis is located close but in front of the entrance lens thus leading to a negative sign in this formulation. Displayed are the results of the final finite-element full computer models (D20/T20) for the two imaging modes (SR/HR), two position angles (0°/90°) and a positive and a negative (P/N) gravity vector. All together, the cases do simulate the loads of horizontal pointing in all four directions, North, West, South and East, covering the two principle symmetry planes of the instrument with opposite lateral loads.

5.1.2 Thermal constraints

The experience with former large telescopes – especially with the ESO 3.6-m – and the high imaging quality, expected from the telescope's active optics, put very high demands on the thermal control of the telescope environment. A well known source of internal seeing, affecting largely the original imaging quality of the site, are the thermal mismatch of primary mirror and of the dome interior with the ambient air. Therefore, a thermal budget of heat dissipation was specified for any single telescope component that includes the primary mirror, the dome environment and the instruments therein. The heat dissipation of each single component was supervised on its matching with the budget and after installation also tested with a thermal-infrared camera. The maximum thermal load of the telescope and dome environment by attached instruments is specified to

- total power dissipation ≤ 100 Watt

- hot spots on the instrument and cabinets ≤ 1°C above ambient temperature.

Heat dissipation sources

Different sources of heat dissipation enter the dome environment with an instrument,

- electrical motors of the driving units,

- mechanical gears, spindles and worm gears,

- servo control electronics and

- cabinets, housing the electronics.

A thermal assessment of each single heat source did confirm, that the drive units work too short (on average of every quarter hour) to heat up significantly because the drive units were attached to large masses with a high dissipation rate. The same is valid for the mechanical driving gears, with one exception that will be addressed later as a possible source for internal seeing. The servo control electronics could be excluded as negligible, at least those parts that are mounted inside of the instrument or the drive units. The only real heating source, that was identified in the assessment, were the cabinets that house almost entirely the electronics to control the fifty-three moving functions of the FORS instrument.

Insulating the cabinets

With a power consumption of about 4 KW to the maximum, it became obviously, that the control electronics, distributed over four cabinets, must be separated and thermally isolated from the rest of the instrument. On the other hand, the cabling of the numerous functions requires a co-moving of the cabinets with the instrument during telescope slew and tracking. The capacity of the instrument's de-rotating cable wrap was too small to cover such an enormous cabling. Therefore, the cabinets had to be sealed thermally with thick insulation layers before mounting them onto the instrument housing. The dome environment was protected by insulating all

surfaces of the cabinet structure. Nevertheless, the attachments to the housing structure had to isolated from their mounts through plastic inserts that prevent the heat from escaping the cabinet into the instrument. There remained only one minor source of leakage, that were the four screws made of steel but with moderate cross-sections that were mandatory to bolt the 100 kg cabinets safely to the instrument.

Heat exchangers inside each cabinet transfer the dissipated electrical power from the air, sealed inside the cabinet, into a liquid coolant. This coolant will then direct the dissipated heat through a cable de-rotator away from instrument and telescope, out of the dome into exhausters, hundreds of metres away, downstream of the prevailing wind direction.

Instrumental seeing

One point of concern was the possible induction of 'internal' seeing inside of the instrument which would affect the high fidelity of the instrument in maintaining the superb imaging quality, delivered by the telescope's active optics. Any source, generating possibly heat inside of the instrument, was therefore checked on dissipating electrical or mechanical power due to friction.

The control electronics inside of the instrument have a power consumption that is (more or less) comparable to that of a light-emitting-diode. The need for power exists only at the electro-mechanical drive unit of each function. Due to the conditions on maintainability, all electrical drives were moved to the outside of the instrument housing. Though, they give no longer any raise of concern because they were mounted to the large mass and surface of the housing which is exposed to the air stream, freely flowing through the dome.

The gears and spindles are driving only low mass components at a 90 % high transmission efficiency, so that frictional dissipation is negligible here. Relatively high power was only needed at the worm gear, driving the large filterwheels. They position the wheels, each with 70 kg of moving mass, with micron accuracy within the beam. This positioning has to be done free from any play, thus pre-loading the worm gear with a spring load became necessary. The gear was made from a special plastic (Delrin of the poly-acetal POM group) to prevent any lubrication of this sensitive area, next to the very expensive analyzing optics. This mean did reduce the efficiency drastically, that the worm gears dissipate a large amount of the drive's 40 Watt electrical power. Long term continuous operation of this drive thus would heat up the worm gear to about 60°C which was tested at the hardware.

In order to avoid such or even quasi-continuous operation, the filterwheels are routinely operated in an intermittent and optimized mode. Filters and grisms were changed between exposures, those last 5–30 minutes in the mean. Then, the wheels move the shortest way to replace the filter or grism by the next one which is mounted routinely in the adjacent position. Through this optimized operation is it not possible to heat up the worm gear significantly which could be confirmed by testing the original hardware under realistic pre-load.

Thermal analysis

We performed two thermal analyses, one on the mechanical and one on the optical properties. The optical analysis with the ray tracing program in Heidelberg showed that an optical bench made from aluminum will match the shift of optics at the best when ambient temperature

changes.

The mechanical design tried to avoid a mixture of material properties, for instance thermal expansion. This goal had to be violated since it was not possible to built the instrument entirely in steel as the telescope flange was made from. The stringent constraints in momentum and mass acting onto the telescope's flange and mirror cell forbid this. The limited maximum momentum was more critical than the weight constraint. This led to the solution that the sections, closer to the instrument's back end, were made from aluminum. The FORS instruments are therefore made of dual-material, steel at the front and aluminum at the rear part.

We designed a clean interface between both materials that was defined by dividing the collimator section at the centre of the instrument in two halfs. This intermediate flange between the front and the back half of the collimator section did not contain any symmetry-braking or other interfering structural parts within its circular geometry. The finite-element analysis did fully confirm that absolutely no deformation or displacement had to be expected from the difference in thermal expansion coefficient due to the circular, symmetrical and undisturbed clear interface.

The same behaviour was observed at the two collimator tubes. For optically matching reasons, mentioned above, they had to be built from aluminum. But for stability reasons, they had to be mounted into an exchange carriage, made of steel. No deformation nor displacement could be observed for the collimators' imaging optics at temperature change, and the internal strain at both sides of the aluminum-steel interface were kept within acceptable limits.

Hardware testing

Since the thermal matching of the instrument with its environment is of great importance for the success of the telescope project, the calculated thermal dissipation and heating had to checked with real hardware tests. The power dissipation of the cabinets totals to some 70 Watt each. This estimate took into account the air temperature when the heat exchange reached thermal equilibrium, any loss through insulated surfaces and the leakage through the cabinet mounts and screws.

Pictures were taken with a thermal-infrared camera that confirm all surfaces of the instrument within the specified 2°C above ambient temperature. These thermal tests were repeated at the observatory under real conditions of about 12°C. The pictures taken so far confirmed the former test results as it is well documented in the commissioning report.

5.1.3 Earthquake stability

One specification, that was quite special for instrument designers, belongs to the seismic activity of the Paranal site that is located in one of the most active regions in the world. The site is explored thoroughly in that respect so that good seismic data of ground-acceleration exist. The different kinds of acceleration of the ground would be magnified through the dynamical response of the telescope structure that was estimated independently to a maximum of $3\,g$–$5\,g$ at the location of the Cassegrain adapter. The FORS instruments had to withstand these loads, generated by an earthquake and magnified by the telescope.

Telescope and instrument are dynamically decoupled because the lowest eigenfrequency of the

latter was estimated by the finite-element analysis to more than 70 Hz. Therefore, such amplified earthquake loads can thus be treated as quasi-static loads. The static analysis of FORS returned a safety margin of more than 80 times before reaching critical loads at the most sensitive locations that were identified at the housing section where the collimator drive is pre-loading the linear motion guide for stabilizing the image motion compensation. At more general locations, the safety margin reaches a factor of 200, before irreversible deformation will take place.

Taking into account the additional load of earthquakes, magnified by the telescope structure, there remains still a safety margin of a factor of 16–50 before a mechanical disaster will occur. This margin is far above those values which are required in standard safety regulations for lifting devices. From this point of view, no concern about the resistance of the instruments against earthquake loads exist.

5.1.4 Reliability and maintainability

High demands were set on the reliability of the instrument as total as well on its maintainability in order to minimize the down-time of the instrument together with the telescope. The contract with ESO specified the following intervals and time consumption for possible repairs as a maximum.

- 3–6 man-hours once every three months,

- 1 day of repair once every six months without any loss of an observing night,

- 2–3 days of repair once per year to the maximum,

- All these figures have to be matched during an instrument lifetime of at least 10 years.

With this demanding specification, special care had to be taken already during the design phase to make the instrument user-friendly through a stringent modular design of extraordinary high degree. A clear structuring was mandatory to follow the concept of line replaceable units – LRU's. They were used in the design wherever a failure due to wear or tear could be expected. The first address for this were all electro-mechanical moving parts.

The FORS instrument comprises in total fifty-three moving functions. All drive units were located outside of the instrument enclosure, with one exception, that is the camera focusing drive. Nevertheless, even this drive unit is designed to have it accessible from the outside for a quick replacement. Those electronic components, that must be mounted next to the moving function for closed loop operation and therefore located deep inside the instrument, were attached twice at each single function and work redundantly.

All driving mechanics were placed into individual cases to form units. The mechanics is designed in a way that the loads in ordinary operation will stay below a 20 % level. They are lubricated with a special grease that takes into account the special environment of the Paranal site with its very low humidity. They are also well protected against dust and aggressive silicate particles with a double-shielding through the instrument housing and internal encasing. The assessment of the mean-time-between-failure (MTBF) showed that not wear and tear nor the reliability of mechanical functions would fall below the anticipated 10 year lifetime. But, the kind of intermittent operation together with long periods of non-operation in the stand-by mode – that

regularly will take place around the full moon phase for a 'dark-time' instrument – did raise concern. This will be compensated by a procedure that will set-up the instrument into different configurations on a regular basis. Nevertheless, a check and re-lubrication of some specific parts – but no overhaul – is foreseen every two years.

That FORS fulfils the reliability specification, could already be demonstrated during the time of the testing period which did last almost two years for FORS1 and another one year for FORS2. Another operational period of about half a year of commissioning at the telescope add to this figure. In the meantime, both instruments are in routine operation at Paranal observatory without any major failure or malfunction for a long period. This fact supports that the assessment on reliability was correctly done.

Today's operation confirms that it was right to push the reliability specification to such high demands because the VLT, as a world class facility, ranks nowadays at highest rate of reliability due to its very low amount in engineering down-time and high amounts in shutter-open time of each single instrument. Both are unrivaled under earthbound telescopes so far.

5.2   Realisation

5.2.1   General

The following section will address that part of the instrument that was put into hardware by the team of Göttingen Observatory, led by myself with the responsibility in matching both, the technical and the observational specifications. At the end of the section, one will see that all of them have been fulfilled with an adequate or even higher quality.

We did face challenging tasks throughout the course of the project when we did manufacture, procure, integrate and thoroughly test to improve the instrument hardware. Describing all these issues in detail would go beyond the scope of this thesis. Therefore, we will display and list comprehensively all units in a summarizing form that became relevant for the multimode character of this instrument.

Only one of the numerous tasks, the flexure compensation of the image motion will be addressed in larger detail due to its large impact on design and instrument performance. It was this issue, which failed in a focal reducing instrument at another competing very large telescope. This issue shall stand representatively for all the other tasks in order to match the requirements, either given by the customer's contract or deduced internally by the VIC consortium itself, the first potential user of the instrument.

5.2.2   Total view drawing

Figure 5.1 gives a total view of the design how it was realized in two copies of the FORS instruments. Visible are all instrument units and modules except for the mask exchange unit (MXU) which is special only for FORS2 and is hidden in this section view. Please compare this detailed with the schematic view, given in Fig. 3.1, for a better understanding of the following description.
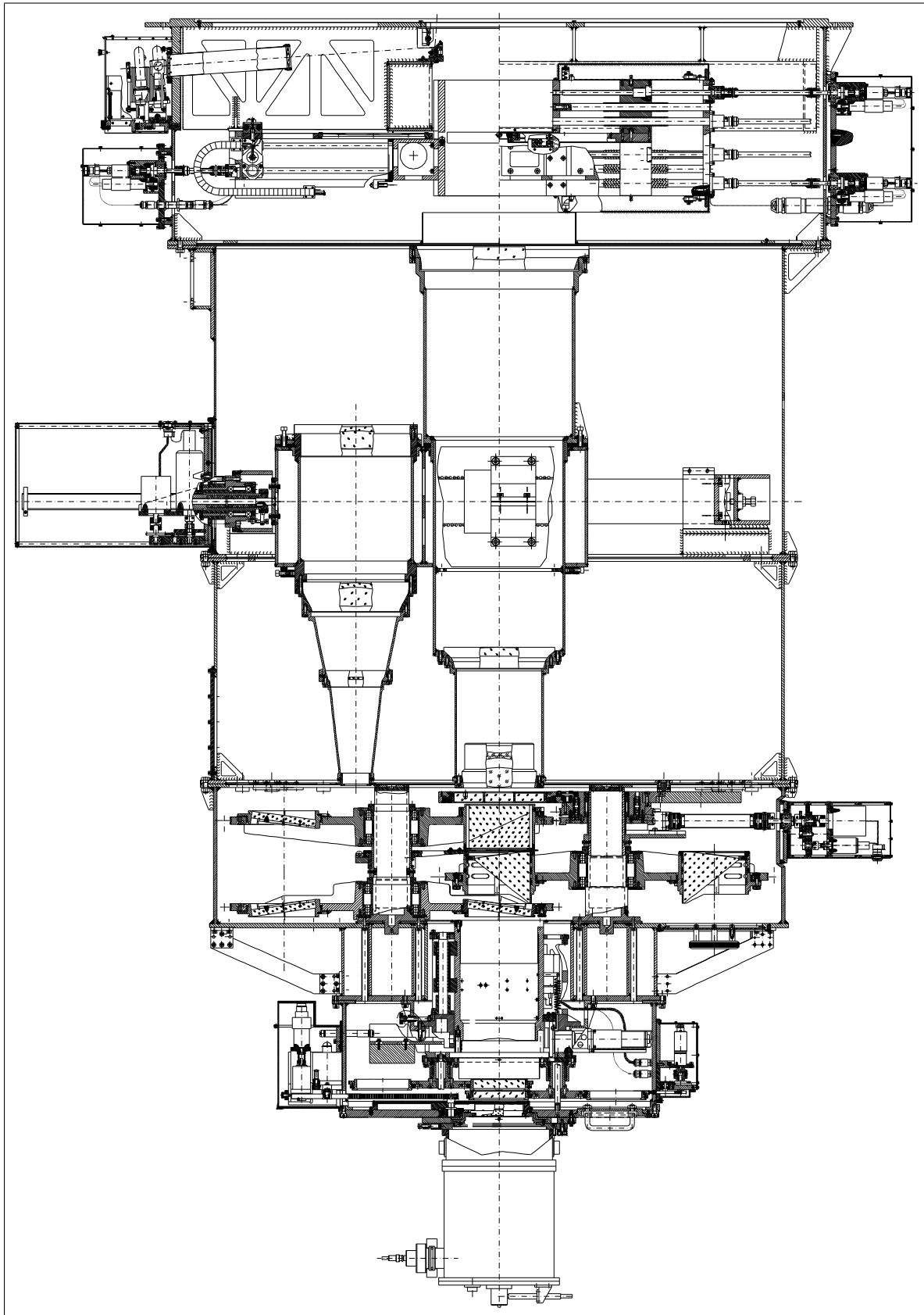
Figure 5.1: Section view of the FORS focal-reducer and spectrograph as it is realized in two copies for the ESO/VLT at Paranal Observatory in northern Chile.

One half of the symmetric MOS unit with movable slitlets can clearly be identified to the right inside of the top section. The drive modules are attached at the outside housing to each individual slit-jaw carrier. The longslit unit and the calibration unit can be identified left to the optical axis in the top section. Both were drawn at 90°rotated to make them visible in this section view because the motion of longslit and MOS slitlets crosses each other in the focal plane.

The central section contains the double-collimator, one for standard and one for high spatial resolution imaging. Both, the large SR and the smaller HR collimator, rest in their linear exchange carriage. The frame, that surrounds the carriage and contains the linear motion guides, can be seen at both sides of the exchange carriage. To the left, the spindle drive with the largest power of all is mounted to that frame work without contacting the housing. It will pre-load the carriage within its frame for a stiff fixation at both end points after exchange motion.

One of most complex sections, crowded with units and modules, is the so-called filter/camera section at the instrument's back, just in front of the very last unit, the detector cryostat. The filter/camera section is the heart of the instrument where all analyzing elements will be inserted into the optical beam. All five filterwheels – three large ones, moving the broadband filters, grisms and Wollaston prism and two smaller ones for narrow-band filters in front of the cryostat – are identified with their large diameter, filling the size of the filter and of the camera section's housing entirely. Only one of the three drives is drawn to the right, fixed to the filter section housing. Between the two sets of large and small filterwheels, the camera optics with its focusing mechanism is visible. The focusing drive and a balancing mechanism for the camera are visible at both sides of the camera optics inside of the housing. The two drive units at either side of the smallest, the camera housing, drive the narrow-band filter wheel and the camera exposure shutter at the instrument's end.

The detector unit within its cryostat is mounted to that plate, closing the instrument at its end and giving access to the narrow-band filters for exchange. The stiffening diagonals, connecting the filter with the camera section at the outside of the housing, are visible around the periphery where the large diameter of the housing steps into a smaller one. Those diagonals are the most crucial parts in tuning and adapting the stiffness which led to an optimum in compensating image motion due to instrumental flexure.

The final realization of the two FORS instruments offer the observer the following observing modes, that utilizes either single opto-mechanical units or a combination of several of them. We want to emphasize, that tremendous efforts were made to push the instrument design to its limits in flexibility of combining a maximum of independent observing modes.

1. Broadband filter imaging with two imaging scales, SR and HR,

2. Multiple-Object-Spectroscopy through MOS (and MXU) spectroscopy at two spatial scales,

3. Longslit spectroscopy at numerous spectral and two spatial resolutions,

4. High-time-resolution imaging and spectroscopy through modified longslit mask,

5. Polarimetric imaging in two polarization states (linear & circular) with two spatial resolution scales,

6. Polarimetric spectroscopy in two polarization states (linear & circular) with numerous spectral and two spatial resolutions,

7. Narrowband filter imaging in two spatial resolution scales, despite the large oblique angle of incidence in the parallel beam section.

This high degree in the flexibility of combining all these modes justified in the end the denotation of FORS as the 'Workhorse' of the VLT.

5.2.3 Instrument Units

We will summarize in the following section the instrument as it was realized at the end through the team at Göttingen Observatory. It will list all the units and major modules, most of them already mentioned throughout the text. We will concentrate solely on the mechanical capabilities that were personally covered by my responsibility at Göttingen Observatory. The numerous interfaces and interactions with the instrument optics and electronics are not addressed here.

All instrument parameters are listed that were finally realized and confirmed through real hardware tests. These parameters characterize the FORS instrument mechanics and their outstanding capabilities, those unrivalled by other focal reducers in their performance so far.

- Entrance and Emergency Shutter   (automatically closing in case of failure)

- Multiple-Object-Spectroscopy – MOS Unit

    - Field of view; full 228×288 mm field in SR (and HR) mode supported
    - Slits; 19 individual slitlets, formed by 38 movable slit carriers of 250 mm length
    - Slitlength 12 mm or $22\rlap{.}''5$ on the sky at 0.5 mm/arcsec telescopic scale
    - Slit pattern setup-time; typically 22 sec
    - Slit quality
        * Positioning accuracy; $< \pm 10 \,\mu$m corresp. $0\rlap{.}''02$
        * Minimum width; $150 \,\mu$m or $0\rlap{.}''3$
        * Width variation; $< \pm 5\%$ corresp. $10 \,\mu$m
        * Edge straightness; $\pm 0.5 \,\mu$m at $0.2 \,\mu$m roughness
        * Edge parallelism; 2–$3 \,\mu$m

- Mask Exchange Unit – MXU   (FORS2 only)

    - Design; late add-on to the MOS mode, after the FDR and housing procurement
    - Field of view; full 228×288 mm field in SR (and HR) mode supported
    - Multi slit capacity; up to maximum of 100 slits per mask, laser-cut with a separate Mask Manufacturing Unit MMU
    - Magazine capacity; 10 framed masks to the maximum in storage magazine
    - Observing potential; up to 1 000 objects per night (and even higher) to spectroscopy
    - Dimensions;(LxWxH) 415x325x360 mm at 30 kg full weight, fully equipped with masks

- Add-on incorporation; unit fits snugly into instrument space, left inside the top section after remove of the polarimetric obscuring mask for HR

- Longslit set with decker masking Unit

  - Field; full field support of SR (and HR) mode at $228\,\text{mm}$ corresp. $7\!'\!.1$
  - Slit number; 9 in total, selected by decker mechanism
  - Widths; $0.15 - 1.25\,\text{mm}$ corresp. $0\!''\!.28$, $0\!''\!.4$, $0\!''\!.51$, $0\!''\!.7$, $1\!''\!.0$, $1\!''\!.31$, $1\!''\!.6$, $2\!''\!.0$, $2\!''\!.5$
  - Edge straightness; $\leq \pm 10\,\mu\text{m}$
  - Edge parallelism; $\leq \pm 12\,\mu\text{m}$
  - Curvature; optimally focused by bending the longslits to the focal 'plane' curvature of $2\,070\,\text{mm}$ radius

- Polarimetry Masking Unit

  - SR imaging mode; full $220\,\text{mm}$ field support by generating the masking $12\,\text{mm}$ strips with slit carriers of the MOS Unit
  - SR spectro-polarimetry mode; full field support through generating $12\,\text{mm}$ strips and slitlets by the MOS Unit
  - HR imaging mode; full $110\,\text{mm}$ field support by obscuring strip mask of $6\,\mu\text{m}$ strip widths
  - HR spectro-polarimetry mode; full field support by masking out $6\,\text{mm}$ strips and slitlets generated by the MXU

- High Time Resolution HIT – Mask

  - Part of the longslit masking Unit
  - A special gap and decker design enables this type of observation

- Calibration Units

  - Calibration sources; up to max. 12 light sources, without any exchange
  - Projection optics; 6 beams for screen illumination
  - Spectral lamps; 2x Helium, 2x Neon, 2x Argon
  - Flat fielding lamps; Quartz tungsten halogen lamps, 4x blue- and 4x un-filtered

- Top Section Housing Structure

  - Structural functions; mounting & housing focal plane equipment and facilities
  - Total size; $1\,580\,\text{mm}$ diameter, $496\,\text{mm}$ length
  - Total weight and momentum incl. section units; $772\,\text{kg}$ at $1\,530\,\text{Nm}$

- SR Collimator Unit

  - Structure; stiff cylindrical tube as optical bench for the refracting optics
  - Alignment; precisely machined mounts, that after optics insert no further alignment necessary
  - Straylight baffling; stacked tree of baffling light stops

- Interface; stiff flange attachment to the exchange unit with precision seat

- HR Collimator Unit

  - Structure; stiff cylindrical tube as optical bench for the refracting optics
  - Alignment; precisely machined mounts, that after optics insert no further alignment necessary
  - Straylight baffling; stacked tree of baffling light stops
  - Interface; stiff flange attachment to the exchange unit with precision seat

- Collimator Exchange Unit

  - Functions; high-precision exchange SR and HR collimator optics within optical beam and focusing them onto telescope's focal plane
  - Repetition accuracy; $100\,\mu$m or 2 pixel typically
  - Motion type; linear motion guide on $100\,$mm cylinders with $6\,$mm bearing balls
  - Fixation type; pre-loading carriage within stiff framework against physical motion stops at the two opposite end positions
  - Drive type; spindle drive combined with selflocking worm gear, attached to the framework without contact to the housing structure
  - Total moving weight incl. collimator optics; $280\,$kg

- Collimator Section Housing Structure

  - Structural function; interfacing the instrument's steel with the aluminum part
  - Total size; $1\,480\,$mm diameter, $1\,202\,$mm length
  - Total weight and momentum incl. section units; $953\,$kg at $8\,830\,$Nm

- Parallel Beam Section Units

  - Functions; three wheels and additional swing arm for optics exchange
  - Filter capacity; 3 wheels, each offering 7 (+1 clear) positions

    1. Polarization swing arm; accommodating two phase-retarder mosaics, up to $20\,$mm thick
    2. Filterwheel I; Wollaston prism + filters + grisms, $95\,$mm max. thickness
    3. Filterwheel II; grisms, $115\,$mm max. thickness
    4. Filterwheel III; inclined filter optics, $15\,$mm max. thickness (plus $20\,$mm tilt)

  - Filling factor; $265\,$mm out of $295\,$mm parallel beam section, in total 90% is available for the analyzing optics alone
  - Physical dimensions; optics max. diameter $140 - 146\,$mm
  - Positioning accuracy; $\leq 0°\!.1$
  - Adjustment; mechanical fine tuning of grisms and Wollaston prism within their mount by rotational alignment of dispersing direction with CCD matrix
  - Repetition accuracy in position angle; $10''$corresp. $1/10$ pixel along full spectrum length

- Failure protection; insert positions and mounts were hardware coded against collisions
- Handling safety; dedicated handling tools for each type of analyzing optics; Wollaston prism, grisms, filters
- Optics protection; unlubricated worm gear, running on special plastics
- Drive type; worm gear driven, free of any play due to pre-loading

- **Pupil Stop**

  - Size; clearance of 105 mm for the parallel optical beam
  - Type; obscuring metal plate with sharp edges, preventing straylight
  - Functions; rotational adjusting mechanism for alignment with beam position

- **Camera Focusing Unit**

  - Functions; fixing the refractive elements and groups within optical beam and focusing parallel beam onto detector plane
  - Focusing range from nominal position; totally $+2.5$ mm to -9.5 mm
  - Mechanical solution; linearly driven by 80 mm large eccentric disk of 6 mm rotary displacement
  - Focusing step size; $< 10\,\mu$m
  - Repetition accuracy; $\pm 1\,\mu$m
  - Camera tilt due to bending; reduced from $8''$ to $1''$
  - Momentum compensation; 5 kg dead weight, counter-balancing the camera optics via a weak fork for equal load distribution
  - Drive type; un-loaded selflocking gear
  - Total moving weight incl.optics and balancing weight; 33 kg

- **Narrowband Filter Wheel Units**

  - Filter capacity; 2 wheels, each offering 4 (+1 clear) positions
  - Optical properties; blue-shift of IF-filters avoided down to 1.2 nm, widening of transmission curve in the wings reduced to 0.2 nm at FWHM or 4% and a relative transmission of 95% (SR) and 90% (HR) at maximum
  - Capacity in physical length; 15 & 20 mm max. thickness
  - Beam size; 116 & 112 mm, free of any vignetting

- **Camera Exposure Shutter Unit**

  - Type; chopper, uni-directionally rotating plate segment
  - Optics beam diameter; max. 80 mm
  - Shortest exposure time; 1 second
  - Photometric accuracy; ± 10 millisec corresp. 1%
  - Light tight; better than 10^{-10} attenuation

- **Detector Flange Attachment Unit**

- Isolates the detector electrically from the instrument's grounding
- Adjusting the detector plane (and refractive field lens) in all six degrees of freedom
  * X,Y $\pm 2\mu$m shift and fixation mechanism and thereafter re-centring with a perfectly matching conical shoulder, free of any play
  * Z longitudinal fine-tuning via a separate spacer ring
  * U, V tilt adjustment for a detector parallel to focal plane via a separate space ring
  * W rotational alignment ($\pm 3°$) of CCD matrix with the direction of the MOS slitlets, the longslits and polarimetric strip mask via a lever fixation system

- **Filter/Camera Section Housing Structure**
  - Total size; $1\,332/744$ mm diameter, $483/261$ mm length
  - Total weight and momentum incl. section units; 400 kg at $7\,900$ Nm

- **Instrument internal Baffling**
  - Baffling type; four levels for preventing ghosts and straylight
    1. Sharp edges, wherever mechanical stops destroy light rays
    2. Lighttight interconnection between each of the four section (except beam itself)
    3. Internal additional baffling within instrument units; MOS, collimators, camera
    4. Black optics paint on all surfaces inside of the instrument housing and units, destroying straylight rays if originated despite the above preventive means

- **Instrument Service Connection Point – ICP**
  - Counterpart to the Service Connection Point SCP on the telescope's mirror cell
  - Central distribution point for data, energy and cooling lines on instrument side
  - Fixes the cable guidance, counterpart of the tripod-leg structure on instrument side

- **Cabinet mounts of electronics**
  - Fork mount with momentum support for four cabinets, 70 kg each
  - Integral part of collimator section without flexure deformation

- **Instrument (in total)**
  - Image quality, maintained by mechanical structure and mounts;
    * Light concentration in SR mode; 70% within 1 pixel and $> 90\%$ within 2x2 pixel up to $4'$ field radius in all Bessel-U,B,V,R,I filters
    * Light concentration in HR mode; 70% within 1 pixel and $> 90\%$ within 2x2 pixel up to $2'$ field radius in all Bessel-U,B,V,R,I filters
    * Light concentration in polychromatic (spectroscopic) mode; 70% within 2x2 pixel and $> 90\%$ within 3x3 pixel
    * Light concentration in polarimetric SR and HR mode; 80% within $0\rlap{.}''5$
    * Linear polarization accuracy; $\lambda/4 \pm 1.5\%$
    * Circular polarization accuracy; $\lambda/4 \pm 4\%$
    * Parasitic light suppression; $< 2\%$ sky concentration

- – Size; 2 800 mm diagonal diameter (incl. electronic cabinets),
  2 865 mm total length (incl. detector cryostat)
- – Weight and momentum; 2 250 kg at 19 980 Nm and 330 Nm axial torque

- Installations and Devices at the Telescope

  - – Tripod structure as cable wrap for de-rotation of energy chain, closed cycle cooling lines and data transfer fibres
  - – Handling device for Top Section incl. turning capabilities
  - – Handling devices for each optical component, filters, grisms and Wollaston prism
  - – Stand for attachment when the instrument, detached from telescope, is in storage
  - – Special tools for adjusting and centring mechanical and optical parts

The characteristics, given here, match all the specifications that were defined and independently tested and verified by the customer ESO. A comparison of the above characteristics and test results with the specifications – given in an excerpt format in Section 4.2 – revealed clearly that the contractually binding performance parameters were fully matched and partly over-fulfilled by casting the instrument design.

The most sophisticated units were already mentioned in different context in previous chapters, where the special issues and the specific solutions were outlined and to which the reader is referred to.

Chapter 6

Structural analysis by finite-element methods

6.1 The analytical approach

Due to the lack of finite-element-analysis software during the early phase of the project, an
analytical approach for assessing the flexibility of the instrument structure was performed. Three
different models were made; one with the instrument mass uniformly distributed along the
centre axis of a cylindrical beam of constant stiffness, the second with the instrument mass
and the stiffness split into three different components according to the three main sections of
the preliminary design and the third of the highest detail taking additionally into account the
shearing deformation. All three approaches led to fairly similar results which were issued in
the design proposal for constructing the FORS imager and spectrographs. These analytical
approaches did convince the reviewers that the idea of passive flexure compensation is basically
able to compensate the expected image shifts to negligible residual amount.

6.1.1 Simple cantilevered beam

In the first approach for getting a rough guess of flexure compensation, a very simple model of the
instrument mechanics was applied. The total instrument was modelled as a simple cantilevered
beam. The polar moment of inertia of that beam was calculated accordingly to a beam of
cylindrical shape, made of thin plates. The instrument was modelled with a cylinder of $1.5\,\mathrm{m}$
diameter, $2.3\,\mathrm{m}$ length and $15\,\mathrm{mm}$ aluminium plates. The total mass was distributed uniformly
along the cylindrical beam.

According to Hooke's law (with assuming a non-deforming cross-section i.e. shearing strain not
taken into account), one can describe the curvature of a beam under the bending momentum
M_b in Euler's formulation

$$\frac{y''(z)}{(1 + y'^2(z))^{\frac{3}{2}}} = -\frac{M_b(z)}{E\ I_y(z)}$$

according to [20]. For small amounts of bending $y'^2(z) \ll 1$ and for a *constant* polar momentum

of inertia $I_y(z) = I_y$, the linearised differential equation simplifies to

$$y'(z) = \alpha(z) = -\frac{1}{E \, I_y} \int\limits_0^l M_b(z) \, dz$$

$$y(z) = \int\limits_0^l \left[-\frac{1}{E \, I_y} f(z) + c_1 \right] \, dz \; .$$

The constants of the integral are determined by the boundary conditions for a cantilevered beam to $y(0) = 0, y'(0) = 0, y''(l) = 0, y'''(l) = 0$.

The analytical approach of a simple cantilevered beam with the continuous load g, length l, Young's modulus E and the neutral axis along z follows then

$$y(z) = \frac{g \, l^3}{24 \, E \, I_y} \left[3 - 4 \left(\frac{l-z}{l} \right) + \left(\frac{l-z}{l} \right)^4 \right]$$

$$\alpha(z) = \frac{g \, l^2}{6 \, E \, I_y} \left[\left(\frac{l-z}{l} \right)^3 - 1 \right]$$

with the polar moment of inertia of plate thickness s to

$$I_y = I_x = \frac{\pi (D^4 - d^4)}{64} = \pi \, s \, r^3 \; .$$

This function describes the displacement and tilt for collimator and camera optics. Both amounts, estimated with this function, were inserted into the relationship of flexure compensation (Sec. 5.1.1). This resulted in an residual image shift of $2.9 \, \mu$m, listed individually in Tab. 6.1. This gave the first hint that flexure compensation would work properly for the design, proposed by us.

6.1.2   Beam superposition

This model was analyzed in the next step in more detail by taking into account the mass and stiffness of each of the three main sections. The mass of each individual section was spread uniformly along the symmetry axis of the section. The bending and tilt was then calculated for each individual section in the same way as it was done for the first, the very simple model but applying the mass and the polar momentum of inertia of each single section specifically to their corresponding plate thickness. The latter decreased from $20 \, $mm for the top section at instrument's front end, $12 \, $mm at the collimator to $5 \, $mm at the filter/camera section in order to reduce the total momentum acting on the telescope attachment flange. This procedure took into account the momentum, decreasing along the instrument axis toward its back end. The result of each specific calculation was then superpositioned through linking the common flanges, taking the results of the forefront section as boundary condition for the subsequent section. The individual and the effective result of that superposition are listed in Tab. 6.2. The residual image shift of $2.3 \, \mu$m is well within the specification of $6 \, \mu$m. Although the assumptions for both models are quite different according mass distribution and stiffness, the analyses led to astonishingly similar results.

Optical components	Displacement	Tilt	Resulting image shift
Common flange Top/Coll.-Section	$10.8\,\mu$m	$1\overset{''}{.}4$	–
Collimator neutral axis	$26.0\,\mu$m	$2\overset{''}{.}1$	$+\,5.9\,\mu$m
Camera focussing mechanism	$33.6\,\mu$m	$2\overset{''}{.}2$	$-\,3.0\,\mu$m
Detector focal plane	$37.4\,\mu$m	$2\overset{''}{.}2$	–
Flexure compensated **residual** image shift			$+\,\textbf{2.9}\,\mu\textbf{m}$

Table 6.1: Residual image shift of the analytical approach of the bending of a cantilevered beam. The total mass is spread continuously along the symmetry axis of a cylindrical aluminium tube of a mean 15 mm constant thickness.

Optical components	Displacement	Tilt	Resulting image shift
Common flange Top/Coll.-Section	$7.6\,\mu$m	$0\overset{''}{.}9$	–
Collimator neutral axis	$21.7\,\mu$m	$1\overset{''}{.}7$	$+\,4.9\,\mu$m
Camera focussing mechanism	$29.2\,\mu$m	$1\overset{''}{.}9$	$-\,2.6\,\mu$m
Detector focal plane	$32.8\,\mu$m	$1\overset{''}{.}9$	–
Flexure compensated **residual** image shift			$+\,\textbf{2.3}\,\mu\textbf{m}$

Table 6.2: Residual image shift of the analytical approach of the bending of three cantilevered beams of different mass (550, 800 and 300 kg) and plate thickness (20, 12 and 8 mm) through superpositioning the displacements and tilts of the three individuals, the top, collimator and the camera section.

A comparison of the two analytical approaches (Tab. 6.1 and 6.2) exhibits that flexure compensation is very robust. It reacts very relaxed on different amounts of displacement and tilts, as long as proportionality of displacements and tilts is maintained. The latter is identical to the conservation of curvature.

6.1.3 Superposition with shear deformation

The third approach took the shearing deformation of each cylindrical housing into account, additional to the former displacement and tilt of the individual sections. This advanced method did not show any further significant impact on the residual image shift. Thus, the second analytical superposition approach had been regarded as sufficiently detailed for the instrument proposal. The principle of passive flexure compensation is very robust since earth's gravity guarantees for the curvature of the beam and the right sign in bending and tilt of all the components along the symmetry axis. Although the analytical approach was sufficient for a design proposal, it had to be re-checked and confirmed by a detailed finite-element-analysis (FEA), that was performed throughout the two subsequent phases of preliminary and final design.

6.2 Finite element analysis

6.2.1 Finite-element model

The finite-element-analysis was performed with the *Algor Inc.* software package, for which the analyses of the Keck 10-m telescope through this software applied as a reference project. At a later stage, the *ANSYS* software was used in the manufacturing phase for more detailed studies and for the data exchange with the contractor. The *Algor* software did base on the Intel-386 CPU-hardware and the Microsoft DOS operating system, both available at that days when the analyses took place. They did, together with the available memory, define the computational boundaries in modelling structural details and limited the spatial resolution of the instrument units to marginal values.

The model with the highest mesh density, that required a run-time of about six hours, contained 5 755 nodes and 4 940 elements which lead to the order of 30 000 degrees of freedom. They produce the so-called total stiffness matrix of the system that has a diagonal band-structure in filling the positions with stiffness coefficients, depending on the type of elements and their formulation. Numerous algorithms were proposed to reduce this bandwidth and to minimize the total stiffness matrix – for instance by eliminating inner degrees of freedom – into a condensed stiffness matrix [21] which pushed the computing system to its limits. A few of the models did require more than 72^h of elapsed computing time in the case study when replacing linear link elements by the non-linear formulation of gap elements [22]. Such time and memory constraints limited the number and the kind of modifications that could be applied to the models in order to identify week points and to optimize the instrument structures.

The number of nodes define the mesh density that can be applied to specific parts and locations within the instrument. More nodes had to be spent where higher resolution is needed to cover excessive or concentrated forces, whereas the cylindrical enclosure required only a fairly rough

mesh. The spatial resolution of the mesh could be doubled through the savings, gained by the axi-symmetric design of the structures. Since those nodes would move only within that symmetry plane and not perpendicular it, it did reduce the number of nodes to half of its original amount when applying the correct boundary conditions to that nodes in the symmetry plane. Nevertheless, one has to take into account the symmetry of the structure with respect to the actually acting gravitational load when constraining the six translational and rotational degrees of freedom. Thus, two models of any design modification had to be maintained since the instrument symmetry plane, common with the gravity vector, changes with the instrument's position angle. Those were applied to any design modification. After finalizing major design changes, a full model with all nodes imaging the instrument totally had to be computed due to the lack of symmetry in the camera focussing mechanism or in the dynamical and thermal analysis.

The software was able to apply several load cases (e.g. $1g_x, 1g_y, 1g_z$) to the model in a single run. This improvement – though calculating the stiffness matrix only once – was used to analyze the displacements at positive and negative gravitational force. Thus, the displacement and tilt of two opposite horizontal pointings could be obtained in a single run which is not a priori of the same absolute amount as it was verified by the values of Tab. 5.1.

The type of elements that were used in setting up the computer model did comprise

- plate (or shell) elements for about 95% of the instrument components like the housing structure and flanges, stiffening ribs and diagonals,

- brick (or solid) elements for all refractive optics and lens mounts and simulating any internal load by lumped mass e.g. for the electronic cabinets and the movable MOS slitlets,

- compression gap (non-linear) elements for simulating the linear motion guides of the collimator exchange and of the camera focussing mechanism.

All those can be identified in Fig. 6.1 showing one representative of the numerous *Algor* computer models. It is identical with the final design of the instrument [47] and demonstrates the density of the mesh that could be covered by the existing hard- and software.

6.2.2 Static analysis

The analysis of static stiffness was performed parallel to the development of the instrument mechanics during the two phases of preliminary and the final detailed design. Dozens of models were built and modified which delivered valuable hints for specific design details such as,

- how to attach the concentrated mass of the MOS unit to the housing structure,

- the attachment of the heavy electronic cabinets via fork mounts and their torque release through supporting legs,

- the internal flexural bending of the two collimator assemblies, assumed as infinitely stiff in the former analytical approach,
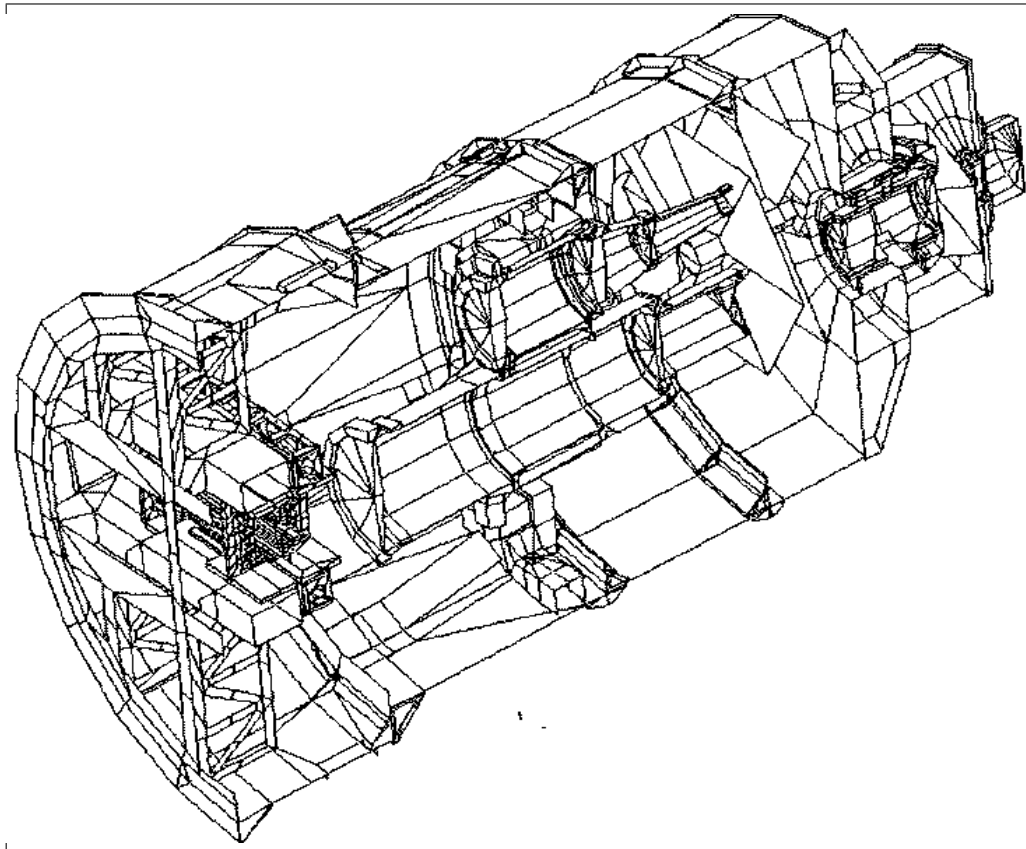
Figure 6.1: 3D-model of the FORS instrument built within the DOS/Algor environment for the Final Design Review. The sections and major units can be clearly identified (cf Fig. 3.1). Three different types of elements were used in the FEA model, shell/plate, solid/brick and non-linear gap elements.

- the decision for a linear instead of a rotary stage for the collimator exchange,

- the design and attachment of collimator's exchange mechanism,

- the displacement and tilt of the analysing optics (filters and dispersing grisms) due to bending of the filter wheel mounts,

- the introduction of a semi-spider structure into the filter section,

- the displacement and tilt of the camera focussing mechanism,

- the influence of the linear motion guides of collimator and camera on the flexure compensation,

- the detailed design of the camera section housing despite the lacking stiffness by inserting IF-filter wheels that cut the direct link between camera and detector and introduced additional image shift due to the detector tilt from the S-sag shape of the back-end plate,

- the re-stiffening of the instrument back-end within the optical constraint of positioning the IF-filter wheels next to the detector and field lens,

- the re-stiffening of the interface between filter and camera section in order to maintain the camera tilt for compensation,

- the stiff link between flanges and housing,

- the necessary stiffening of the housing itself,

- the local deformation and strain at the mounting plates, used for handling and link to the instrument transport cart,

- the stiff detailed design of the service openings for Wollaston, grism, filter and IF-filter exchange and last but not least

- the subsequent cutting and and framing of the access openings in the top section for servicing and maintaining the MXU mask exchanger, that was added to instrument after Final Design Review.

One special feature in the FEA model is the collimator exchange mechanism that was originally designed as a rotary stage. Attaching the axle of this 200 kg weighing unit to the housing did appear unfeasible because the local deformations of the housing at their mount led to unacceptable displacements of the twin collimators. Despite its amount in vertical space requirement, reserved for the analysing optics in the parallel beam section, it also led to a dependance in position angle, so that flexure compensation should fail with that kind of stage.

A linear motion stage was therefore designed that spread the load of that unit onto the housing through four attachment consoles (Fig. 6.2). These were located next to the interface flanges of the housing, acting effectively as a large re-stiffening rib and preventing the departure of the cylindrical enclosure from circular shape. Any further housing deformation was avoided through a direct link between collimator exchange mechanism and drive. The moving carriage was pre-loaded by 2 500 N spring force against physical stops at both end positions. This pre-load against the inner frame work, formed by the linear motion guides and the connecting beams, led to a re-stiffening of the entire exchange mechanism with accordingly small local deformations of

structure and housing. As a result, flexure compensation depends solely on the overall bending of the housing and not on local deformations, reduced to negligible amounts. Additionally, the electrical drive module is bolted to the exchange structure without loading the housing and becoming accessible from the outside for maintenance reasons.
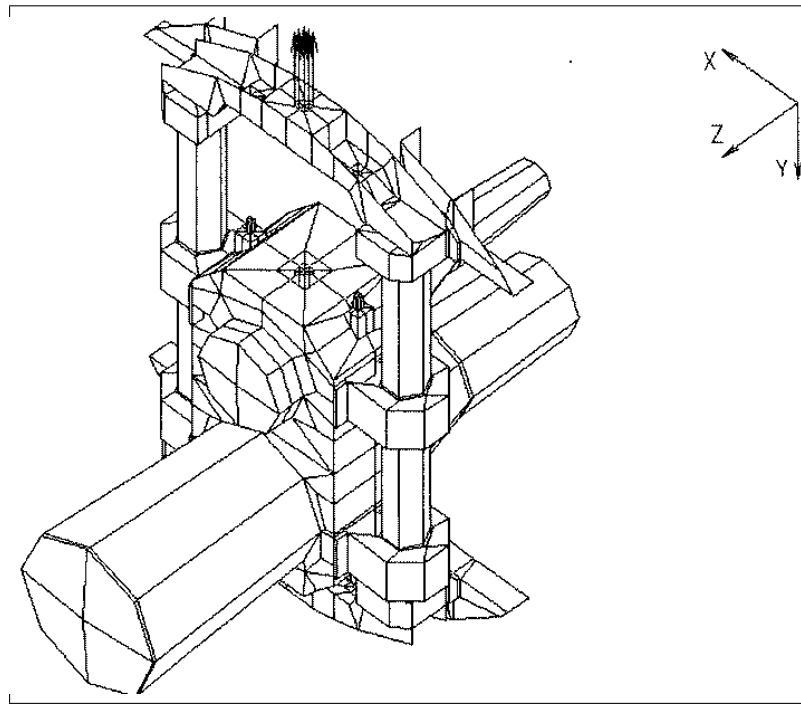

Figure 6.2: Detail of the FEA model. The collimator exchange mechanism is shown covering the support structure, linear motion guides, movable carriage with the tube and optics assembly as well as the end stops and the pre-loading force vectors.

6.2.3 Modal analysis

After the static analysis, the dynamics of instrument had to be estimated. First of all, a modal analysis was performed for that purpose. This type of FEA determines the eigenfrequencies of the instrument structure, at which it will step into resonance. These resonance frequencies will give first hints if the instrument would suffer under dynamical loads.

The modal analysis upon the instrument's eigenfrequencies turned out the following frequencies.

- eigenmode-1; filter wheel vibration at 72 Hz

- eigenmode-2; housing bending mode in Y-plane at 109 Hz

- eigenmode-3; housing pumping mode at 113 Hz

The lowest eigenfrequency of the instrument was determined to about 70 Hz at the filterwheels, but to more than 100 Hz for the more important structural of the instrument housing. This was far from being critical. The lowest resonance frequencies of the telescope, to which the instrument is attached and that could excite the instrument to resonance, fall into the range of
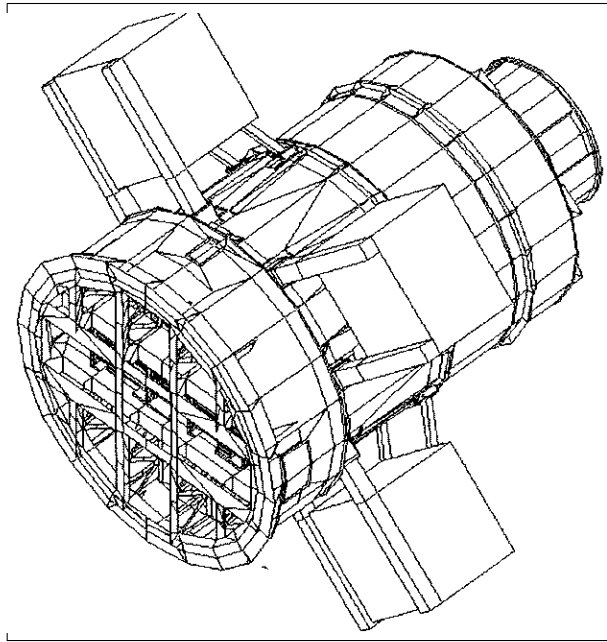
Figure 6.3: FEA model, displaying the global deformations of displacement and tilt. All deformations are largely exaggerated relative to the instrument dimensions.
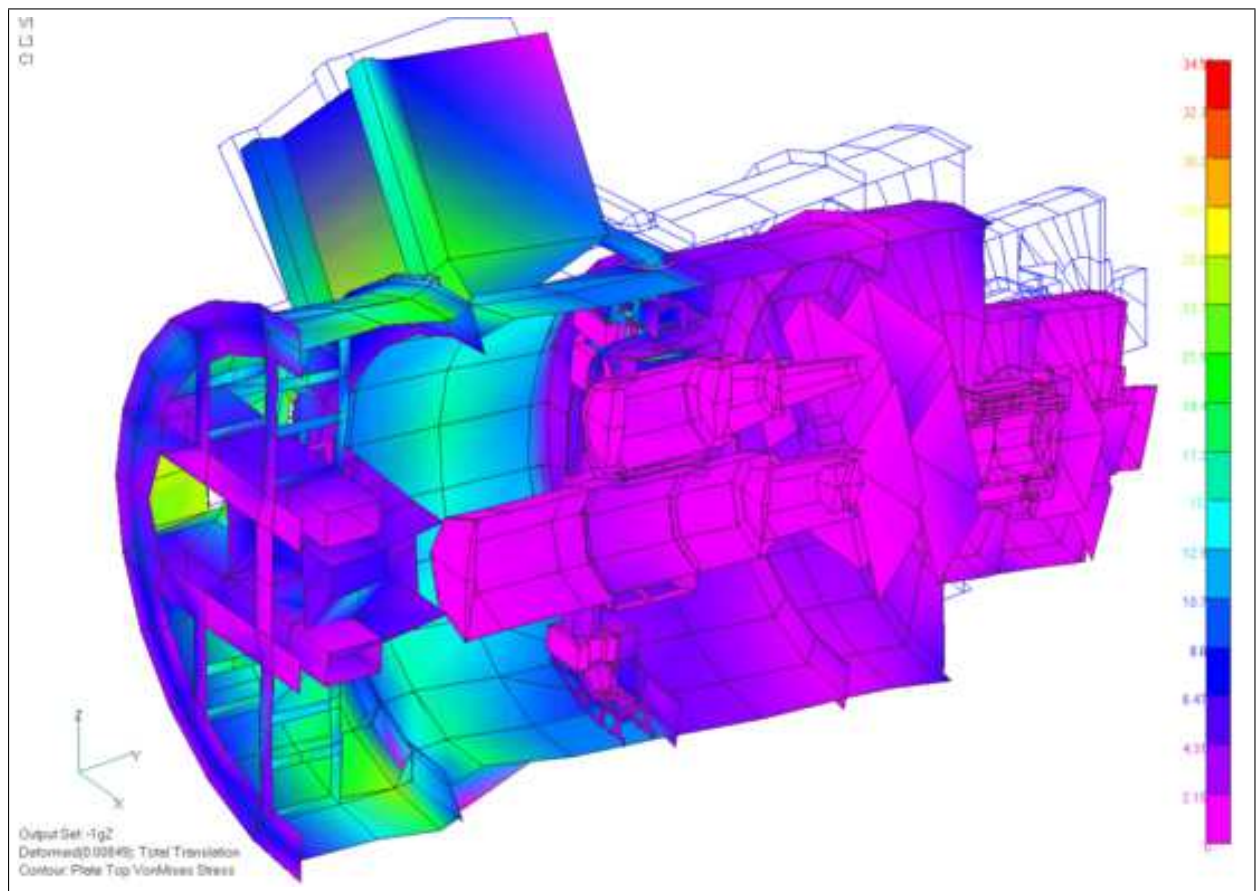

Figure 6.4: FEA model, displayed with the amount and distribution of the 'Von-Mises' material stress of the instrument housing and of the inner opto-mechanical units.

8–12 Hz. The next possible source for excitation, the AC frequency of the electrical power net, is also far away with 50 Hz. Also the response of the telescope structure on excitement through earthquakes is far below the instrument's 70–100 Hz range.

These frequency ranges altogether result in the condition that the telescope and the instrument is dynamically decoupled. This means, that the static loads only can be applied by multiplying the load factors. Those were determined to maximal $3–5g$ amplification due to earthquake response by the telescope's mirror cell. These additional loads would be easily absorbed by the instrument structure which exhibits still a reserve in yield strength of at least a factor of 4 when it is applied to the static FEA results.

The outcome of the modal analysis supported that no further dynamical analysis – for instance taking into account dynamical response spectra and excitation – became necessary in view of the largely decoupled frequency ranges.

6.2.4   Tuning the flexure compensation

Much effort was spent to identify a possibility to adjust the flexure compensation after the instrument was manufactured and assembled. The design had to open the opportunity to fine tune the compensation in the very last moment, when the instrument will be attached to the telescope. This was regarded from the designer's point of view as the fall back solution if the analyses would fail at the end due to the many unknowns or uncertainties in the real behaviour of the telescope and the instrument's reaction.

The cylinder housing turned out to react very insensitive on variations of the plate thickness. This variation could only be performed within a reasonable range that would allow the welding of the enclosing structure. Reducing the aluminium plate from 8 to 4 mm thickness for the top and from 6 to 3 mm for the collimator section did result in a change of image shift of only $0.2\,\mu$m and $0.7\,\mu$m, respectively. This became evident, when setting the cylinder diameter in relation to the thickness of the plate and its variation, because flexure compensation is based on the curvature and not on absolute displacement.

On the other hand, large effects in compensating image shift should be expected when the stiffness would suffer a discontinuity. Such a discontinuity will appear when the diameter of the cylinder housing changes abruptly. A plate, that connects two cylinders of different size together, will suffer a so-called S-sag. This will disturb the continuous progress in curvature and leads to a dramatic increase in the tilt of any subsequent structural part.

The remove of the triangular stiffening ribs from the flanges, that did connect top and collimator section, did have no effect on compensating image shift because it increased the displacement and tilt of both, collimator and camera, and maintained their relative positions to each other. But, the remove of the stiffening diagonals at the link plate, that connects the larger filter section with the smaller camera section, the tilt of the camera increased that large, that the residual in image shift changed abruptly from about $3\,\mu$m to -35 μm.

Maintaining the collimator displacement, the camera tilt became too large so that the compensating image shift did pass the target value resulting effectively in an over-compensation. Thus, any variation in the configuration, kind and thickness of the stiffening diagonals could lead in principle to an optimum in flexure compensation that would be obtained in an over-

| Model | Imaging | General | CODE V ray-trace | | Residual image shift | |
No.	mode	load	dx	dy	dx	dy
G400FS	SR	$1g_y$	–	- 2.1 μm	0.02 μm	- 2.16 μm
G418FS	SR	- $1g_y$	–	0.1 μm	- 0.02 μm	0.00 μm
G4P9FS	SR	- $1g_x$	0.5 μm	- 1.1 μm	0.48 μm	- 1.10 μm
O400FH	HR	$1g_y$	–	5.5 μm	0.06 μm	- 5.54 μm
O418FH	HR	- $1g_y$	–	2.5 μm	0.11 μm	2.40 μm
O4N9FH	HR	$1g_x$	1.5 μm	–	1.59 μm	4.01 μm
O4P9FH	HR	- $1g_x$	- 0.8 μm	4.0 μm	- 0.74 μm	3.92 μm
O4P4FH	HR	-0.7g_x,0.7g_y	- 1.1 μm	5.1 μm	- 1.00 μm	5.05 μm

Table 6.3: The residual in image shift that is left by compensating the collimator displacement with the camera tilt, as it was obtained by finite-element-analysis. The corresponding computer model of the final design is shown in Fig.6.3. The results are obtained for the two configurations, once the SR and once HR collimator in the optical beam at the position angles 0°, 90°, 180°and 270°. Given are two results, once obtained with optical ray-tracing program CODE V and the other with our own calculation formula according to Section 5.1.1. The former was done additionally which confirmed our own calculation in the very best way within tenths of a micrometer. Therefore, further ray-tracing could be abandoned and subsequent image shifts were calculated with our own formulation. That flexure compensation is designed at its optimum, display the values obviously because the direction of compensation changes its sign when going from SR to HR mode, standing for over- and under-compensation, respectively. The ray-tracing results are displayed in Fig. 6.5 were the residual X-Y motion is plotted in the detector plane.

compensation for the SR-collimator and under-compensation for the HR-collimator. This had to be balanced out, because the two collimators own different focal length and produces therefore different image shifts.

This optimum could be obtained at the final design through attaching four diagonals in a cross configuration, coincident with the two symmetry axes. Two of them had to be duplicated in order to compensate for the lack in stiffness that was obtained though cutting the service openings for the filter replacement into the plate, connecting the two sections. This opportunity in re-stiffening the filter/camera section by simple diagonal beams is of great value because it opens the option to manage the camera tilt at the very last moment. Additionally, we became able with these diagonals to react on any stiffness variation as a function of position angle. This would be done through configuring the number, the thickness and the size of the diagonals at the telescope site. Varying these parameters in the finite-element-analysis confirmed an adjustment range in compensated image shift between + 2.5 μm (over-) and - 0.5 μm (under-compensation). The residuals in image shift, that were obtained theoretically as the optimum in flexure compensation are listed in Tab. 6.3. It shows the results in image shift that were obtained for the final design, just before manufacturing and procuring the structural parts.

Figure 6.6 plots the same results as a function of altitude angle for both, SR and HR collimator. It makes obvious, that over- and under-compensation are the optimum in compensating the image shift of two collimators of different focal length.
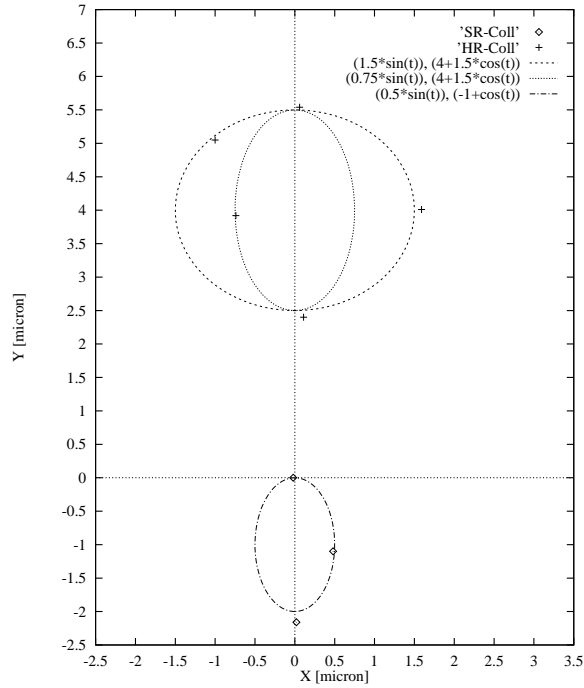
Figure 6.5: Analytical image motion in the detector focal plane according to the FEA results at the end of the FDR phase. It plots the values of Table 6.3, obtained by inserting the FEA displacements and shifts into the ray-tracing program CODE V. These elliptical tracks has to be compared with those that were obtained in the tests under real conditions, plotted throughout the next chapter. They look astonishingly similar.
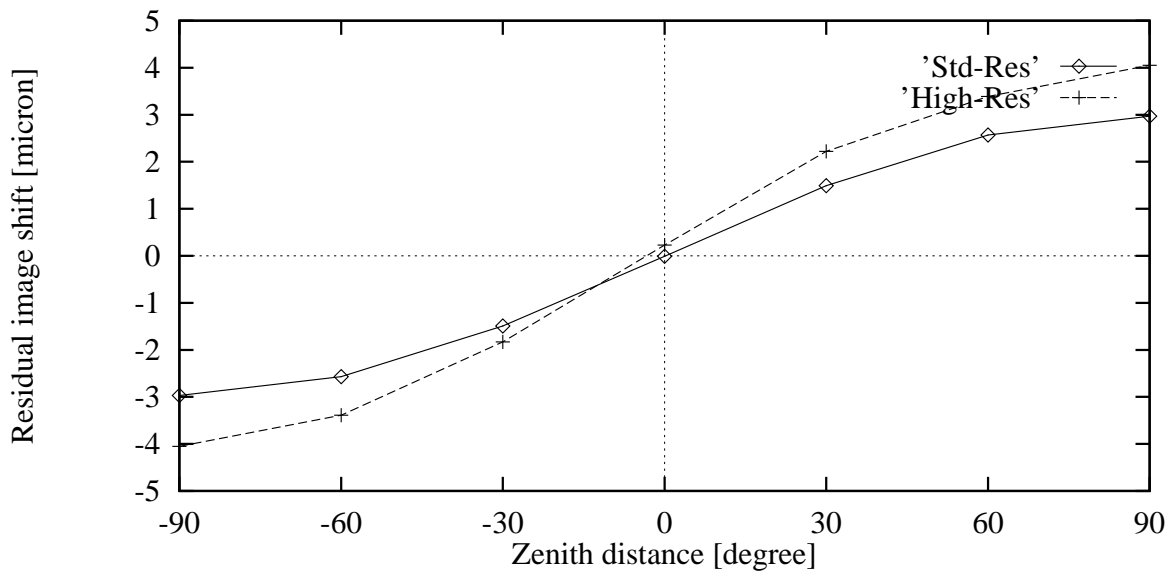

Figure 6.6: The residual in flexure compensated image shift as a function of zenith distance ZD, all obtained from finite-element-analysis at the end of the final design phase.

Chapter 7

Test results obtained at integration, simulator and telescope installation

7.1 Test results obtained at integration

Numerous tests had already be performed prior to integration during the assembly phase of the modules, sub-units and units. Those cover basically the specific functions of each part. After passing this test, the units were integrated into the main sections. Prior to the shipment of the integrated sections to the telescope simulator, each section was tested electro-mechanically on its critical functions in the assembly hall.

7.1.1 Flexure simulations in the integration hall

The flexural behaviour is from the mechanical point of view one of the most critical aspects in designing spectrographs especially when mounted to the Cassegrain focus as already mentioned in previous chapters. Therefore, one is aiming for information on the real stability in a project phase as early as possible in order to develop strategies to counteract an unexpected misbehavior. Due to special circumstances in the project, we became able to simulate the basic flexure of the instrument's top section by introducing the correct momentum into the housing parts of the instrument copy, i.e. of FORS2. The flexure of the top section is one of the most critical values since it affects the displacement of focal plane devices and collimators, the camera and dewar tilt and the stress amounts at the front flange loaded with the maximum on momentum.

The loading simulation reduces to a combination of a force with a position measurement. The instrument was fixed upside-down onto a concrete floor. Two preparatory steps are necessary in order to get the right reaction force at the front and a well distributed momentum at the back end of the top section. The first is ensured by the aid of an existing storage flange with a well fitting fixation to the concrete floor. The second is tried by bolting the two collimator housings, that of steel and of aluminium, to the top section which should distribute the forces that are induced at specific locations at the back end. A force of $1\,200\,\text{kp}$ was applied at the back end of the assembled housings in order to introduce a momentum of $19\,200\,\text{Nm}$ that acts at the front flange when the 2.1-ton instrument points to the horizon with its centre of gravity at $920\,\text{mm}$

off the flange. This force was applied in three different ways, a) by a single attachment point, b) by a symmetrical attachment at two points, c) distributing the load by wrapping a crane rope around the far side of the cylindrical housing in order to check the best arrangement for load distribution.

The two-point attachment revealed the best symmetrical behaviour between the near and the far side of the acting force. It delivered the most reliable results due to the best load distribution along the housing downwards to the measured top section. The other two attachment configurations, the single and the distributed load, both show different values at the front relative to the back side of the symmetry plane as an indication for inhomogeneities in the distribution of momentum. Hereafter in this chapter, the results of the symmetric two-point force application, the only one out of the three test-setups, will be discussed in detail.

The displacements of the top section housing were detected with micron-gauges for all $90°$ position angles at several elevations. At the $90°$ and $270°$ position, relative to the applied bending momentum, the transversal contraction of the top housing was typically $5\,\mu\mathrm{m}$ when applying the load. The measurements with a dense sampling along the symmetry plane of the top section revealed a progressive increase for the deformation between the two flanges, a clear indication for bending of the housing. The absolute displacement at the focal plane level was about $42\,\mu\mathrm{m}$ at the front and $33\,\mu\mathrm{m}$ at the back side, relative to the applying load. A thorough inspection of all measured data by two colleagues exhibit that the concrete floor deformed under load into S-sag shape, which affected all measurements by tilting the stably' mounted micron-gauges by $5\,\mathrm{arcsec}$ in the front, minus $12\,\mathrm{arcsec}$ in the centre and $3\,\mathrm{arcsec}$ in the back of the housing. The effective tilt (relative to the central reference one) corresponds to a linear increase coefficient of $1/14.3$ at the front and $1/18.4$ at the back as function of flange distance in Fig. 7.1. When applying all corrections i.e. motion of the reference storage flange and tilt of the gauges by the concrete floor effect, the above values reduces to about $10\,\mu\mathrm{m}$ which is the offset between the full load data of $12\,\mathrm{kN}$ and the linear line for increasing distances to the bending floor (Fig. 7.1). This effective value for the motion of focal plane equipment matches fairly well the $6\text{--}10\,\mu\mathrm{m}$, that are estimated twice, once within finite-elements, modelling the simulating situation, and also from our standard computer model of the instrument.

All data which are taken at different load levels up to the simulation limit of $1\,200\,\mathrm{kp}$ show very precise linear scaling. This was a clear indication that we observed a pure bending according to Hooke's law with the lack of friction at the bolted flanges. A forced relaxation had to be applied to the mechanical system under test to overcome hysteresis effects. This was performed in a way as it was done numerous times for precision measurements by a gentle knocking on the housing. Additionally, the sag of the concrete floor had to be taken into account to reach the accuracy in linearity and reproducibility of the measurements that was observed. This simulation plays an essential role to determine the real motion of slits and masks within the focal plane of the telescope which was measured at the telescope simulator and is described in a later section.

7.2   Functions of the telescope and star simulators

One forcing requirement from ESO is the handover of the instruments in Europe in a well and fully tested manner before they will be shipped to the remote site of Cerro Paranal in Chile. The experience that is gained with the instrument at the simulator within a period of a year
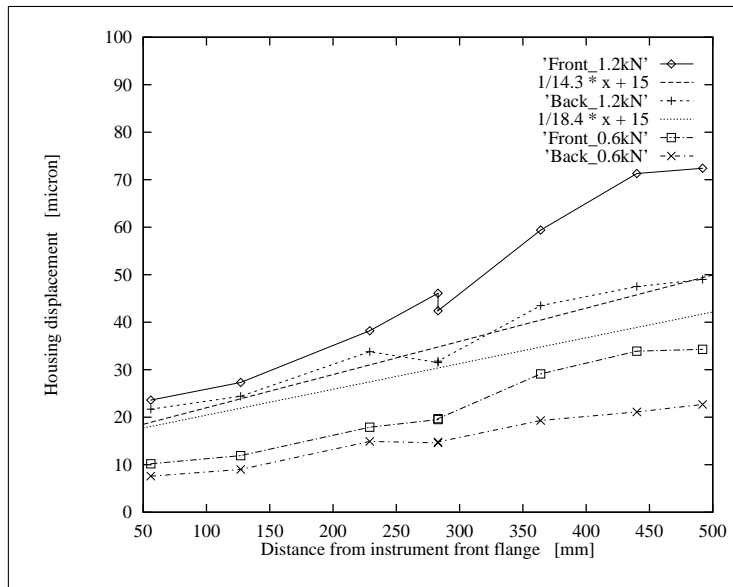
Figure 7.1: Displacements of the top section housing obtained in a bending simulation. The measured curves show the displacements for the nominal 12 000 N load at the front and the back side of the symmetry plane as well as for half this load for checking the linear scaling. The floor effect is indicated by the linear increase of 1/14.3 for the front and 1/18.4 for the back side.

fully supports that demand. Lots of necessary modifications of the instrument and the software interaction could otherwise not be performed.

Several simulators, specially dedicated to the FORS instruments, were built by the VIC consortium. The largest one was the telescope simulator that was motor driven in two axes, in the elevation and the flange rotation axis. These two-axes motion did simulate any motion of instrument within the gravitational field with all possible aspect angles relative to the gravitational vector.

This telescope simulator did allow the checking of

- all electro-mechanical functions and its performances regarding fine-tuning adjustments, reproduction accuracy and reliability,

- all opto-mechanical adjustments, sensitivities and stabilities,

- the optical qualities in imaging mode, spectroscopy and polarimetry under real i.e. bending conditions etc.,

- the interaction between software and electronic hardware in a realistic environment,

- the contamination of the detector and its controller system by homemade electro-magnetic noise from the instrument itself,

- the behaviour of the cable wrap with all its power and cooling lines and the fibre link for data transmission

under realistic and fully operational conditions.

59

Additionally to this telescope simulator, two star simulators were build to provide adequate light sources for all these tests. One formed star images via projection optics while simulating the telescope optics as close as possible except for its astigmatism – which is inherent to the RC-system – and the small residual of mismatching coma. It provided stellar images with the right size and F-number that could be positioned at every location within the instrument's field of view allowing the analysis of image qualities and ghost images and to determine the amount of straylight. The second star simulator was specially build for testing purposes of the instrumental flexure. This was designed to illuminate pinholes in the instrument's focal plane without introducing errors in image shifts by its own bending through a stiff mounting.

These three simulators could cover in their combination the telescope functions almost completely except for the environmental effects. The consortium was not able to simulate thermal loads or behaviour of the instrument or of the internal modules by changing temperatures or gradients of the range to be anticipated at the Paranal Observatory. These tests were considered to be dispensable because detrimental effects were not expected according to the proper design and the results of corresponding thermal calculations.

Another effect that could not be simulated realistically is the electro-magnetic environment of the observatory to test the electromagnetic compatibility (EMC). Due to this lack we are unable to test the irradiation of electro-magnetic noise. That would – if any – most probably affect the instrument but not the telescope or the dome functions due to the power consumption of the instrument, the telescope and the dome driving motors, respectively. A contamination of the near-field environment by electro-magnetic noise, produced by the most powerful drives of the instrument for filter and collimator exchange, could be detected. It did not impair any electro-mechanical function but it affected the detector and its controller system. An improved shielding could not counteract the induction of noise into the data lines but the right change of the motor frequency shifted the noise into a domain that was uncritical for the detector system. Even though the EMC problem could be solved for the instrument alone, no simulation strategy could be found so far for the observatory's environment. Thus, the compensation for a possible electro-magnetic incompatibility had to be figured out for the telescope site.

The last lack in simulating the observatory's environment were the loads that will be induced by possible earthquakes, emergency brakes or wind buffeting. The probability for an earthquake is in this seismic very active region of the pacific plate extremely high, compared to Europe. I was not surprising that since the beginning of constructing the observatory, several weak and one strong earthquake took place. Up to now, the strongest quake happened in 1995 on July 30. with an intensity of grade eight on the Richter scale which produced some minor damages to the equipment like the domes etc. that were already installed on the mountain at that time. Acceleration curves exist for the telescope site which are transformed by finite-element calculations to specific locations like basement, control room or the different foci. The ground acceleration for the Unit Telescope was given with $0.34\,g$ or 8.5 magnitudes to the maximum which is magnified by the telescope structure (yoke, tube and mirror cell) to amounts of about $3\,g$ with a maximum just below $5\,g$. The instrument structure withstands these loads according to our finite-element analysis. The FE-models clearly indicate that additional loads are allowed to amount to a factor of 20 at least. This will be by far enough reserve in strength for the loads expected for earthquakes, deceleration of any emergency brake or the wind buffeting. They all are only a small fraction of the load that would be induced by an Operational Based Earthquake 'OBE' or the even stronger Maximum Likely Earthquake 'MLE'. Due to the experience that the consortium unfortunately gained with the instruments in the course of testing, and which

strongly supports the analysis, no doubt exists that the instrument will withstand all these loads.

7.3 Flexure tests on bending characteristics in imaging mode

Determining the bending characteristics of the instrument and its opto- mechanical components was one of the main issues of the entire testing programme. Therefore, several weeks were spend in total on determining the instrumental behaviour regarding flexural stiffness and the influence of the bending effects affecting primarily the optical, secondary the electro- mechanical functions. In the following, the characteristics of instrumental flexure in the imaging mode is described as well as the fine-tuning range and its optimisation with respect to image wandering on the detector. The behaviour regarding spectroscopy and electro-mechanical functions will be presented in a following section.

7.3.1 The principle flexural behaviour

The affecting flexure of a spectrograph can be modelled completely if the stiffness of two axial sections of 90° separation is known. In case of equal stiffness in these two transversal planes, the displacements measured for those planes should be of symmetrical amplitude relative to the null reference at zenith position. The stiffness of the instrument at any position angles in-between the two principle planes can be modelled by co-adding the sine and cosine component of the stiffness in this two planes. A symmetrical structure resulting in an equal stiffness in the principle planes should therefore form a perfect circle of displacement measurements when rotating the instrument around with its optical axis pointing to the horizon. If the stiffness in both planes is unequal, an elliptical distribution of the displacements should turn out. The stiffness of each of the two principle planes can be regarded as the major and the minor semi-axis of an ellipse. The effective stiffness and the resulting displacement at each arbitrary position angle can be calculated from the vector components of the elliptical equation. In case of the FORS spectrograph, it was clear right from the beginning that the two principle planes coincide with the main sections through the instrument i.e. the X- and Y-plane due to the axial-symmetry of the inner structure.

All measurements of flexural stiffness base on the concept of flexure compensation, outlined in chapter 5.1.1. Therefore, not the displacement of each single opto-mechanical component is taken into account but the motion of the base optics itself that images point sources onto the CCD. The image motion is the residual optical effect of displacing and tilting the base optics in superposition. An independent measurement of each single base optics could not be performed with reasonable means because there is a close interaction between bending of the collimator and tilt of the camera through the feedback of the collimator section onto the camera section's tilt when loaded by the subsequent camera section for detection. A consequence of this interaction is that the spectrograph is tested in the most realistic way by its own components though using the instrumental optics simultaneously as measuring as well as loading tool. This dependance led to the principle of detecting only the superposed optical compensation effects. It is therefore impossible to derive the single contribution of each component from these measurements and the amount of collimator translation, camera tilt and CCD displacement remains unknown in absolute terms.

The test plan hereafter was derived from these constraints. So the image motion was measured at first for each of the two principle stiffness planes as a function of the elevation angle. A check followed if the image is wandering on a circular or on an elliptical track when the instrument rotates under maximum deflection with a horizontal pointing. The first measured image motion track followed an elliptical track (Fig. 7.2 and 7.3). But also hysteresis effects were detected at this most extreme attitude. It became clear in subsequent tests that slews in elevation solely could not explain totally the stiffness amplitudes of the two principle planes. It turned out that the measurements depend on the pointing prior to the measurement and on the tracking path to reach each test position. Due to this hysteresis effect, the original testing plan had to be modified.

The general test procedure for each individual setup of stiffening diagonals did foresee first two full turns, one 360° clockwise rotation followed by a backward rotation. But at each beginning of the full turn, a turn-over of 90° in position angle was made in order to get a well defined state of the system by pre-loading the linear bearings and mounts of the opto-mechanics. Then the simulator was stopped at each 45° turn and a short exposure was taken with either an external or internal pinhole. The exact position of the centre of the pinhole's point spread function is taken with the centre-gauss command of the MIDAS image processing system. This procedure revealed an internal accuracy of about 0.02 pixel. The rotation curves were normally taken at the horizon of observation which is specified to a maximum zenith distance of 60°. Each rotation sequence starts at zenith position with a slew to the corresponding zenith distance (e.g. 60°) and also ends there for referencing purposes. The rotation curve which is obtained this way exhibits the extreme in image motion that has to be expected for the configured setup and for the corresponding attitude of observation, covering also the hysteresis effects.

For some special configurations of stiffening diagonals, a slew in attitude for both planes of the main sections was performed additionally in order to check if the flexion follows Hooke's law. The amplitudes of the resulting image motion would scale with the sine component of the gravitational vector at each attitude in this case. Additional rotation curves were also taken in some cases at zenith distances of 30° or 80°. The files that contain the original data set are displayed in each plot. The filename codes at its first position the sequential number of the test run starting with 'q..' for historical reasons, at the second position the number of stiffening diagonals (00, 06, 10 or 18), at centre the imaging mode corresponding to standard-(SR) or high-resolution (HR) collimator in the light beam and at last the instrument's attitude in degrees, at which zenith distance it is rotated (r..) or at which position angle it is slewed (s...) in special cases. The character 'm' is appended when the original data are modified and shifted by a certain constant in order to plot the rotation curves of both collimators in the same frame for comparison purposes.

The first test run was performed with a start setup of 6 diagonals attached at the filter/camera section. This configuration turned out in previous finite-element analyses as the optimum in flexure compensation. The measurements of that configuration with an external pinhole seemed very promising for both, the standard (Fig. 7.2) and the high resolution mode (Fig. 7.3. The radii of image motion of 'q06' are Sx=0.5 px, Sy=0.7 px for the SR- and Hx=0.25 px, Hy=0.25 px for the HR-collimator at the 60° horizon. Follow-up measurements were done with an external pinhole for the maximum stiffening configuration of 18 diagonals attached (q18), for medium stiffness with 10 diagonals (q10) and with stiffening diagonals totally removed (q00) (cf Fig. 7.2 and 7.3). These few measurements already show that the relation between the radius of image motion and the number of diagonals is linear as one would expect from the linearity of Hook's law
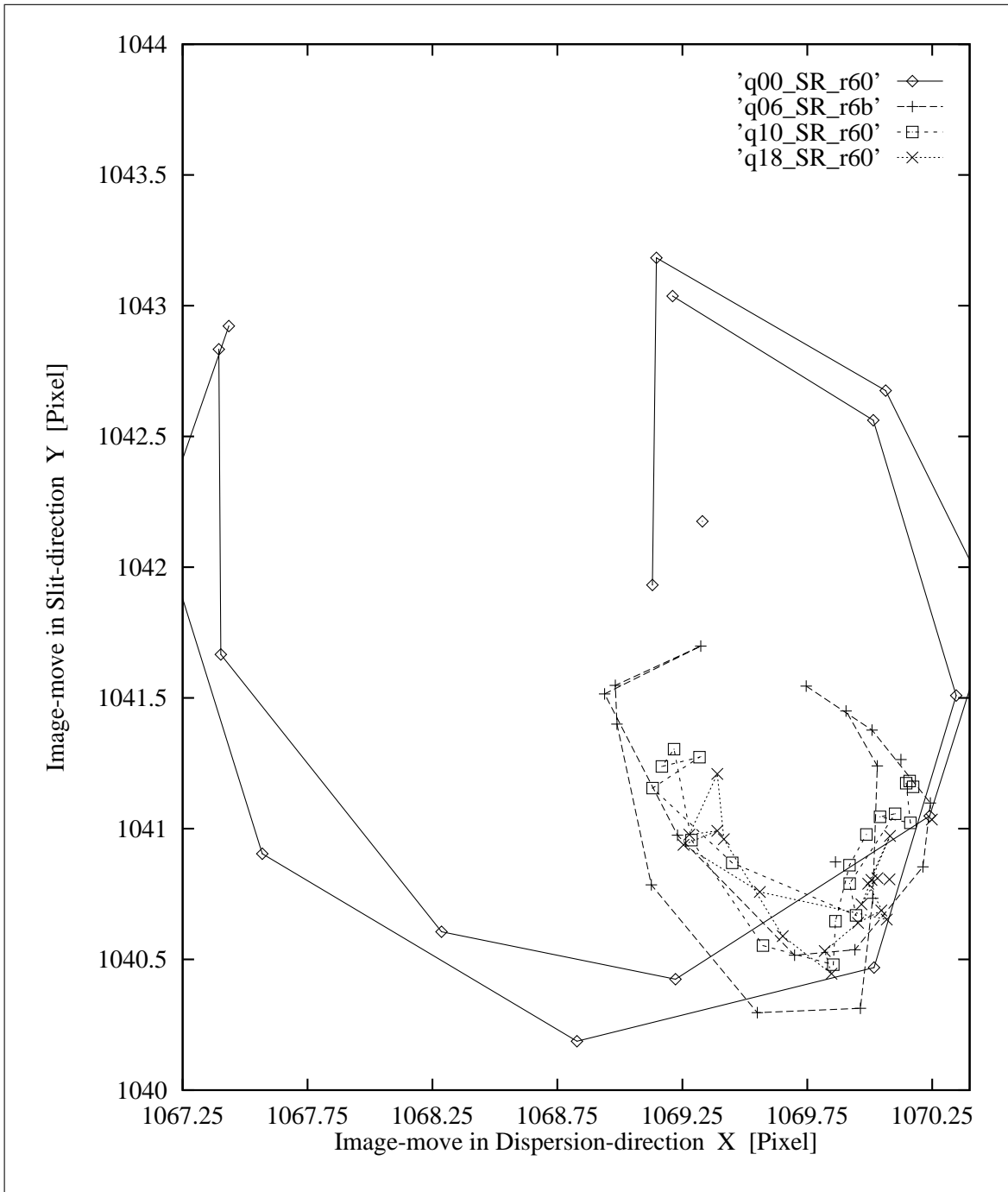
Figure 7.2: Image motion track of an *external* pinhole in standard resolution SR-mode on the CCD taken at the very first test run 'Q'. All curves are obtained at a zenith distance of 60°. The scaling with the number of stiffening diagonals (00, 06, 10 and 18) is obvious. Circular track that closes at the top indicates 'over-compensation'.
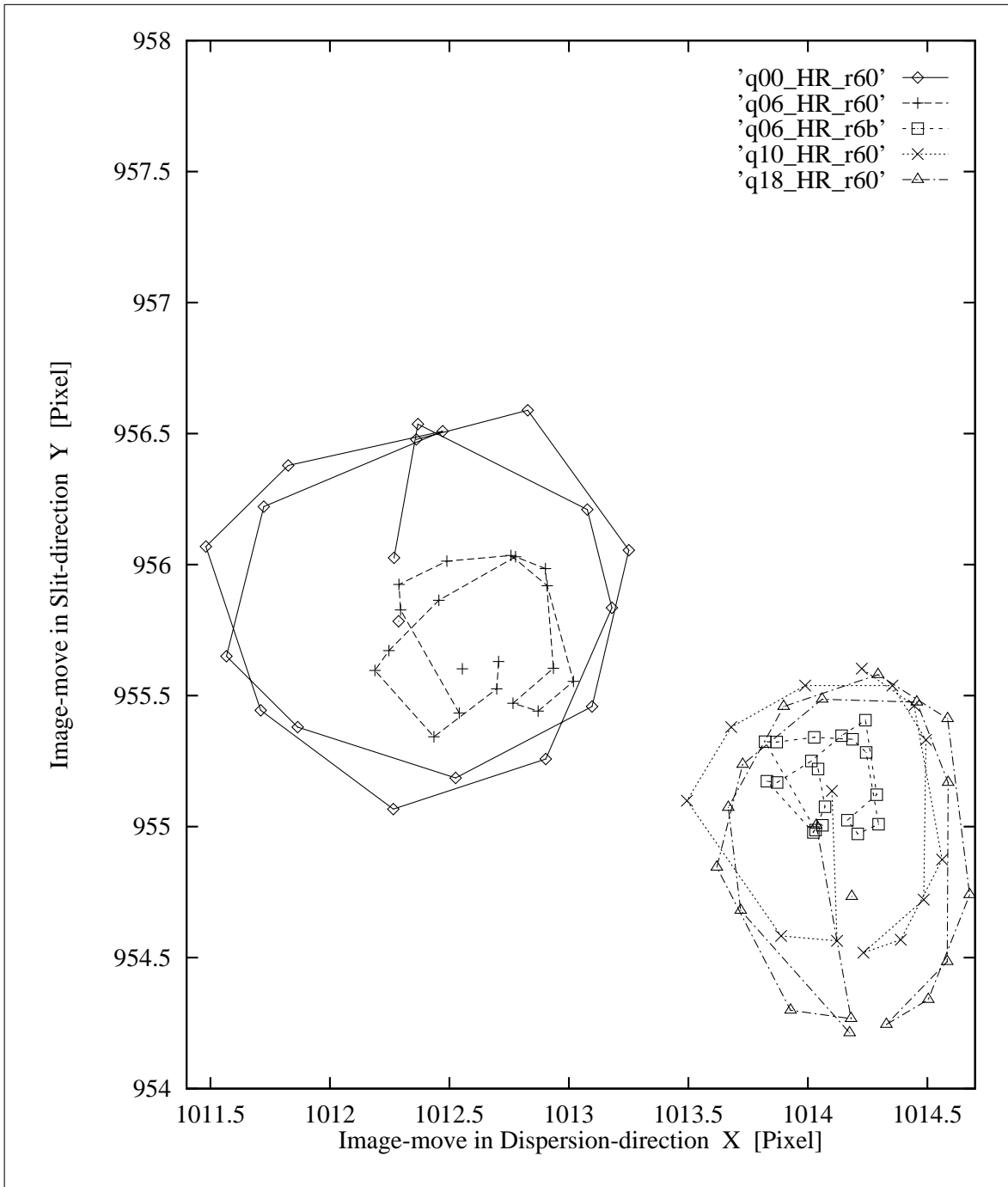
Figure 7.3: Image motion track of an *external* pinhole in high resolution HR-mode on the CCD taken at the first test, the Q-run. The rotation curves at 60° zenith distance scale with the number of stiffening diagonals (00...18). Circular track that closes at the bottom indicates 'under-compensation'.

for tension and bending. This linearity breaks down marking a turn-off point when all stiffening diagonals are removed from the filter/camera section. In this moment, the tensional stiffening of the diagonals is replaced by the bending stiffness of the intermediate plate connecting the filter with the camera section which causes a rapid increase in the camera tilt leading to the discontinuity in linear stiffness (Fig. 7.4).
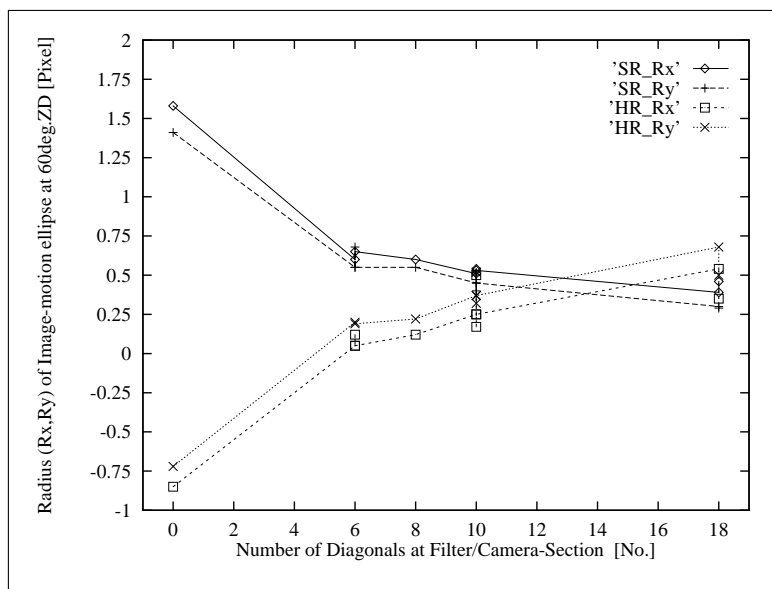
Figure 7.4: The major and the minor half-axis of the image motion elliptical track as a function of the number of stiffening diagonals, that are taken at the first test run 'Q'. The spread in radii is about 1.5 pixel for both, standard (SR) and high (HR) resolution mode. The relation is quite linearly until the turn-off point is reached when all diagonals are removed and the tension of the stiffening diagonals breaks down and is being replaced by bending stiffness.

Other effects also become obvious from the rotation curves. First, the elliptical tracks of image wandering are more or less closed either at the top or at the bottom of the curve. A closing at the top corresponds in our coordinate system to a negative sign in compensation which can be understood as an *over*-compensation of the collimator's translation by the tilt of the subsequent camera. This is usually the case for the standard collimator who causes a small image shift with its long focal length. The opposite is valid for the high resolution collimator with its short focal length. The larger image shift of the latter could not be fully compensated by the camera tilt which is constant for both collimators. This led to an *under*-compensation in the effective image shift on the detector leading to a positive residual in image shift. This becomes visible in closing the elliptical track at 6 o'clock since the tracking path from zenith position to the first horizontal pointing was identical for both collimators. Only one curve differs from that basic behaviour. The rotation curve 'q00-HR-r60' in Fig. 7.3 closes not at the 6 o'clock as the other HR-curves show. This means that the usual under-compensation of the HR-mode switched over into an over-compensation since all diagonals were removed and the tilt of the camera enlarged that much that it becomes able to fully compensate the larger image shift of the HR collimator. This switch-over was expected from finite-element calculations so that this behaviour confirms well our FEA that will be used further to describe the principle flexural stiffness.

Another effect visible in the curves is some kind of hysteresis which can be clearly identified through a 15° turn between the clockwise and the anti-clockwise rotation curve causing the

non-coincidence of image positions at identical attitude and position angle of the instrument. We have no clear detection where this hysteresis comes from although attempts were made. The latter did not provide confident results due to the small size of the deformations on micron-level which had to be detected for single components. But from our experience that we gained with the linear bearings, we have clear indications that the biggest part of the hysteresis is caused by the linear motion guides of the collimator exchange mechanism. They are already chosen at the limit of available size of 100 mm to carry the heavy load of two collimators including their mounting box. The pre-load of the 6 mm balls within the bearing was also set to the manufacturer's limit in order to make the guide as stiff as possible. But stick-slip effects on micron-scale cannot be fully excluded as the reality reveals. This assumption was confirmed later when measurements were taken from individual slitlets of the MOS which exhibit identical behaviour (Fig. 7.15). Although this hysteresis effect was detected, the consortium did not expect detrimental effects because astronomical observations always run very smooth and tracking follows continuous rotations without any abrupt changes in pointing. Therefore, the observer can accept it taking into account the size of the effect on a sub-pixel size. At the end, specification on image motion was met nevertheless.

7.3.2 Modifications and variation range

In subsequent test runs, the scaling of image motion as a function of the number of stiffening diagonals and zenith distance were investigated more thoroughly. One of the principle diagonal configurations, that appeared close to the optimum for both imaging modes of the external pinhole, did cover 10 stiffening diagonals. Additionally to that detail investigations, the maximum range of manipulation of the stiffness was estimated.

From the point of view of imaging with high spatial resolution, a stiffening setup with 6 diagonals turned out optimal as clearly seen in Figure 7.6. Then, an imaged point source rests over 24 hours within 0.4 pixel for any zenith distance smaller than 60° (r06..). Introducing any additional stiffening (to a maximum of up to 18 diagonals) results in wider spread of image motion track due to an increased under-compensation in HR-mode by the gained stiffness, as it can be clearly identified in Figure 7.6 and 7.8 with increasing number of diagonals (r10...–s18...). The opposite is valid for the standard resolution mode. Gaining more stiffness by adding more diagonals reduces the amount of camera tilt matching better the smaller amount of image shift in SR-mode. This improved compensation in SR-mode can be seen in Figure 7.5 and 7.7 where the radial spread in image motion reduces from 0.7 pixel (r06..) to about 0.4 pixel (r18..). From the inverse relation in compensating the SR- and the HR-mode on re-stiffening, an optimum of 10 diagonals was estimated for the imaged external pinhole. In this case, the spread in image motion track of both modes is of almost equal size and the number of 10 allows an equally distributed arrangement of diagonals at the mounts of the filter/camera section.

Comparing both figures, 7.5 and 7.7, rotation in HR-mode forms a more circular track than in the SR-mode. The latter shows a distorted ellipse which is characteristic for all rotations in the SR-mode. The reasons for this discrepancy between HR- and SR-mode is simply the 1.5 times larger weight of the SR collimator (49 kg) that produces a much higher momentum load onto the ball bearings of the linear motion guides, the mounting consoles and the housing when placing the SR collimator into the light path with all the internal friction effects. One must emphasize that the relative shifts between the rotation tracks of Figure 7.5, 7.7, 7.5 and 7.7 are smaller than 1 pixel. The shift of the track's centre from one diagonal setup to the other shows the
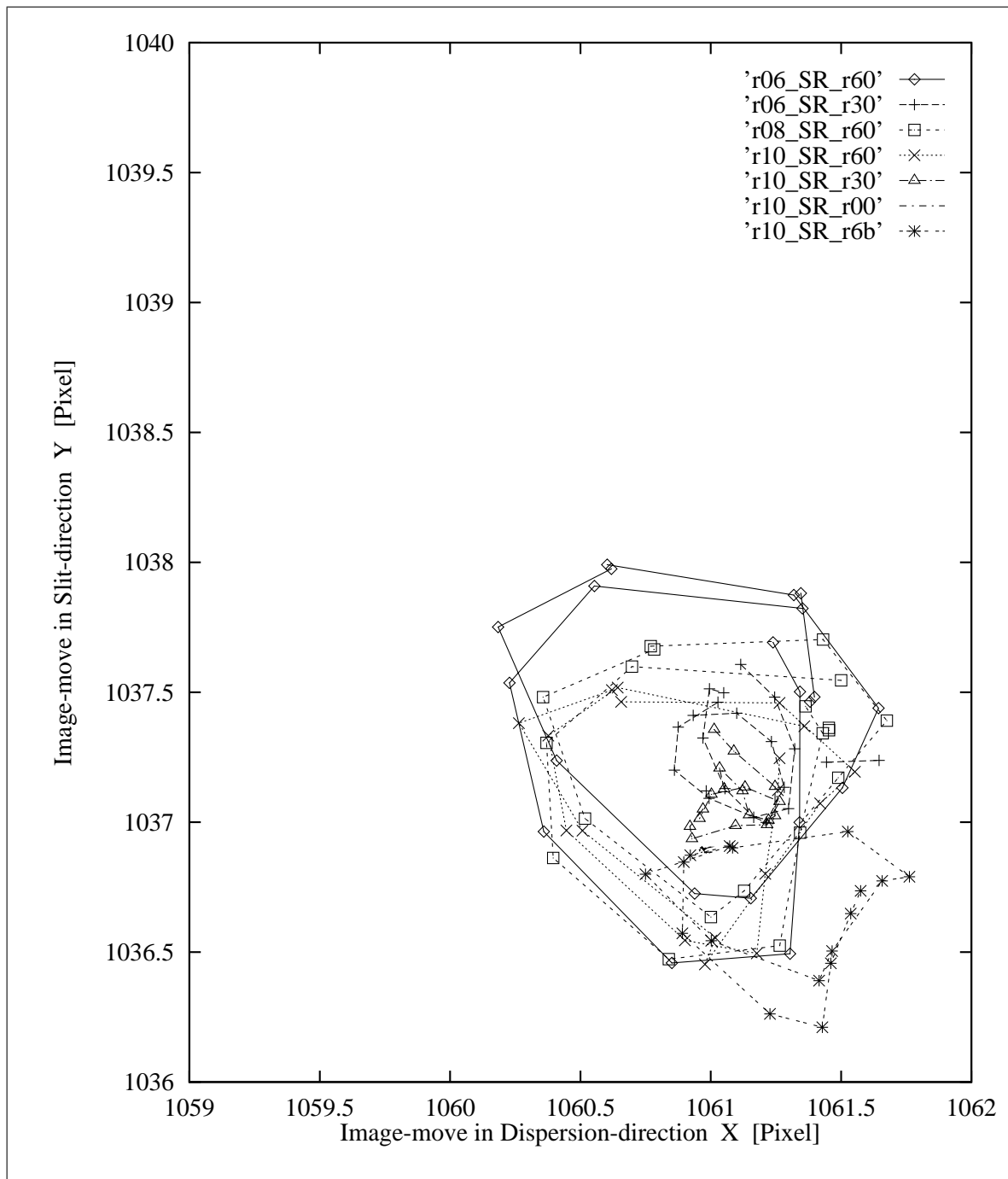
Figure 7.5: Image motion track of an *external* pinhole in standard resolution SR-mode on the CCD taken in the second test run 'R'. The improved compensation by gaining stiffness can be identified through ever smaller radii when going from six (r06...) to ten (r10...) diagonals. The last number of the filename denotes the zenith distance from 0 to 60°.
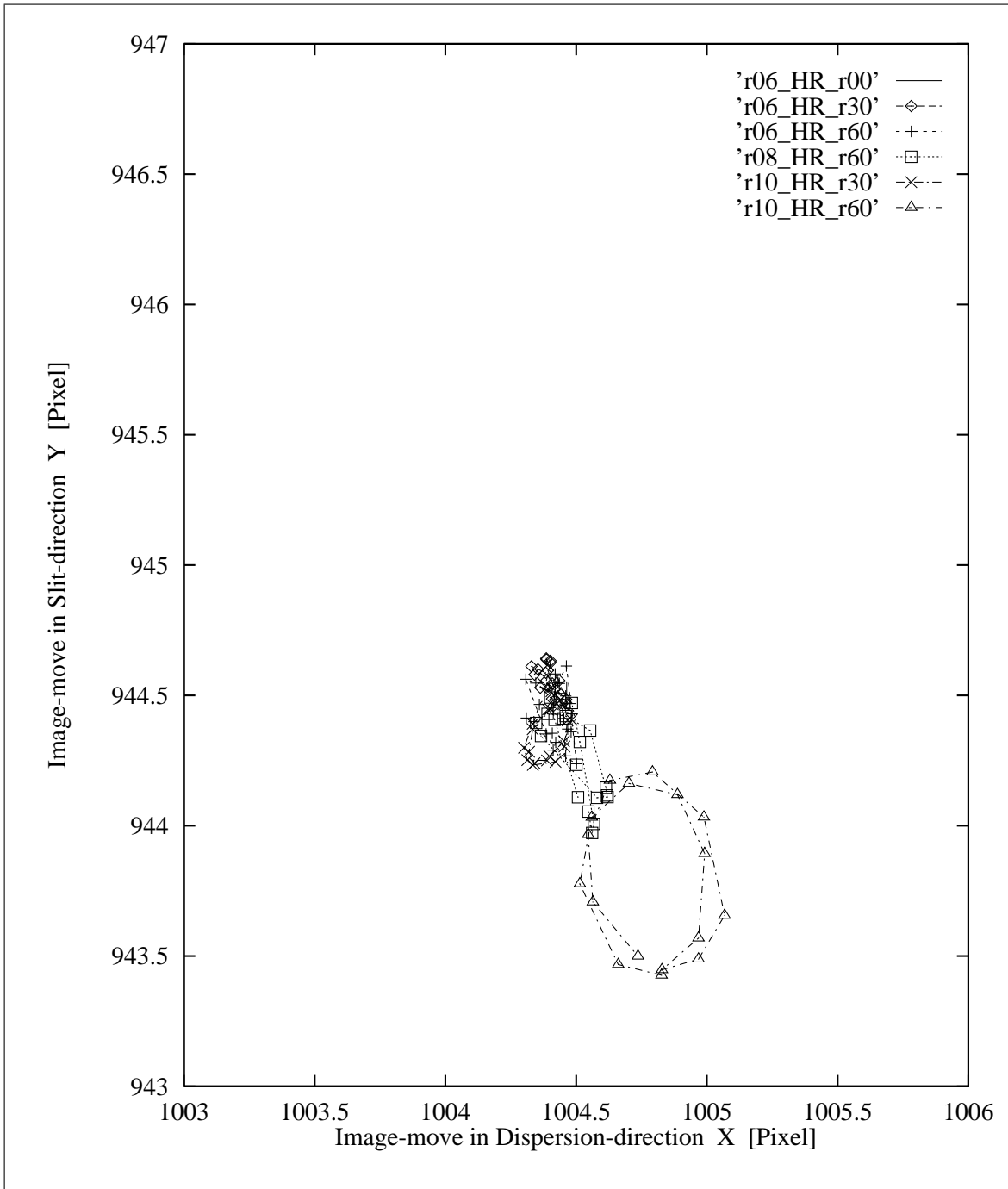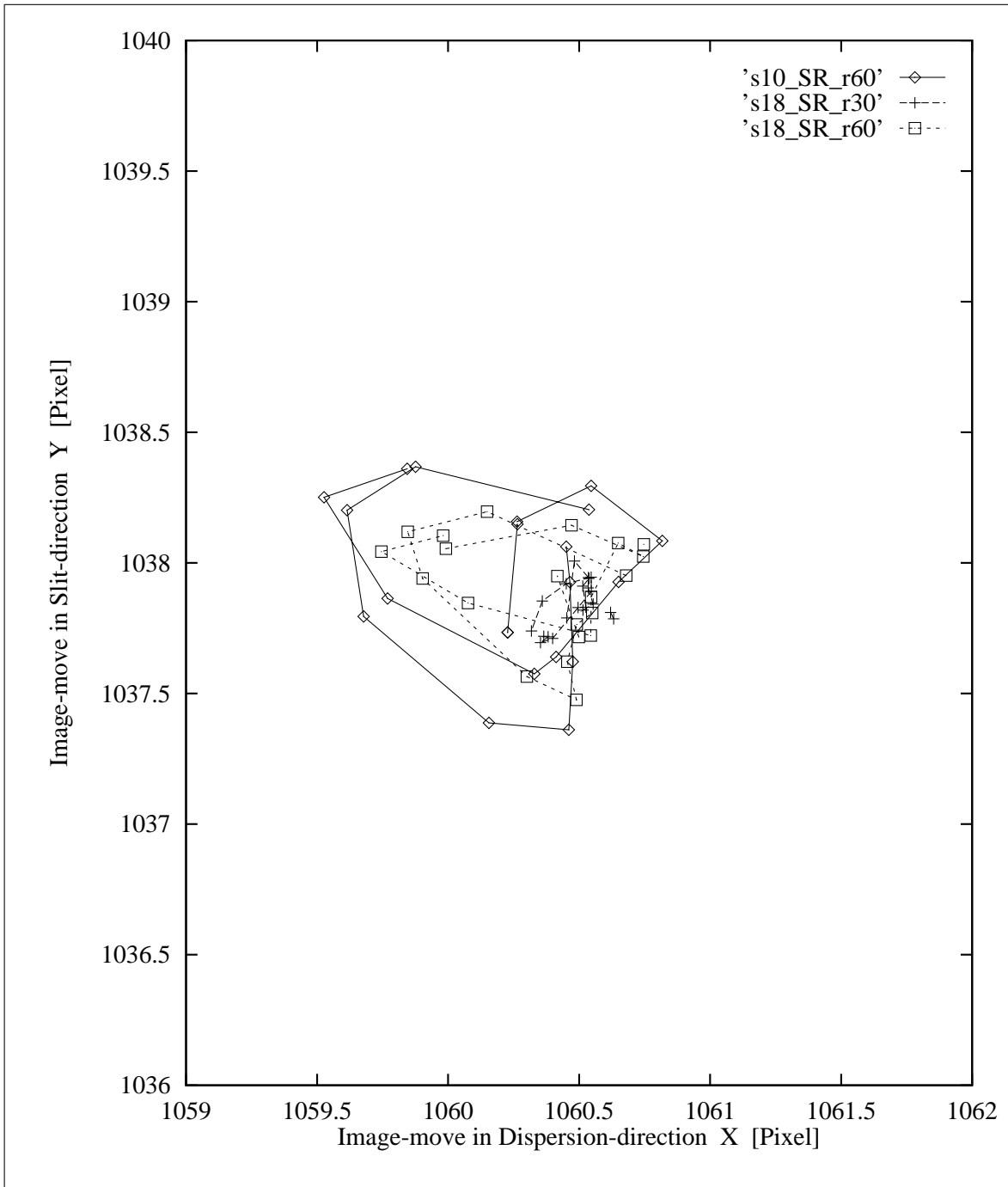
Figure 7.6: Image motion track of an *external* pinhole in high resolution HR-mode on the CCD taken in the second test run 'R'. The less matching compensation by an increased overcompensation through higher stiffness can be identified through ever larger radii when going from six (r06...) to ten (r10...) diagonals. The last number of the filename denotes the zenith distance from 0 to 60°.

Figure 7.7: Image motion track of an *external* pinhole in standard resolution SR-mode on the CCD taken in the third test run 'S'. The even more improved compensation by gaining additional stiffness can be seen in the smallest circular track of the maximum 18 diagonals (s18_SR_r60) at the maximum zenith distance that was specified for observation to 60°.
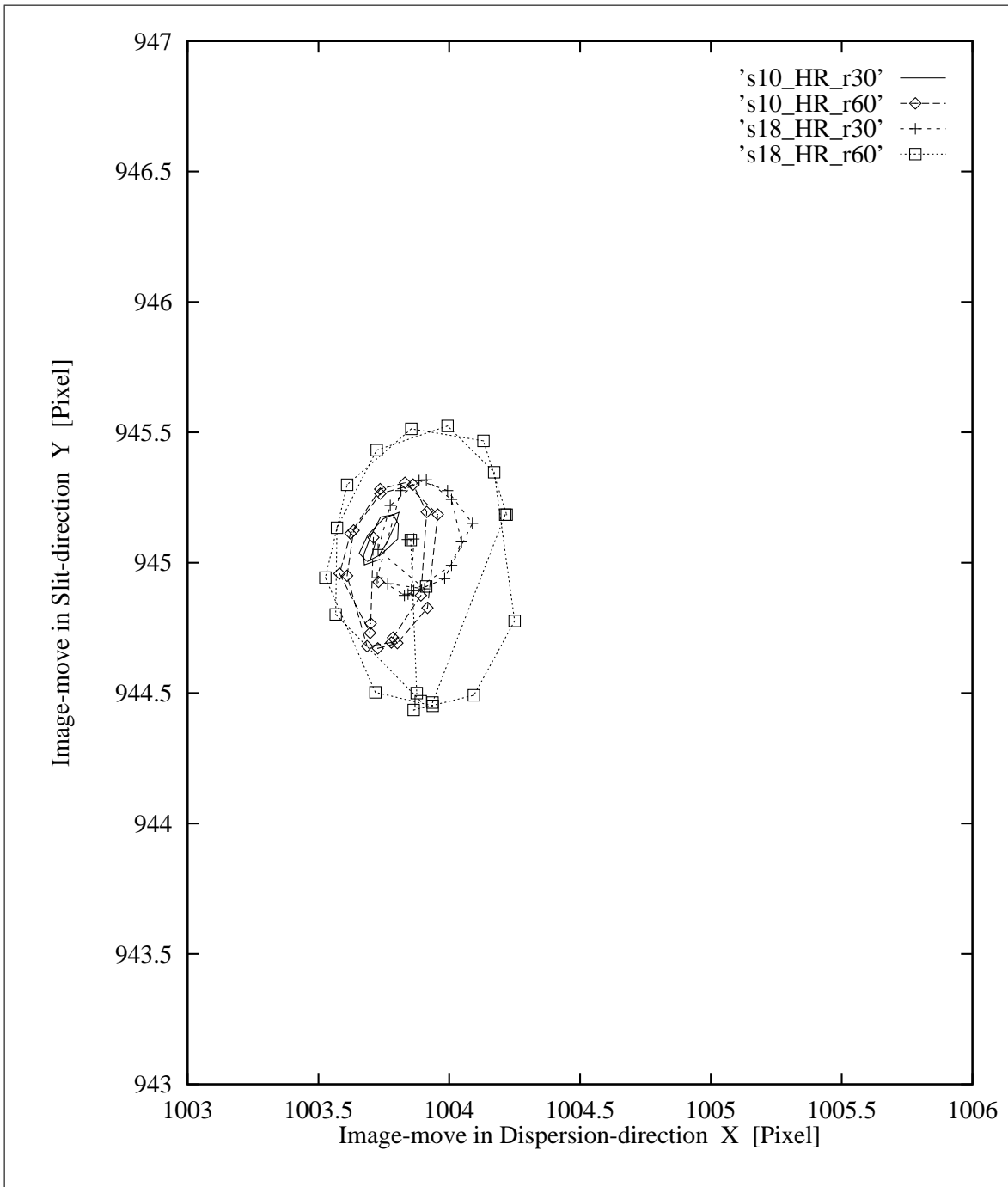
Figure 7.8: Image motion track of an *external* pinhole in high resolution HR-mode on the CCD taken in the third test run 'S'. The compensation is getting worse for even higher stiffness at the maximum available stiffness of 18 diagonals (s18_HR_r60) at the maximum zenith distance of 60°.

accuracy in reproducing the position of each collimator within the beam because the SR and HR collimator were switched back and forth in each single run. The reproduction accuracy of each collimator at the end stops is better than 0.7 pixel corresponding roughly to 70 μm for the SR and 35 μm for the HR collimator. This amount of less than one tenths of a millimetre is smaller than expected when considering the size and weight of these components. The other shifts of rotation tracks between different runs and setups are caused by a complete de- and re-attachment of the filter/camera section or the CCD dewar as well as upside-down turnings, re-attachment of the entire spectrograph at the flange and other maintenance work between the runs. The latter class of shifts are of the order of a single pixel. From all these tests follow a re-centring accuracy of the opto-mechanics of better than 0.1 mm even after maintenance work on the instrument.

Another value that can be obtained from the four plots is the scaling with zenith distance. In case of pure flexion, the radius of image wandering taken at 30° zenith distance should by a factor of 1.73$=\frac{sin(60)}{sin(30)}$ be smaller than the radius taken at 60° according to Hooke's law. This is obviously not the case, neither in SR- nor in HR-mode. The observed scaling factors between 30° and 60° amount to 2.4-3.1 which causes a progressive decrease when pointing closer to the zenith. This discrepancy to Hooke's law is most probably caused by non-linear forces like friction and stick-slip effects. Those can occur at the intermediate flanges connecting the housing segments, at the bolting screws and at the ball bearings of the linear motion guides. The latter are used for both optics defining the flexure compensation, the collimator exchange as well as the camera focusing unit. Observing this effect is not surprising for an instrument that bears a complexity that high as this spectrograph does.

In a fourth run (Fig. 7.9, 7.10), image motion was checked with an image of an internal pinhole that was realized with the spectrograph's longslit mask. The radius of image motion track, taken with the optimum setup of 10 diagonals for external pinholes, amounts to Sx=0.9 px, Sy=0.9 px in the SR- and Hx=0.6 px, Hy=0.8 px in HR-mode. This is difference of some 0.4 px in the SR-mode which has to be caused by additional motion when changing from an external to an internal pinhole. This excess is obviously the motion of the instrument's focal plane holding the longslit mask with the internal pinhole. The 0.4 px excess in SR-mode translates to an 0.04 mm motion in the focal plane whereas the 0.4 px of the HR-mode transforms into 0.02 mm focal plane motion. At the first glance, this appears contradictory but a close inspection of the HR rotation track (Fig. 7.10) exhibits that the elliptical track closes at the top. This means that the former under-compensation switched into an over-compensation, like the SR-mode. Taking this change into account, the excess in HR-mode amounts correctly to 0.8 px or 0.04 mm in the focal plane which is fully consistent with the standard resolution mode. A much more detailed investigation of this turned out that this focal plane motion is not caused by a flexion of the instrument itself, but by a flexure of the telescope simulator's flange which will be addressed later. Measuring the image motion tracks, caused by instrumental flexure alone, is better performed with an internal than with an external pinhole due to this bending effect of the telescope simulator.

Therefore, a sample of rotation tracks (Fig. 7.11, 7.12) were taken with the internal pinhole in the longslit mask for both imaging modes as a function of diagonal setups and zenith distance to obtain the flexure residual of the instrument alone. It turned out that the instrumental flexure itself will be compensated at best at the maximum stiffness of the filter/camera section, obtained with 18 diagonals. The radii at the 60° ZD were estimated to Sx=0.8 px, Sy=0.7 px, Hx=0.3 px, Hy=0.4 px in SR- and HR-mode, respectively. The scaling according to attitude as well as stiffness variation can also be obtained from these plots. Although the resolution
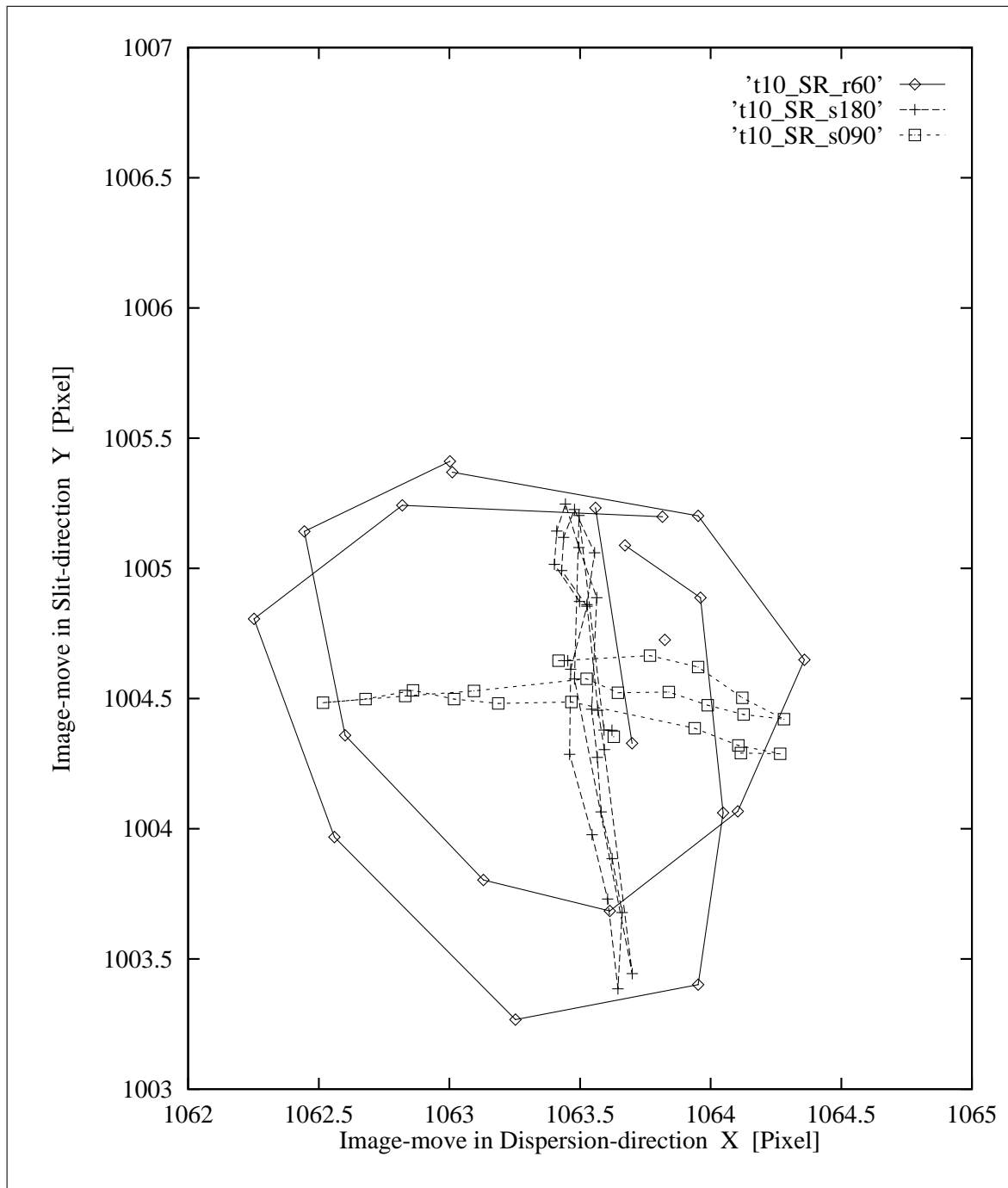
Figure 7.9: Image motion track of an *internal* pinhole in standard resolution SR-mode on the CCD taken in the fourth test run 'T'. It shows the for- and backward rotation track for the 10 diagonal setup. The elevation slew (...s180) and (...s090) in the two principle planes of symmetry is overlaid.
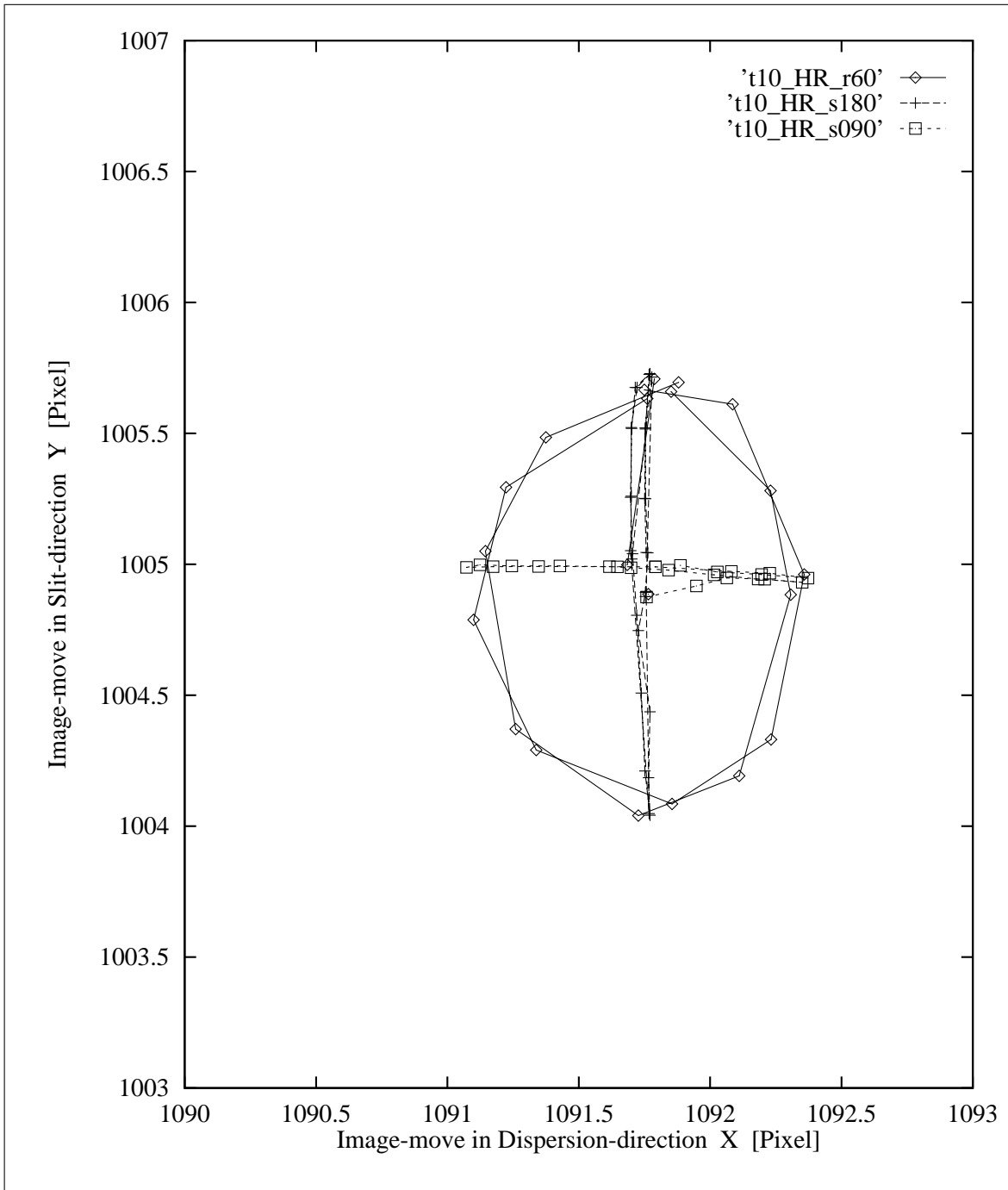
Figure 7.10: Image motion track of an *internal* pinhole in standard resolution HR-mode on the CCD taken in the fourth test run 'T'. It shows the for- and backward rotation track for the 10 diagonal setup. The elevation slew (...s180) and (...s090) in the two principle planes of symmetry is overlaid.
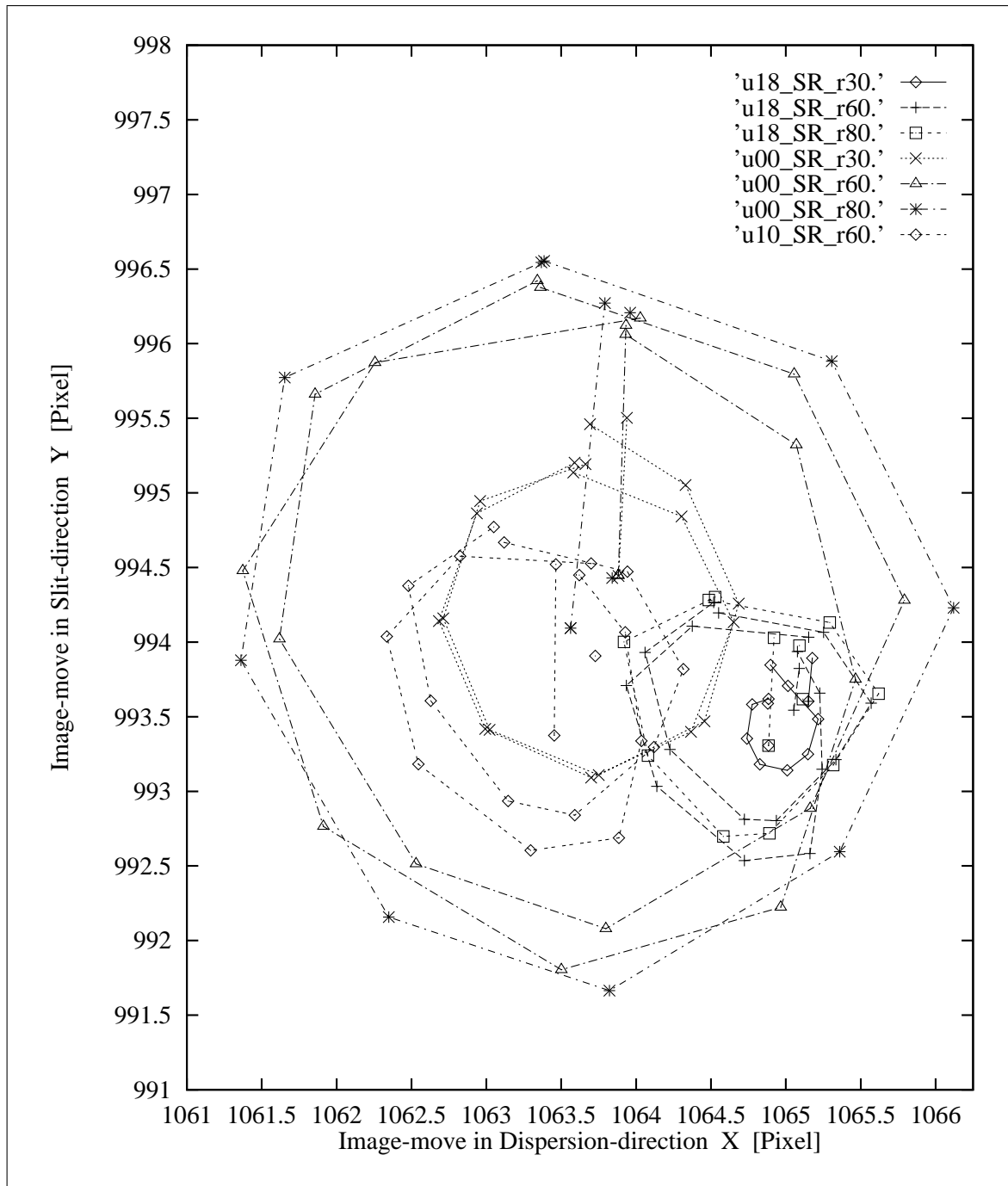
73

Figure 7.11: Image motion track of an *internal* pinhole in standard resolution SR-mode on the CCD taken in the fifth test run 'U'. The stiffening diagonals were varied from maximum (18) to minimum (00). Rotation tracks were taken for different (r30 – r80) zenith distances.
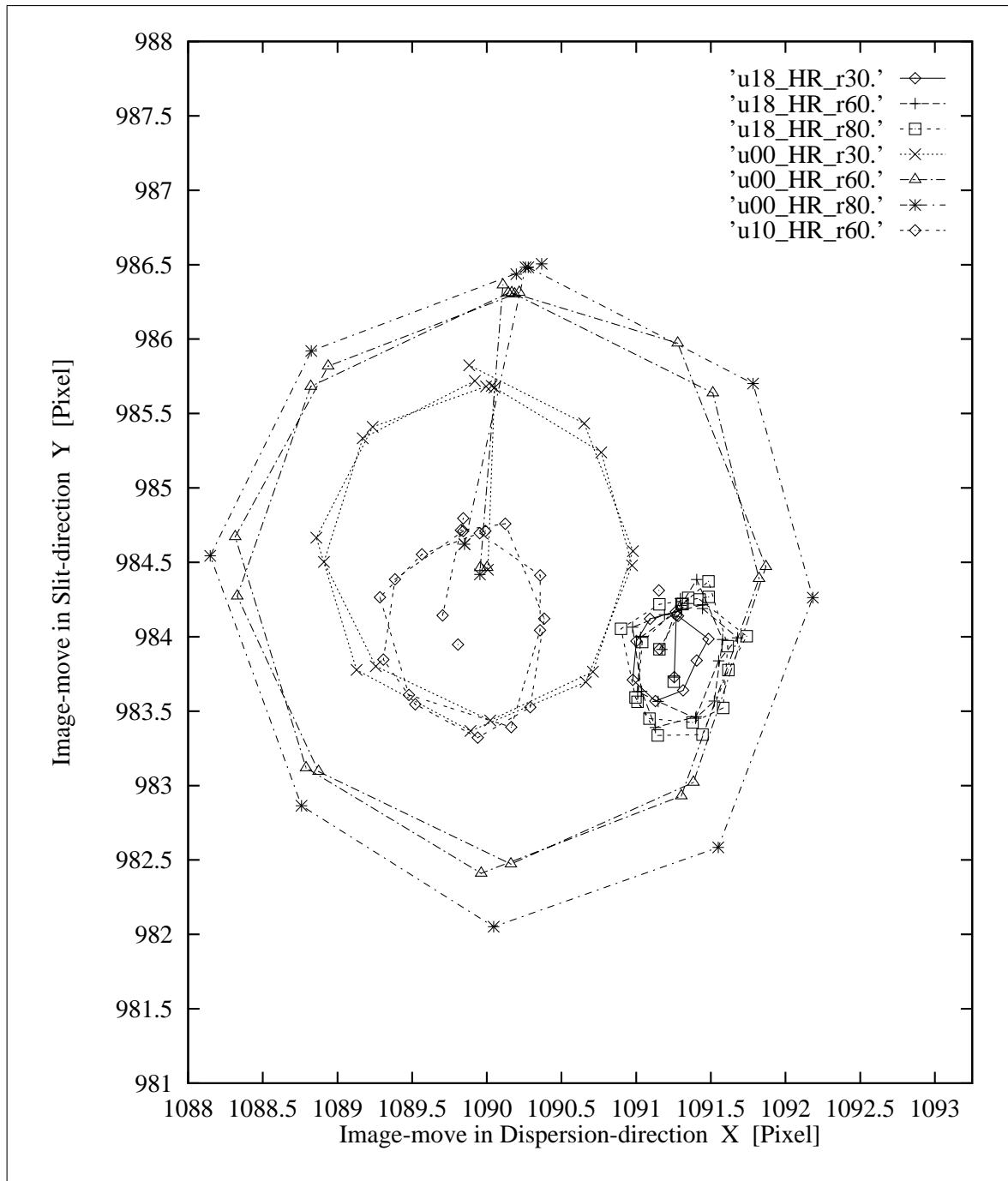
Figure 7.12: Image motion track of an *internal* pinhole in standard resolution HR-mode on the CCD taken in the fifth test run 'U'. The stiffening diagonals were varied from maximum (18) to minimum (00). Rotation tracks were taken for different (r30 – r80) zenith distances.
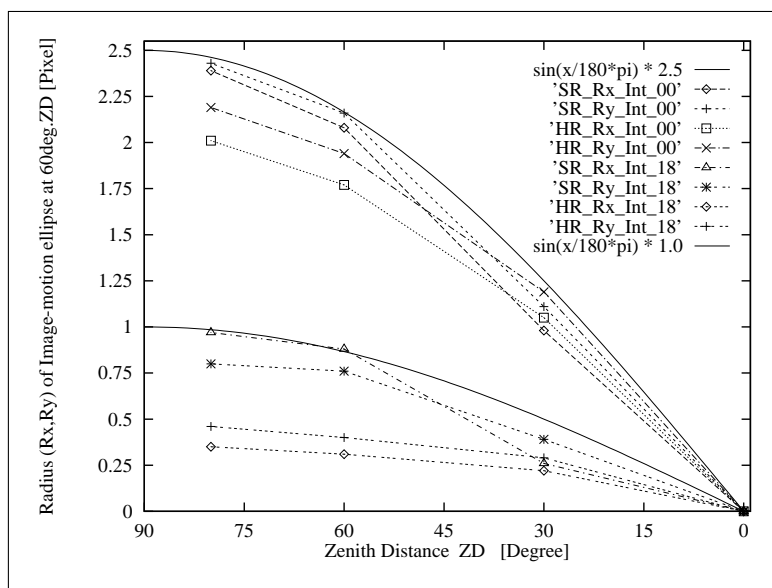
Figure 7.13: Major and minor axis of the image motion track as a function of zenith distance ZD. Plotted are the X and Y radii (Rx, Ry) of the image motion tracks of the internal pinhole (Int) for both imaging modes (SR, HR) for two stiffening setups, minimum (00) and maximum (18) diagonals. The functions obey quite good the sine component (continuous lines for minimum and maximum stiffness, respectively) of the gravity vector according to Hooke's law. The curvature of the lines indicates a progressive decrease of image motion when pointing the telescope to even smaller zenith distances.

in stiffness variation is quite rough, it confirms the principle behaviour of Fig. 7.4 seen at earlier runs. A modest increase in radius of the image motion tracks can be observed with the known turn-off when all stiffening diagonals are removed and the camera tilt follows the discontinuity in stiffness due to the replacement of tension by bending forces. Interesting is also the dependence of image motion from zenith distance shown in Figure 7.13. The radius of image wandering follows quite good a sine-law which is plotted for comparison. This confirms the expectation as the sine component of the gravitational vector is the effective momentum acting on the structures. Deviations from the sine-law were already observed at earlier runs due to non-linear forces like friction and stick-slip effects. The largest off-set of Rx radius of the SR collimator from sine (observed at $30°$ with 18 diagonals) is considered as an underestimation due to an incomplete measurement because only a single rotation track could be taken. The curvature of the sine function is independent from diagonal setup. It becomes flatter when going to stiffer configurations. There is a clear separation into two groups, one for the configuration of zero diagonals with maximal $2.5\sin(ZD)$ and the other for maximum stiffness of 18 diagonals with a sine-amplitude of 1 pixel as upper limit. The X components in radius are systematically somewhat smaller than Ry, but run parallel to each other. This results in image motion tracks of equally elongated shape. Although the 18 diagonal configuration is not yet the optimum compensation – which will be addressed later – it becomes clear that the specification on image motion of a quarter pixel is already met. One can scale the $60°$ values down to the specified exposure times of the 1 hour in SR- and maximum 2 hours in HR-mode. The radius of image wandering in SR-mode reduces then by a factor of about four to some 0.2 pixel and in HR-mode about two times to the same 0.2 pixel level. It can be seen directly in the plot that in HR-mode the images radius falls within a quarter pixel for 24 hours at zenith distances of up to $30°$. The

76

residual in image motion compensation– minimized for an internal pinhole by a maximum of the 18 stiffening diagonals – can be simply described by a sine-law with an amplitude of roughly 1 pixel in the standard resolution mode and about 0.5 pixel amplitude in the high resolution imaging mode representing the flexure compensation of the spectrograph alone without any degradations caused by telescope flange effects.

The sample of rotation tracks was sufficient for checking if image motion on the detector, specified to a maximum of a quarter pixel within 0.5–1 hour of integration in SR- and 2 hours in HR-mode, is met. The maximum rate in variation of position angle and attitude that can occur at the Paranal Observatory amounts to 15°/hour in position angle for a polar star and to 13°/hour in elevation change for an equatorial star. The last rate of elevation change differs not much from the standard rate due to the relatively close location of the site to the equator. Therefore, the standard rate of 15°/hour is taken for checking both, the image motion due to change in position and in elevation angle.

The image motion which is obtained from the rotation tracks with their step size of 45° in position angle (corresponding to 3 hours of integration time) must be scaled down by a factor of 1/3 for the SR- and 2/3 for the HR-mode, respectively. The rate in elevation change can be estimated to an upper limit by applying a correcting factor 1/4 for SR- and 2/4 for HR-mode to the radii of image motion taken from the measurements at the 60° horizon simulating a 4 hour integration.

A closer look onto the scaling as a function of elevation angle reveals a minor discrepancy to Hooke's law. According to that, one would expect a linear relation between the radii of image motion taken from the measurements at 60°, 30° and 80° zenith distance. The bending load at 60° zenith distance is already 87 % of the maximum amount that acts at full horizontal pointing. Assuming a zero spread in image motion at zenith position, which was checked and confirmed at the simulator, the radii of image motion at 30° zenith distance should be 1.7 times smaller than the 60° values – scaling with SIN (ZD) – due to the actual applying component of the gravitational vector. But the measured 30° radii are a factor of 2.5 smaller than those at 60°. This is a clear indication that progressive decrease took place in image motion when slewing from large to smaller zenith distances.

Checking the scaling with elevation angle exhibits a progressive decrease in image motion when slewing to smaller zenith distances. As a result, a large reserve in the residuals of image motion is gained for the much more frequent observations at small zenith distance if we can show that image motion specification is met at 60°. If uncertainties would remain, we could ship the instrument in this case with much more confidence to the telescope site.

7.3.3 Optimization of flexure compensation

In the last chapter, it was shown that the FORS spectrograph and imager meets the image motion specification for both simulations, the internal pinhole that detects the instrument's flexion alone as well as the external pinhole which includes the affecting simulator flange. The final image motion at the telescope depends on the real stiffness of the telescope flange. The stiffness of the mirror cell together with the telescope's attachment flange, the Cassegrain Adapter-Rotator of the VLT, was estimated by an FEA. Although any motion, introduced by the flexion of the primary mirror cell, shall be cancelled out by the telescope's guide probe, the flexure of the

Adapter-Rotator itself cannot be compensated for because the guide probe is an integral part of the Cassegrain adapter. Any flexion (motion or tilt) of the Adapter-Rotator will cause an image shift within the focal plane of the telescope, coincident with that of the spectrograph. The values referred to in the ESO report on finite-element analysis of the Cassegrain Adapter/Rotator [23] are only indicative and amount to the magnitude of 20μm. This shift in the telescope's focal plane is one half of the motion that was introduced by the simulator flange and covers the range of stiffness that one expects for the telescope flange. The telescope should be stiffer than the simulator flange which suffer under tilt due to the bending of a plate that connects the larger diameter of the instrument flange with the smaller diameter of the rotary bearing. On the other hand, the telescope flange can not be simulated regarding stiffness with the internal pinhole because this pinhole already simulates a flange of infinite stiffness. The real behaviour at the telescope is therefore expected to fall in between the two investigated simulations, that with the external and with the internal pinhole.

A sample of image motion tracks of this two limiting cases are shown for comparison in a single plot (cd Fig. 7.14) for the 10 diagonal setup. The tracks of simulation run 'r' reflects the motion including flange weakness of some $50\,\mu$m. Those of simulation run 't', 'u' and 'Mos' display the residual image motion of the internal pinhole excluding any flange effects. We will emphasize here that the SR-mode tracks scale with zenith distance and keep shape and orientation for all cases – which keeps valid also for different diagonal setups – that means *over*-compensation is maintained in SR-mode every time. In HR-mode, the shape of the tracks is kept for all zenith distances and setups, but it switches from over- into an under-compensation when changing from internal to an external pinhole. The optimum compensation due to both, instrumental *and* real flange flexion, would be a rotation track with a diameter of ≤ 1.5 pixel, equal for both imaging modes, but with over-compensation (closing of image motion track at the top) for the standard resolution and with under-compensation (closing of motion track at 6 o'clock) for the high resolution mode.

The final image motion would fall onto to this optimum if the real flange stiffness of the telescope adapter/rotator will amount to half of that of the simulator, as the finite-element calculation of the adaper/rotator already suggests. The rotation track at the telescope should therefore fall between those of the 'r10' and 'u10' run. Dividing the flange effect in half of its amount reduces – similar to the re-stiffening amount of 18 diagonals – by some 20% to about 0.5 pixel radius for $60°$ ZD observations. This corresponds to an residual in image shift of $\frac{1}{8}$ pixel/hour in standard resolution imaging mode. In HR-mode, the variation range is much larger, but passes the zero point of compensation. Therefore, the track in between 'r10' and 'u10' test run will obtain 0.3 pixel diameter then which increases – similar to 18 diagonals stiffness increase – by some 40 %. This will result in an effective image motion residual of $\frac{1}{8}$ pixel/2 hour in the high resolution imaging mode. The specification of a quarter pixel of image motion over one and two hours of integration in the SR- and HR-mode, respectively, will therefore be met. Moreover, the 10 diagonal setup will be the optimally configured flexure compensation if the scaling outlined above will be confirmed at the telescope.

We also want to emphasize that we consider this amount to be the minimum to be obtained because the shape of the tracks become more and more irregular as compensation works better. The small residuals of tiny effects – such as motion of the CCD detector itself within its mount for instance, which we cannot counteract – become apparent when flexure compensation works at its best.
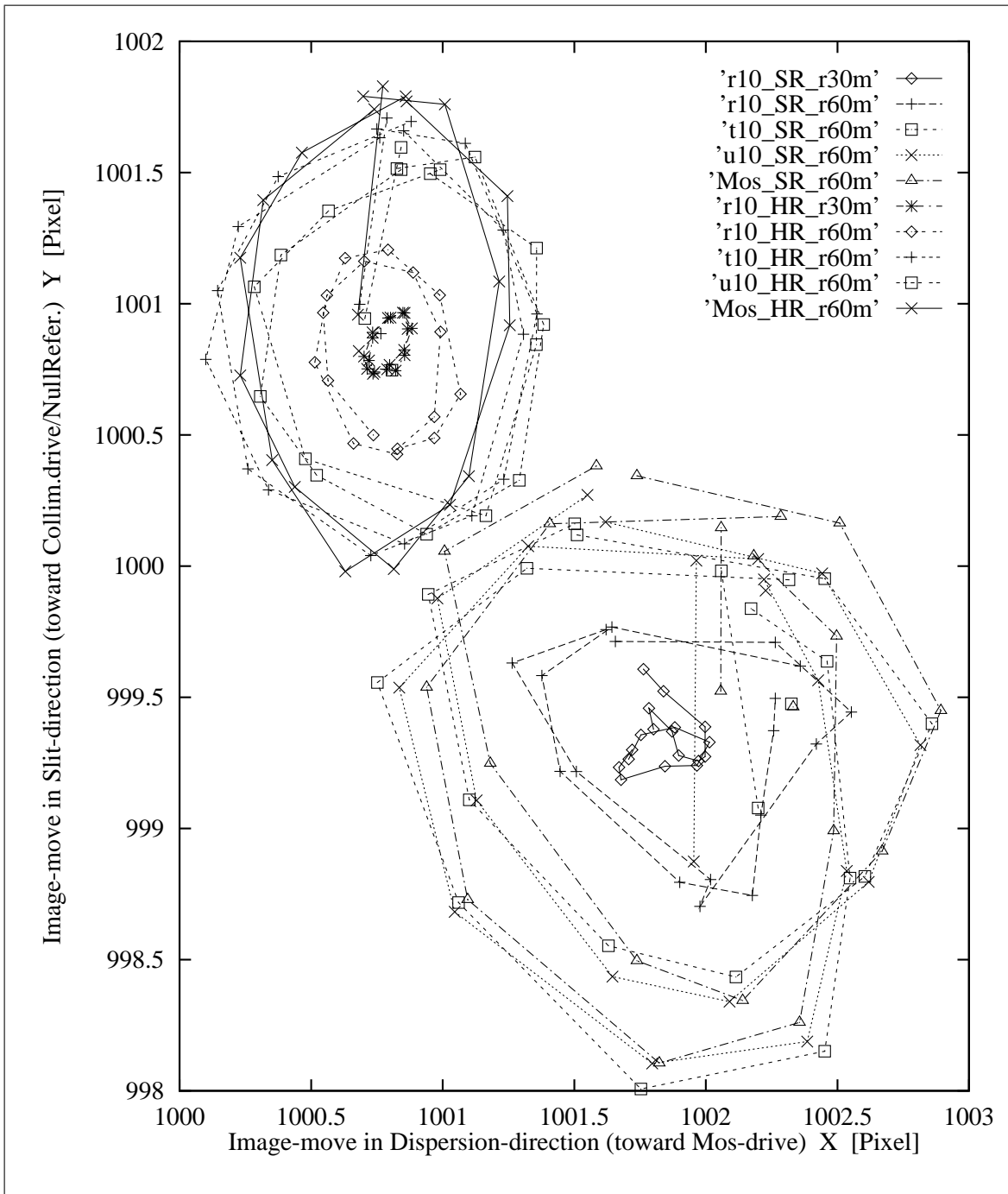
Figure 7.14: Final sample of image motion tracks obtained in standard spatial resolution (SR) and high spatial resolution (HR) imaging mode. They were taken in different test runs with different pinholes; 'r' denotes external, 't' and 'u' internal pinhole and 'MOS' a single slitlet. For comparison and scaling purposes, all rotation tracks were taken for a single setup of 10 stiffening diagonals. Taking into account the calculated flange effects, the track finally obtained in SR-mode at the telescope should coincide with the 'r10_SR_r60m' track of 0.5 pixel radius. The HR-mode then should fall at the telescope quite close to the 'r10_HR_r30m' track of 0.25 pixel radius, but then at 60° zenith distance. Scaling these values down to real observing in SR- and HR-mode leads to 1/8 pixel of image motion per 1 and 2 hours of integration time, respectively.

7.3.4   Motion of focal plane equipment

In order to separate any motion of focal plane equipment (like mask pinholes or MOS-slitlets) from pure image motion compensation, the central slitlet of the MOS unit was measured simultaneously to the optical estimates of image motion. Two precision gauges were mounted to the central simulator flange that detect mechanically any displacement in the two orthogonal planes, that coincide with the principle stiffness planes of the instrument. The gauges were fixed within the instrument's focal plane, 250 mm apart from the mounting flange. They were tested on their flexure to obtain the required accuracy of microns. The reproduction accuracy for repeated instrument positions were confirmed to $\leq 1\,\mu$m. These gauges did detect in separate test runs the motions of both, that of the MOS unit as a whole and that of a single slitlet. The gauges' mount contained also a pinhole that allowed for checking the stability of the gauges during the test run through optical image motion confirmation. Images of that 'external' pinhole were taken simultaneously with the CCD detector and compared with existing image motion residual tracks for that purpose. These tracks were almost identical with those of prior test runs and they confirm two assumptions. First, that the gauges are stable with respect to the focal plane and second, that both external pinholes were stable to the same amount although they were mount on different structures.

The two gauges did detect a perfect circle for the motion of the MOS unit itself with respect to the simulator flange. The tracks (Focl_ in Figure 7.15) were taken for both collimators, standard (SR) and high-resolution (HR), for different zenith distances. The change of collimators within the optical beam did not show any effect on the MOS motion and confirmed that no deformation from the collimator into the top section could be observed and obviously not causing any 'print-through' of collimator section deformation onto MOS unit motion.

The dependance of the motion on zenith distance (Fig. 7.16) matches a sine function perfectly with an amplitude of $45\,\mu$m at the maximum of horizontal pointing. The measurements covered also the flexure of the simulator flange which add to the motion of the MOS unit alone. One has to take into account this effect by subtracting its amount of some $40\,\mu$m which will be addressed later. The effective motion of the MOS unit within the common focal plane, shared by the telescope and the instrument, therefore reduces to a low $5\,\mu$m. This stability of any instrumental masking device, contained or mounted to the MOS unit, is of extraordinary quality when transformed into the apparent motion on the sky of $0''\!.04$ and $0''\!.02$ in SR and HR mode, respectively.

At the second, the motion of a single slitlet was detected mechanically at its slit-carrying tip with one gauge for each component. The motion forms a perfect elliptical track (Fig. 7.15). The long and the short half-axis each obey perfectly a sine function (Fig. 7.17). The one component (s180) departs gently from the sine wave which is caused by frictional hysteresis within the linear motion guide of the slitlet when momentum is acting on the 1 mm balls of the cages. This kind of hysteresis was already addressed severally within this chapter. It is the same effect that could be observed when taking the image motion tracks with the two collimators. They both are resting on the same kind of linear motion guides, but of much larger dimensional stiffness, as mentioned earlier in the design description. The effect is obviously larger for the standard han for the high-resolution collimator due to its significant higher weight and decenter-of-gravity resulting in a much larger effective momentum acting on the 6 mm large balls of the collimator motion guide.

More obviously is the elongation of the elliptical track i.e. the difference in amplitude of an additional $50\,\mu$m. It reflects the bending flexure of the cantilevered slitlet beam when loaded by a momentum with the gravity vector running parallel to the slit direction (Y). This bending leads to a misalignment i.e. non-parallelism of the slit jaws that was already tested during integration for each slitlet of the MOS unit separately. Those mechanical tests confirmed the design calculations of about 2 micron of inclination for each single slit jaw along its $12\,$mm length. The bending of the cantilevered beam amounts to little less than $1.5\,\mu$m. Taking into account the additional flexure of the quarter-metre cylinder lengths of the linear motion guides enlarges the inclination to a total of some $2\,\mu$m. Transforming the $250\,$mm slitlet outrigger length into the $12\,$mm slit length reduces the observed $50\,\mu$m displacement to less than $2\,\mu$m misalignment of the single slit jaw. This is another confirmation of the MOS and the slitlet stability as well as of slit quality.

The amplitude in X of $52\,\mu$m is by $7\,\mu$m larger than the motion detected for the MOS unit itself. This amount reflects the slitlet motion within the MOS unit under tensional force and fits perfectly to the compensation track that was taken optically from the image of a slit jaw, given as track 'Mos_SR' and 'Mos_HR' in Fig. 7.14. This displacement is a composition in lack of tensional strength of the slitlet carrier and mount as well as torque stiffness of its drive gear, brake and friction clutch. Transferred into displacement on the sky, slit decentring amounts to $1/20$ arcsec and $1/40$ arcsec or tenth of a pixel during spectroscopic observations with either the standard (SR) or the high-resolution (HR) collimator, respectively. That this will not affect image quality of the image motion residual can be seen in the identical shape of the tracks of Fig. 7.14 taken with the internal pinhole t' and u' and with the image Mos' of a slitlet itself.

7.3.5 Flange effects

It was already mentioned several times, that the stiffness of the attachment flanges influences on a minor scale the residual of image motion compensation. This will be advantageous in a sense that image motion compensation is able to take into account this effect and in principle counteract and include it into the compensation. The influence of flange weakness became apparent after changing the imaging of an internal into an external pinhole. Therefore, this effect was addressed in a separate investigation through analyses and test runs.

First of all, the flange unit of the telescope simulator was re-modelled within the computer and analysed with finite-elements regarding stiffness. When applying the effective momentum, caused by the cantilever attached instrument, the flange suffers flexure mainly from stepping in diameter from the $0.7\,$m rotary bearing to the $1.5\,$m attachment flange. The resulting tilt amounts to 110–$120\,\mu$m at $750\,$mm radius. This $35''$ tilt by the flange weakness caused an instrumental shift of $42\,\mu$m with respect to the focal plane of the telescope at $250\,$mm back focal distance. This agrees quite well with the test result of the last section when MOS unit motion was detected mechanically with respect to the simulator flange.

A small discrepancy of some 3–$5\,\mu$m still remained, caused by the flexure of the top section's housing that 'prints through' as a movement of the MOS unit. This minor contribution was tested with the existing hardware of FORS2. The housing structures were procured for both instruments simultaneously. This opened up the chance to actually measure the housing displacement with real hardware through simulating the bending momentum. For this measurement, the housing sections of FORS2 were mounted together and where bolted up-side down
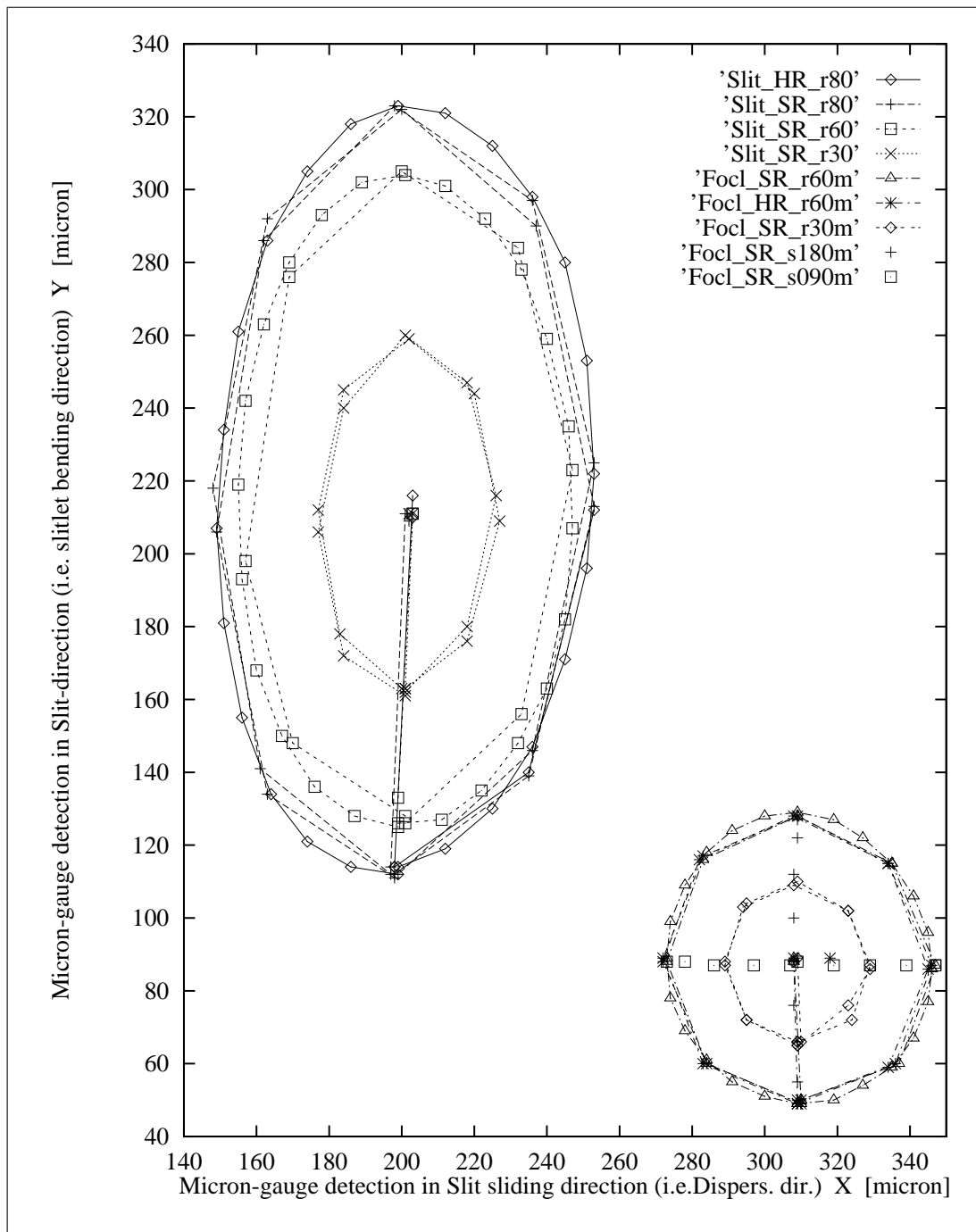
Figure 7.15: The motion of masking equipment in the focal plane, detected by separate micron gauges. The motion of the MOS unit itself (Focl) is a perfect circle due to flexure. The mechanical measurements cover rotations at different zenith distances (r30, r60) as well as slews along the two principle planes of stiffness (s090, s180). Additionally, the outermost tip of a single slitlet (the central one of the MOS unit) was measured (Slit) on the CCD detector. The slitlet motion is largely elongated due to bending of the cantilevered beam of 250 mm length that add to the flexural motion of the MOS unit itself. The motions were totally independent from the collimator (SR) and (HR) that rest within the optical beam for image motion confirmation.
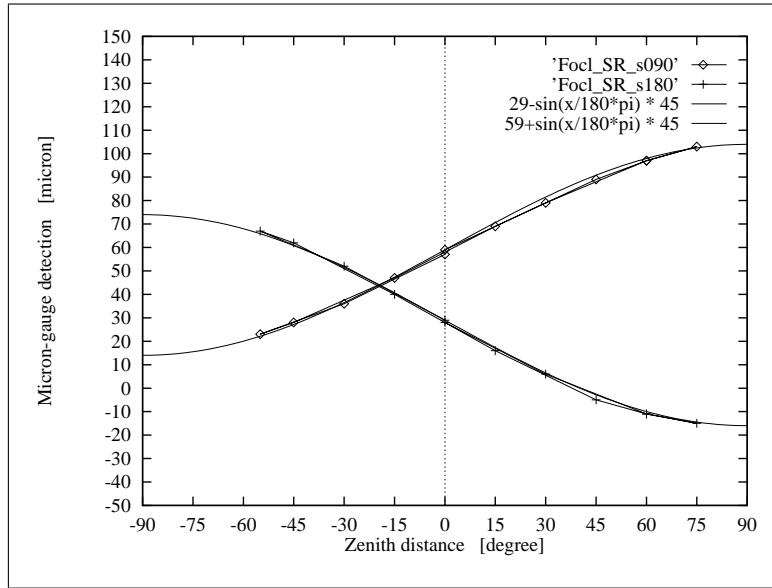
Figure 7.16: The apparent motion that was detected at the MOS unit obey a perfect sine function, also drawn for scale. The amplitude of the sinusoidal wave amounts to 45 μm which reflects to the biggest part the weakness of the simulator flange which amounts to about 40 μm according to analysis. Subtracting this dominating effect leads to an residual as low as 5 μm of MOS unit motion within the telescope's focal plane. The additional constant of the sine fit is arbitrary due to the zero-point of the gauges.
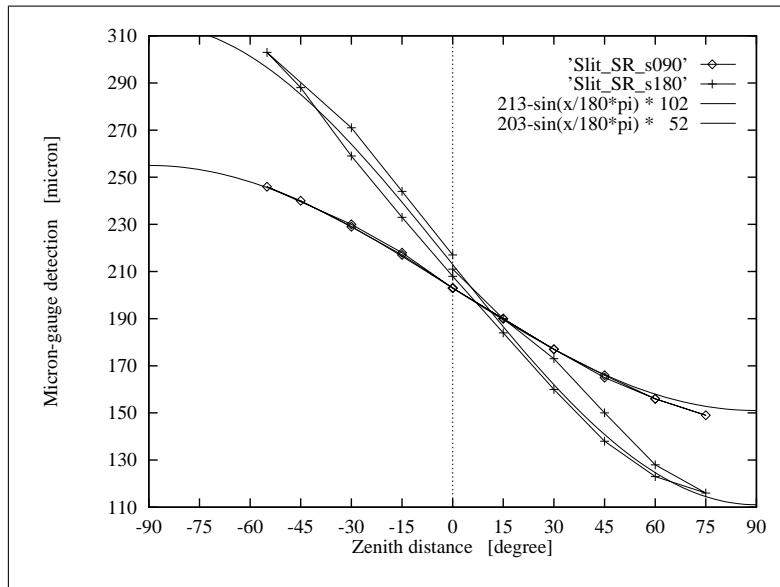

Figure 7.17: The motion that was observed for a single slitlet at its outermost tip follows perfectly a sine function. The small deviation for the one component (s180) is caused by frictional hysteresis taking place when momentum is acting onto the 1 mm balls of the cages of the MOS unit's linear motion guides. This also causes the high amplitude which is 50 μm larger than for the tensional load case (s090) and also a non-parallelism of the slit jaws, but more than 20 times smaller from geometric ratios. The additional constant of the sine fit is arbitrary due to the zero-point of the gauges.

83

onto the concrete floor of our testing facility. The acting momentum was applied to the housing through loading a crane-weighing machine with a tackle block, laterally attached to the wall. Mechanical gauges were placed at different locations of the housing to detect the deformations and displacements.

Taking into account that the concrete floor was not perfectly stiff – which turned out surprisingly during the measurement – the displacement of the MOS attachment console was pinned down to $5\,\mu$m with respect to the instrument attachment flange. This real value fits perfectly well with the residual that remains when subtracting the flange movement of the FEA from the gauge measurements, detected at the telescope simulator. No discrepancy remains between all the measurements and the analyses.

7.4 Flexure tests on bending characteristics in spectroscopic mode

When switching from imaging to spectroscopic mode, an optical component went into the beam, that could add to image motion and would disturb its high quality in compensation. The stability of the dispersing element, in case of FORS that were the grisms i.e. grating prisms, within the optical beam was checked via shifts of spectra on the detector. Three grisms, out of the available seven, were moved into the beam in order to detect any possible tilt of the grism 'filter'-wheel or of its mount. Reference exposures were taken to determine shifts of the spectra relative to that. The slewing of the telescope simulator followed identical tracks for all measurements taken with spectroscopic and polarizing optics as well as for reference. The simulator slewed from zenith to 60° ZD and performed two ±90° turns at this near horizontal pointing. The reproduction accuracy of the measurements was checked to be within 0.02–0.03 pixel.

The shift of the spectra, relative to the reference, was measured to 0.03–0.05 pixel which was close to the detection limit. The effective tilt of the dispersing optics could therefore be estimated to less than 1 arcsec. Thus, all three exchange wheels – the grism-, the broadband-filter- and the Wollaston-wheel – were considered as perfectly stiff with respect to the parallel beam.

The polarizing optics, Wollaston and the two phase-retarder mosaics were tested in the same way as it was done for the grisms. Moving the Wollaston prism together with the $\lambda/2$ or the $\lambda/4$ phase-retarder plate into the parallel beam led to a shift of 0.03 pixel relative to the reference, taken at zenith. The causing tilt of about 1 arcsec belongs to the huge Wollaston prism because the phase-retarder mosaics were plane-parallel plates.

Thus, the stability of this analyzing optics, which is close to the detection limit, was very convincing and did match specification perfectly.

7.5 Flexure compensation at the VLT Unit Telescope

Testing and verifying the flexure compensation at the telescope was covered by the Commissioning Plan which did foresee a twofold test, a) imaging of the longslit's internal pinhole and b) taking long exposures of 1 hour (SR) and 2 hours (HR) with great slews in elevation at two (0°,90°) position angles.

In the first test, the internal pinhole of the longslit mask should be illuminated by the calibration screen and imaged onto the detector during telescope slews that follow the same slews in elevation and position angle as it was done formerly at the simulator. These image tracks were compared with those taken at simulator in the integration hall. These tests at the real telescope showed that we had to re-stiffen the instrument because we did need less tilt of the camera section. The larger stiffness could be easily gained by mounting 8 additional to the existing 10 diagonals at the places that were already prepared for their fixation. The flexure compensation was re-checked with the internal pinhole for this new, stiffer set-up. The tracks, obtained again at the telescope, looked as perfectly as it was obtained (for the 10 diagonal set-up) at the simulator with the tracks 'u10_SR_r60m' and 'u10_HR_r60m' that are shown in Fig. 7.14, but with closing the elliptical track at 12 and 6 o'clock for the SR and HR node, respectively. This indicated clearly a perfect out-balancing between the two imaging scales due to an over-compensation for the standard and an under-compensation for the high spatial resolution mode, as outlined in previous sections.

The second test campaign was performed under real observing conditions by taking long term exposures on the sky. These tests did also cover the tracking performance of the telescope. The Fors Deep Field was selected as a suitable field for this purpose because it is located in the sky on a declination that is nearly identical with the latitude of the observatory's site which was one of the criteria for selecting this field for the scientific programme, as described in chapter 9.2.3. This property led to a track on the sky that raised nearly with the maximum climbing rate of 15°/hour in elevation and without larger disturbing change in position angle on long terms. This track could be followed till a few minutes before passing the zenith with its blind spot which is inaccessible for a tracking telescope and which enforces a 180° turn over in position angle.

The observational track, that span like a meridian circle across the sky, was split into exposures of the following kind. The sequence started with a short 2 minute exposure, than the 1- or 2-hour exposure was separated into adjacent 30 minute images and finalized again by a short 1-minute exposure. Evaluating these images on any point-source shifts exhibited no differences in the coordinates, obtained with the centre-gauss command of MIDAS, of larger than tenths of a pixel. This measurement accuracy was at the time of commissioning the limit of decenter detection. This also means, that the residual in compensating the image shift due to instrumental flexure was totally hidden behind the seeing disk, combined with the telescope's tracking accuracy. Remembering the compensation residuals, taken with simulated point sources at the simulator and the telescope, clearly indicated that there would be no chance to detect those small values under real observing conditions at the telescope which was fully confirmed. Another interpretation of this observation is, that the specification on image motion – that was matched by the Fors instruments – was set correctly to an amount that it shall not further deteriorate the telescope's imaging quality, dominated by seeing and tracking error, which did our observation confirm.

7.6   Conclusion

The comprehensive tests on flexure compensation fully confirmed, that the structural behaviour of the Fors instruments – including the mechanical balancing for image motion compensation – was well understood by us and that our final theoretical computer-modelling did match the real

instrument very precisely. This model was fully consistent with itself and also with a wide range of set-up variations, as the comparison of the test with the computer results clearly showed.

This put us into a position to predict any displacement and tilt of opto-mechanically relevant parts for all instrumental orientations and positions on the sky. The hardware was thus shipped to Chile with the lowest uncertainties in structural behaviour and with the highest confidence in adapting it to the reality that we would face at the VLT.

Chapter 8

The First Scientific Application of the VLT

8.1 The '1st-Light' of FORS

The '1st Light' took place in the evening of September 15th, 1998. The event was scheduled three days earlier but a broken cooling line of the telescope's Cassegrain adapter poured a water-glycol mixture into the instrument. Fortunately, the instrument mechanics and optics was not damaged but needed to be cleaned and dried properly. For doing this, the separation into units, sub-units and components took place in the dome environment and the process lasted three days before reattachment to the telescope flange could be finished successfully.

With the moment of 1st-Light, when the exposure shutter of FORS1 opened the first time with a telescope in front of it, the freshly finished UT1 – unit telescopes UT2 to -4 were still under construction then – obtained for the first time useful light for scientific investigations and an ambitious European project changed from a technical challenge into a scientific machine. This event marks such a major milestone for the project as well as for the research organisation that several press releases were issued of which the main can be found at http://eso.org/ outreach/ press-rel/ pr-1998/ pr-14-98.html .

The very first image (Fig. 8.1) was taken when the shutter opened on 1998–Sept–15 at 20:25 local time for the first time with the telescope pointing onto the sky. An exposure sequence of small window read-out had be performed in advance in order to focus the telescope properly. This first full frame was checked regarding proper focussing over the entire $6.8' \times 6.8'$ field of the view. The inspection revealed a seeing disk of 0.64 arcsec at FWHM and no field-dependent defocusing due to a possible tilt of the detector plane.

Right after checking the focus in the total FOV, the unit telescope slewed onto an equatorial field in the constellation Pisces where a galaxy cluster and a known QSO PB5763 is located (Fig. 8.3). The quasar can be seen as a pointlike source at about 2 o'clock close to the right edge. At lot of field galaxies – or maybe members of other, more distant clusters outside the FOV – are visible in the right half of the frame, additional to the prominent galaxy cluster in the lower left which was not thoroughly investigated so far. Numerous faint galaxies form this distant cluster. Several of them exhibit peculiar shapes which can be seen in the zoomed

image (Fig. 8.4). The view is dominated by a large spiral galaxy under oblique angle which shows perfect symmetry up to the outer tips of its long spiral arm extensions. They can be understood as tidal arms due to interactions, not uncommon in such densely crowded clusters. Strange appearance shows the elliptical galaxy to the left of that spiral. It carries obviously a ring structure of material as an equatorial belt around its main body. The belt rotates perfectly perpendicular to the main axis of the elliptical and is a good example for a tri-axial elliptical galaxy.

One of the next objects of interest became the large spiral galaxy NGC 1232 due to its favourite position on the Paranal sky, its beauty and its possible similarity to our own galaxy. Figure 8.5 shows a spectacular view of the spiral structure and its apparent companion. The picture is a colour composite image taken through three different filters, U, B and R. The older population of stars becomes emphasized due to their reddish colour near and within the central bulge whereas the outer regions are dominated by young, blue stars and regions with still on-going star formation. An obviously accompanying galaxy is highly distorted by the gravitational impact of this massive spiral. At least two galaxies, several ten times more distant than NGC 1232 but still bright enough, are shining through the less dense parts of the spiral arms at 12 and 2 o'clock. With a distance of some 100 million light-years, NGC 1232 is about 3–5 times more distant than the famous Whirlpool galaxy M51. Due to the excellent seeing conditions and the performance of the VLT/FORS combination, this picture shows details that were formerly recognized only in nearby galaxies.

In the very first days of commissioning, when mostly boring images were taken to evaluate the technical performance, time was left for such interesting objects like the remnant of the supernova SN87A which exploded 1987 in our neighbouring accompanying galaxy, the Large Magellanic Cloud. Eleven years after the explosion, the outer shell of the progenitor star is receded that far from the central compact object (a neutron star ?) that it can be clearly recognized as a ring like assembly of matter illuminated by the central star (Fig. 8.6). This quality of images can now be taken from the ground by earth-bound telescopes which opens new opportunities for scientific research that were subject to the 'Hubble Space Telescope' before the VLT's '1st-Light'.

8.2 Commissioning

The commissioning of the FORS instrument separated into two phases of different objectives and tasks. In the first, the Commissioning 1 phase, the instrument was embedded into the hardware and into the software environment of the observatory. After hard- and software embedding, technical and scientific data were taken with the integrated system of telescope and instrument. Those data required a thorough reduction and investigation regarding quality and fulfilment of the specifications which was done in a week long period between the two phases at the home institute. After evaluating the gathered and reduced data, the technical team travelled again to the observatory for the second, the Commissioning 2 phase to finalize its work.

8.2.1 Objectives

The objectives and tasks of the two commissioning phases are presented in form of a short summary which will cover only the most central issues. Table 8.1 lists the objective, the task, the phase and the amount of time that was spent on this task.

8.2.2 The Phases

Above, the objectives and tasks of the different phases of

- Transport and Integration,

- Commissioning 1, and

- Commissioning 2,

all taking place in Chile, were outlined. Presenting the results finally obtained during Commissioning 2 to ESO led to the 'Preliminary Acceptance in Chile' of the FORS1 instrument that mark the begin of the last phase, the 2-year term of technical support and of warranty.

After preliminary acceptance, the so-called 'Science Verification Phase' followed immediately which was performed by ESO astronomers. They did check the quality of the scientific data independently from the instrument team. The data were obtained in all observing modes in a three-week period and then reduced in a proper way, like for a real proposed observation, in order to assess the value of science data that could be gained with FORS.

'Final Acceptance in Chile' took place after the two-year period of warranty which marked officially the ultimate acceptance of FORS1 through the customer ESO. This last milestone was obtained 10 years after publication of the proposal to ESO in the year 1991 [43].

8.3 The '1st-Light' of Fors2

The 1st-Light of FORS2 – the second copy of the two imager and spectrographs – took place in the night of October 29th, 1999, only two days after transport and attachment to the telescope and only one year after its predecessor FORS1. Bringing FORS2 within two days into operation at the telescope was extremely efficient when compared to its twin that suffered under an invasion of a water-glycol mixture from the telescope's adapter the day when it was mounted the first time to the telescope. Everything run very smoothly also due to the experience that was gained the year before with FORS1. The same plan was applied for commissioning FORS2 except that the 'Mask Exchange Unit – MXU' was added to that copy which had to be tested and integrated into the telescopic environment too. The commissioning split also into two phases with a separation of several weeks for data examination and evaluation.

The end of the Commissioning 2 phase marked the 'Preliminary Acceptance' of this instrument in Chile. A two-year term of technical support and warranty followed this acceptance before ESO announced its 'Preliminary Acceptance in Chile'.

Objective	Task	Phase	t
Re-Integration prepar.	unpacking and site preparation	Integrat.	5d
Re-Integration	mount pre-assembled units, modules, LRU,sections	Integrat.	11d
Hard-& Software funct.	test all moving functions, electronics and software stand alone off the telescope in integration hall	Integrat.	5d
Storage	preparation for safe storage for period of months	Integrat.	2d
INTEGRATION	in total	Integrat.	**23d**
Transport prepar.	unpack sealed instrument in storage, funct. tests, remove critical items, protect against environment	Comm 1	5d
Transport	lift totally integrated instrument onto the truck prepare unpaved road to mountain top,plan+wet guarded transport from integration hall to the top unload truck with mirror exch.facility,lift into dome	Comm 1	1d
Telescope mounting	align and mount instrument to the teles.flange functional tests, mount critical items,analyz.optics	Comm 1	2d
Unforeseen accident	liquid infiltration from telescope's Cass.adapter by burst cooling line requ.detachment, disassembly, drying&repair, re-assembly&attach to telesc.flange	Comm 1	3d
The 1st-Light	clearing light path and exposure shutter opening	Comm 1	1d
Imaging mode	moving funct., imaging optics, filters, scales check	Comm 1	2d
Flexure evaluation	image stability check under real telesc.conditions	Comm 1	3d
Spectroscopic mode	re-check & integrate Multi-Object-Spectroscopy	Comm 1	3d
Longslit mode	re-check & integrate longslit spectroscopy	Comm 1	1d
Polarimetry mode	re-check & integrate polarimetric imaging	Comm 1	1d
Spectro-Polari. mode	re-check & integrate polarimetric spectroscopy	Comm 1	1d
Telescope software IF	align telescope&instr.coordinates&communicat.	Comm 1	2d
Data management IF	embed data management&handling in obs.environ.	Comm 1	3d
Photom. zero points	determine zero-points of photometric system	Comm 1	1d
Polar. angle reference	measure&align polar.refer.angle by Glan-Thompson	Comm 1	1d
Photometric accuracy	determine the photometric system	Comm 1	1d
COMM 1	in total	Comm 1	**31d**
Last modifications	dismounting, modify calib.path, remounting	Comm 2	3d
Instr.characterization	determine 27 items; dispersion,resolution etc.	Comm 2	5d
2nd water infiltration	leakage within telescope Cass.Adapter/Rotator dismounting, drying and remounting to telescope	Comm 2	2d
Observing templates	test all observing modes & templates; 10 items	Comm 2	5d
Photom. zero points	re-check zero-points of photometric system	Comm 2	2d
Data management IF	fine tune data management, handling & storage	Comm 2	3d
Acceptance tests	test all available functions & modes; 11 items	Comm 2	5d
COMM 2	in total	Comm 2	**25d**

Table 8.1: Listing of the objectives, the tasks, its phase and the elapsed time t (in days) that were performed during the two commissioning periods of FORS at the Paranal Observatory.

After fine tuning all software interfaces with the Paranal environment at the end of Commissioning 2, the same 'Science Verification Phase' followed as for FORS1, performed by ESO astronomers. This independent check under real observing conditions confirmed the quality of the gathered data as it was shown by the instrument team. The warranty period ran out in the year 2002 which marked the 'Final Acceptance in Chile' of FORS2 but also the successful end of the FORS Project itself.

8.4   Guaranteed Time Observing Programmes

The development, construction, installation and commissioning of the two FORS imager and spectrographs was a ten years effort for the three participating institutes of the 'VLT Instrument Consortium'. As compensation for this effort, ESO granted about 60 nights of observing with the brand new VLT to the consortium. Those observing nights had to be spread among the scientists of the partners to equal amount for the 'Guaranteed Time Observations', the GTO Programmes.

Several workshops have been held well in advance of '1st-Light' in order to organize the optimal use of this GTO time with a maximum in scientific return for those institutes. After three workshops under the leadership of the PI, 35 programmes of very different size and amount of integration time turned out basically (Tab. 8.2). Each of them was given a scientific rational and observational proposal [34] which passed the 'Observing Programme Committee' of ESO for judgement.

The span of proposals range from solar system bodies (like Trans Neptunian Objects) to the cosmological edge i.e. Deep Fields, Gamma Ray Bursts (GRB) and Gravitational Telescopes, so-called for the focusing effect of gravitational fields produced by very massive and/or concentrated objects like Black Holes or Galaxy Clusters. This underlines the character of the two FORS copies that were built as multi-functional instruments.

One GTO programme, the No. 1 in the listing of Table 8.2 was given highest priority. The main reasons for the high ranking of the FORS DEEP FIELD Programme above other GTO programmes were:

1. It could hardly become a General Observers programme,

2. it required large amount of observing time,

3. it required large resources of all three partner institutes in respect of the shared GTO integration time and manpower for data reduction,

4. it was of scientific interest for all three partner institutes and moreover for a large scientific community,

5. it was especially well suited for observations with the powerful VLT/FORS combination,

6. it should deliver compelling results that can be compared directly with data taken by the Hubble Space Telescope in the two deep fields, HDF-North and HDF-South,

7. it promised a maximum in scientific return.

Prg. No.	Programme Title	Principal Investigator
1	The FORS DEEP FIELD	Appenzeller
2	Gravitational Telescope Survey of Distant Galaxies	Seitz
3	Galaxy Transformation in Clusters	Fricke
4	The Fundamental Plane and the $M_{g-\sigma}$ relation of cluster ellipticals at high redshift	Saglia
5	Gamma-Ray Bursters	Beuermann
6	Coronal Lines from Cooling flows	Wagner
7	Intracluster planetary nebulae in the Virgo Cluster	Mendez
8	Extragalactic planetary nebulae as distance indicators and tracers of mass distribution in early-type galaxies	Mendez
9	Multicolour Photometry of Globular Cluster Systems	Wagner
10	The Ultraviolet Spectral Characteristics of the Quasar Population at $z > 4$	Dietrich
11	Spectroscopy of Faint X-Ray Sources	Kümmel
12	Circular Polarimetry of Blazars	Wagner
13	Host galaxies and environment of intermediate redshift AGN	Jäger
14	Spectropolarimetry of AGN	Kollatschny
15	Spectrophotometric observations of southern Blue Compact Dwarf galaxies	Papaderos
16	Follow-up spectroscopy of low-mass PMS candidates in the LMC	Krautter
17	Field topology of magnetic white dwarfs	Reinsch
18	The nature of supersoft X-ray binaries	van Teeseling
19	A mass-function for the black hole candidate V821 Ara (GX 339-4)	Hessman
20	Phase resolved spectroscopy of Pulsars	Mantel
21	Multi object spectroscopy of supergiants in nearby galaxies	Kudritzki
22	White dwarf masses in faint cataclysmic systems	Häfner
23	The pre-cataclysmic binary NN Ser	Simon
24	Photo-polarimetry of Pulsars	Wagner
25	Spectroscopic echo tomography and doppler imaging of reprocessing sites in X-ray binaries	Barwig
26	The faint end of the luminosity function in globular cluster M4	Schweitzer
27	Probing the inventory of minor bodies in the outer solar system	Böhnhardt
28	Spectroscopy of MUNICS K'-band selected Galaxies	Drory
29	Stellar Populations in Cen A	Wagner
30	Probing the Formation of SO Galaxies using Globular Clusters	Ziegler
31	The Thermal Emission from isolated Neutron Stars	Gaensicke
32	Ultra-fast Spectroscopy of Accretion Disks	Hessman
33	Ultra-fast Spectroscopy of Magnetic CVs	Beuermann
34	Spectroscopy of Tidal Features of NGC 7252	Weilbacher
35	Optical Spectroscopy of Isolated Old Neutron Star Candidates	Hummel

Table 8.2: Listing of the scientific programmes that were performed during the period of 'Guaranteed Time Observations' by the 'VLT Instrument Consortium' [34]. The sequence does not reflect a ranking except for programme No. 1 .

The Fors Deep Field No.1 GTO-Programme became therefore the central scientific aim of the VIC consortium. Due to its prominence among the programmes and its scientific interesting questions, it will be discussed in detail in the next chapter.

8.5 '1st-Light' Images

The following pages display a small excerpt of the most impressive images that were taken during the very first observing nights of the VLT with the freshly installed Fors1 imager and spectrograph. It is only a sample of available glossy pictures that were taken during this period of commissioning and observation.

Much more and better reproductions in high resolution and colour can be found in the ESO Press Releases [http://eso.org/outreach/press-rel/] of the years 1998 to 2000. They cover such prominent and appealing objects as the Messier Objects M 1, M 27 and M 83 or the famous 'Sombrero' nebula NGC 4594 and the so-called 'Horsehead' and 'Tarantula' nebula in a superb quality, that was unknown up to that time and which could compete with the marvellous beauty of the 'Hubble Heritage' images, taken with the 'Hubble Space Telescope'.

Figure 8.1: This image that was taken 1998–Sept–15 when the shutter opened for the very first time with the telescope pointing onto the sky. It shows a star field at $0\rlap{.}''64$ seeing located in the constellation Sagittarius (next to the southern edge to constellation Telescopium) at $\alpha=19^h55^m03^s$, $\delta=$-45°00′43″(J2000.0) with the telescope pointing 344°.5 in azimuth and 68°.6 in altitude. With this frame, the ESO-VLT changed into a scientific machine.
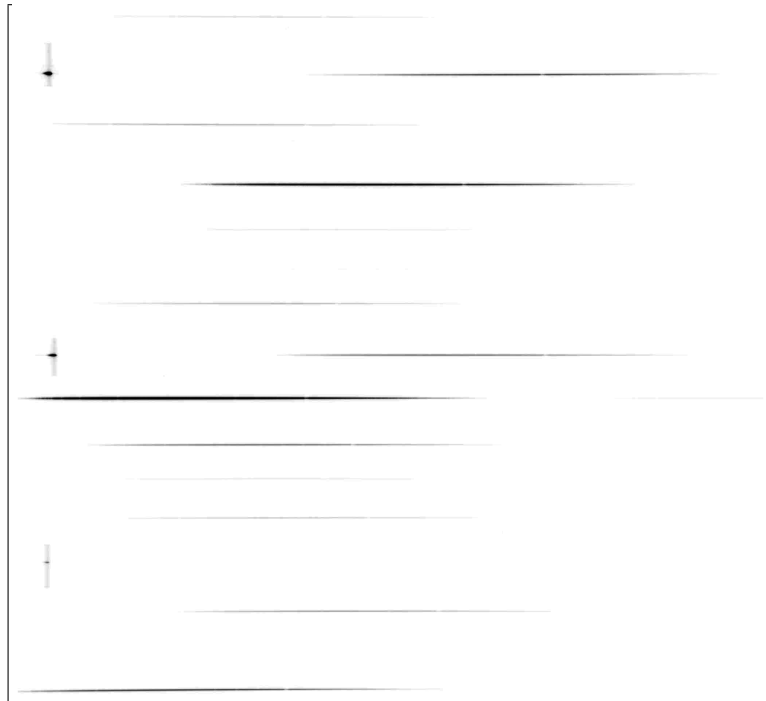
Figure 8.2: The very first Multiple-Object-Spectrograph image was taken on 1998–Sept–20. It clearly shows stellar spectra in 16 of the available 19 slits. The background is filled with spectral lines of the 'glowing' night sky which are much dimmer than the object spectra and exaggerated here to make the field-of-view of the slitlets visible. The field is located in the constellation Reticulum at $\alpha=03^h59^m48^s$, δ=-60°31′56″(J2000.0).
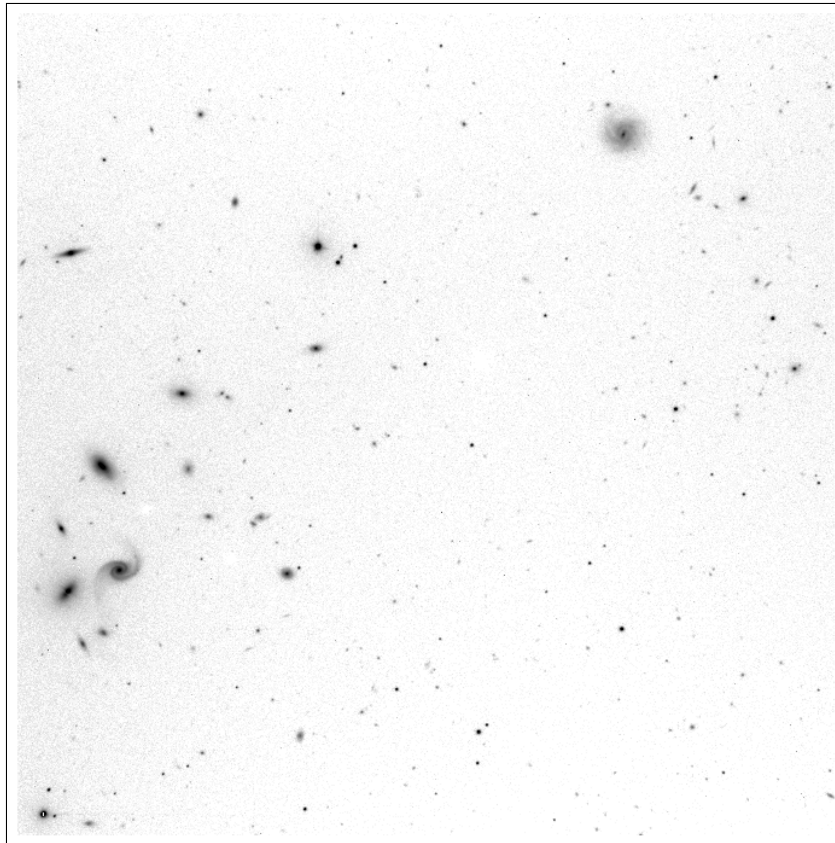
Figure 8.3: After focus check over the total FOV the telescope slewed to an equatorial field at $\alpha=00^h08^m58^s$, $\delta=-00°38'02''$(J2000.0) that contains a galaxy cluster and the known QSO PB5763. Much fainter (field?) galaxies appear in the right part of the field.
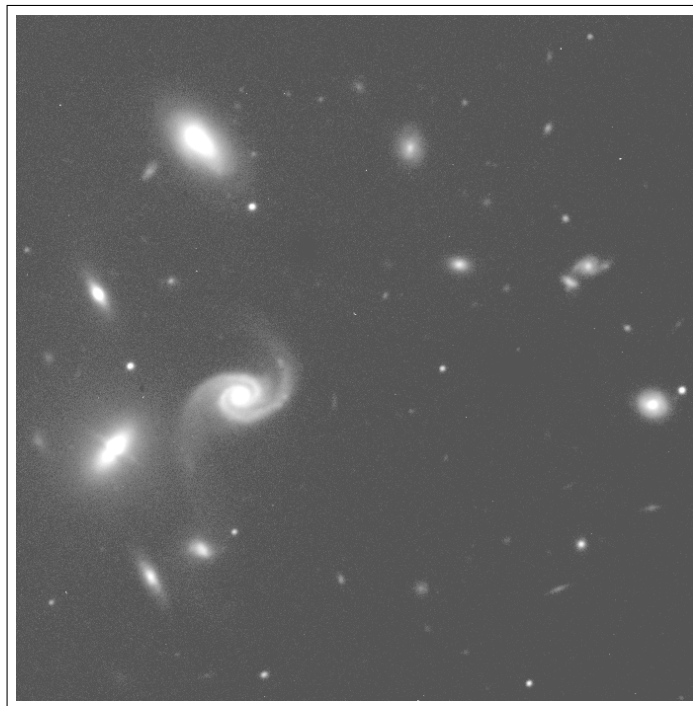
Figure 8.4: A detailed view of the galaxy cluster in the previous figure reveals peculiar shapes of its members. Note the large spiral with its long extensions probably due to tidal interactions. Very strange appears the 'spindle' shaped elliptical galaxy to the left which possess obviously an equatorial ring structure that rotates perpendicular to the main ellipse.
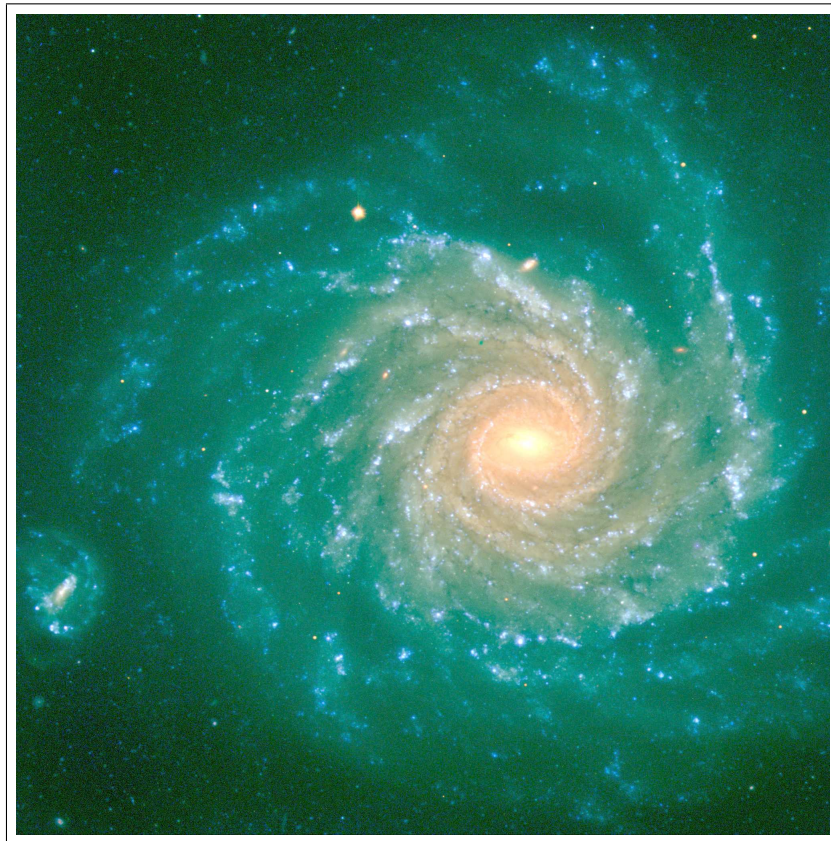
Figure 8.5: NGC 1232, someone call them the FORS GALAXY as it was one of the first images taken with the VLT/FORS combination, is meanwhile reproduced countlessly on posters, calenders, books and covers. It is located in the constellation Eridanus and shows remarkable similarity with the Whirlpool galaxy M51 and its companion.
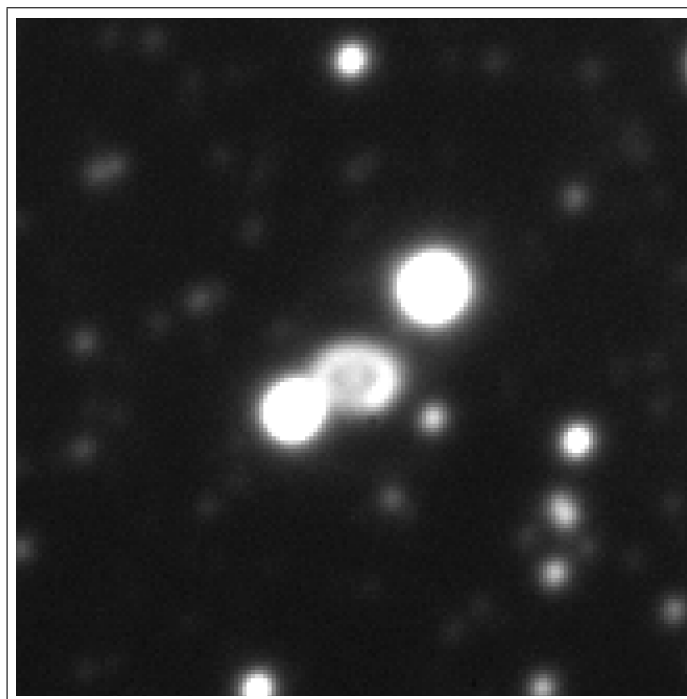

Figure 8.6: Zoom into the image frame that was taken from the famous supernova remnant SN87A in the LMC right at the beginning of commissioning. The material receding from the central compact object is clearly visible.

96

Chapter 9

Science with FORS

9.1 General

The fundamental character of the FORS imager and spectrographs as multi-mode, multi-purpose and multi-functional instruments is clearly emphasized by the attribute of being the VLT workhorse instruments [49], able to cover the broadest observational issues ranging from solar system bodies to the edge of the universe. Within this wide range in observing applications, one dedicated programme, the FORS DEEP FIELD FDF will be outlined in the following chapter, not at least, since I was involved in carrying out this dedicated programme, especially in selecting a suitable located and empty region in the sky as well as in taking the image frames during the commissioning phases for the selection process and later data reduction for scientific use.

Focal reducing instruments such as the FORS twins are most suitable for ultra-deep penetration into space due to their efficient use of light and their relatively low dispersion. Both fit perfectly for the work on very deep fields in the direct imaging as well in the spectroscopic mode. Therefore, the FDF becomes a key programme to be executed in the earliest phase of the guaranteed observing time. Workshops were held several times by the VLT Instrument Consortium to establish it as a key project. This project represents at the best the suitability of the instruments for scientific research.

9.2 The Fors Deep Field

9.2.1 Deep field programmes

Probing the universe quite deeply and statistically goes back to the 30's of the last century. Shapley and Ames provided the first pictures of the distribution of nearby galaxies. The inhomogeneities already observed in this pioneering study were further investigated for instance by Zwicky in the 60's. A big leap was done with the famous CfA-Survey of the 'Center for Astrophysics which covers 2.7 steradian but is still quite shallow with $14^{\mathrm{m}}5$ limiting magnitude although reaching a depth of some $80\,h^{-1}\,\mathrm{Mpc}$ – where h is the Hubble constant H in units of $100\,\mathrm{km\,s^{-1}Mpc^{-1}}$. One of the next deeper probes in a narrow cone was that done by Peterson et

al. [29] in the year 1985. They reached B-magnitudes of around 17 and got photometric redshifts of 329 galaxies. The depth was enlarged by Kirschner, Oemler et al. [30] to about $350\,h^{-1}\,\mathrm{Mpc}$.

The clumpy content of the universe was then probed with very deep pencil beams performed by Broadhurst et al. in 1988 [31] with the Fibre Optic Coupler at the Anglo-Australian Telescope in a spectroscopic survey of about 200 galaxies. Those were contained in five fields of approximately $20'\,\mathrm{x}\,20'$size including the Southern Galactic Pole and led to a galaxy number count per magnitude bin that is considerably steeper than non-evolutionary models predict at 21 magnitude. Therefore, evolution of low-luminosity galaxies could only have occurred over the past 5 Gyr. Shortly after that, Broadhurst et al. were aiming for the vertical structuring of galaxy clusters along the line of sight using pencil beams of small size – typically 40 arcmin in diameter in contrast to the wide area surveys corresponding to some $5\,h^{-1}\,\mathrm{Mpc}$ across at a mean depth of $z \sim 0.2$ – but even deeper penetrating into space. The clustering of the galaxies along the line of sight was explained by a large scale structure which consists of huge empty regions of space, the so-called voids, bounded by 'walls' of enhanced matter density. Each maximum in galaxy density along the line of sight then corresponds to a wall that surrounds a largely empty void. The size of the voids typically equals 125 Mpc. The typical distance along the line of sight between the maximum of the clustering was estimated at about 128 Mpc, which agrees well with the transversal linear scale. The extension of this investigation reached at last a depth of more than $2\,000\,h^{-1}\,\mathrm{Mpc}$. The structuring was observed within four pencil beam fields within $0.4°$of the Galactic poles in the northern and southern hemisphere in 1990 [32]. The reason for choosing that location in the sky will be outlined in the following chapter on the FORS DEEP FIELD selection.

The next logical step was to combine the large but shallow surveys on large scale structuring with the deep surveys of the pencil beams. The FORS DEEP FIELD is not the first attempt to extend the pencil beams by observing so-called 'deep fields' of larger depths and larger widths. Several of them already existed for years. One of the earlier trials is the field that was observed in a seven hour total exposure time by Peterson 1991 [33] with the 3.5 m New Technology Telescope at La Silla. It contained thousands of galaxies within its size of $7\rlap{.}'6$ x $7\rlap{.}'6$ to a depth of 29 mag which showed that more than 97 % of the objects were galaxies. This field was later replaced by the NTT Deep Field (NTTDF) going to a depth of less than 26 mag at a field size of 5.6 sqr.arcmin (cf [35]). It was followed for instance by the William Herschel Deep Field (WHTDP) with much larger field size ($7'\,\mathrm{x}\,7'$) and depth (28.5^{mag}) but only of arcsec seeing quality (cf [38]).

Famous is the Hubble Deep Field (HDF) which is the most prominent of all such attempts. It is based on the imaging performance of the Hubble Space Telescope and was taken with the Wide-Field-Planetary-Camera in about 150 orbits in 1995. Because of the high data quality, two fields – one in the northern (HDF-N) and one in the southern hemisphere (HDF-S) – were observed with the HST. The data of the former field, the HDF-N where published in 1996 [36], the HDF-S followed in 2000 [37]. The HDF-N was by far the deepest look ever made into space, reaching limiting magnitudes of $27\rlap{.}^{\mathrm{m}}6$, $28\rlap{.}^{\mathrm{m}}1$, $28\rlap{.}^{\mathrm{m}}7$ and $28\rlap{.}^{\mathrm{m}}0$ in the passband $\lambda\,300\,\mathrm{nm}$, $\lambda\,450\,\mathrm{nm}$, $\lambda\,606\,\mathrm{nm}$ and $\lambda\,814\,\mathrm{nm}$ of the broad-band filters, respectively. In the meanwhile, the very deep HDF-N was replaced in a follow-up programme by the Ultra-Deep-Field, observed with the Advanced Camera for Surveys of the HST. This new ultra-deep field now penetrates the universe down to a limiting magnitude of 29^{mag} in v and i-band, which is more than 1 magnitude deeper than the Hubble-Deep-Field.

The large advantage of the HDFs is their excellent quality unrivaled by earthbound telescopes,

but they cover a relatively small field of 5.6 square arcmin only. Therefore, their statistics may become affected by two effects, the limited sample size and the structuring of galaxy samples on larger scales. Those possible weaknesses of the HST data could be overcome by a much larger field of comparable deepness. That was one of the primary aims of the FDF that combines the strengths of different predecessor studies. For the first time, it became possible with the VLT to nearly reach the quality of HST images with an earthbound telescope due to the excellence of the site and of the telescope.

9.2.2   The FDF programme

The FORS DEEP FIELD programme was set up to

- reach larger limiting magnitudes than earlier ground-based Deep Field programmes,

- extend the field size covered by the Hubble Space Telescope by a factor of 10,

- improve the statistics of existing Deep Fields,

- explore galaxy evolution,

- constrain current galaxy evolution scenarios – such as hierarchical structure formation in a cold dark matter (CDM) universe,

- to explore the underlying galaxies and the environment of QSOs.

The FORS DEEP FIELD would reach the current space-based limit from the ground. An efficiency calculation demonstrated that FORS would require about 15 hours of total integration time in order to reach objects as faint as 30^m with a signal-to-noise ratio of 5. The FDF programme was aiming for a penetrating depth of $z = 4$–4.5 . It is expected from theoretical models of galaxy evolution programmes that significant imprints from the age of galaxy formation can be detected at the depth of larger than $z = 4$. There was the hope, that these observations could provide the basis to describe the formation of galaxies and clusters in the very early phase of the universe.

The FDF key project should obtain direct images of suited fields in the southern sky. A good candidate would be a field close to the south galactic pole with the advantage of minimum contamination by foreground stars, small galactic extinction and high atmospheric transmission due to a near-zenith transition at the Paranal Observatory. These properties will be outlined in detail in the next section. The direct images would be split into numerous exposures of typical 10 min duration through different broadband filters. The total integration time should amount to 8–16 hours in each filter in order to reach at least 27–28 mag. These images would provide the distribution and density of the galaxies when they were very young, roughly 1 billion years after their formation. Additionally, the knowledge about their distances would be most important. This very crucial information can be obtained with a tricky selection of the broadband filters which allows to derive so-called photometric redshifts. Due to the high redshift z=4–4.5, the Lyman edge of those objects will be shifted into the visible blue spectral range to about 455–501 nm. Putting one filter band-pass on one side of the redshifted Lyman edge and one on the other side will produce a clearly detectable intensity jump in the two corresponding images if the object's distance falls in the window of $z = 4$–4.5 . Adding another image through a third broadband filter will give a very first, zero order spectral information by the generated colour

indices. Further spectral information - even at lowest spectral resolution - is out of the reach of the 4-metre-class telescopes since the FORS spectrographs would require about 8 hours at an 8-metre telescope to get a useful (SNR=10) signal of a 26 mag object at their lowest dispersion of 150Å/mm which is equivalent to a 350 RS-product at 1 arcsec seeing.

The field to be observed with FORS should allow comparison with the corresponding deep field of the Hubble Space Telescope. The latter comprises only about one tenth of the FORS field of view. The HDF-N appears as empty as the SGP field when looked at in the Digital Sky Survey (DSS) on the same scale (Fig. 9.5) and obeys also the other criteria given above for selecting the FORS DEEP FIELD.

A comparison of the FDF with the HDF promised, that one can expect at least a return of the same scientific value from the FDF data set as from the HDF with dozens of publications. But, the FDF will be more than a quantitative step forward through improved statistics of the reddest and oldest object in the universe. From an optimistic point of view and from hints in modelling galaxy evolution, it promised to provide a new quality of insight into the age when galaxies did form. This qualitative step is based on overcoming the current limit in distance and age by an increased depth by about 2 magnitudes.

The FORS DEEP FIELD programme could also contribute to the knowledge of the large scale structuring of the galaxies. Fields of huge size – gigantic compared to that of the FORS instruments – are usually required for that kind of observation. But the lack in sky coverage can be compensated by its depth. This one-dimensional beam along the line of sight could produce data from which the clustering can be investigated as already done and outlined in the preceding section about existing Deep Fields. The FDF data set could confirm the values that are known today, for instance the typical void size of 125 Mpc, or it would deliver different values, hints on evolutionary effects during the age of galaxy formation.

9.2.3 Selection of the Fors Deep Field

Before selecting an appropriate 'empty' field for the deep probing, a catalog of criteria was developed that had to be matched by the field. Table 9.1 lists the reasoning and the specification for the different criteria in order to push the probe as deep as possible with the lowest absorptions, extinctions and contaminations by stars, galaxies or clustering. The different kind of catalogues applied in this evaluation process are given in the lost column.

The search started with selecting a QSO from the Catalog of Veron-Cetty&Veron (1997) fulfilling the following criteria: -32°< δ <-22°, 22h51m< α <02h51m, $z > 2.3$ and $m > 18.5$. Up to 117 QSOs crowded this region. That number reduces to 32 QSOs with a $z > 3$ requirement since host galaxies and environment of quasar closer than this are observable with 4-m class telescopes. Those 32 candidates reduces further to nine with visual inspection of 16 arcmin^2 DSS fields on bright stars, galaxies and field crowding. The avoidance of field contamination – criterium i) – led to four fields that were investigated thoroughly according to criteria a) to h) and j) to o).

Last but not least, the selected field should be comparable in all respects with the Hubble Deep Fields in the North and South for two reasons; the depth of penetration should be equal to compare and evaluate the quality of the gathered data and to estimate any possible deviation from those well investigated deep field probes by much larger samples due to the ten times larger

field size. The pre-selected four fields have the following sky coordinates:

Field No.	QSO-Ident.	Rektasz.	Declination	
F0044	Q 0044–273	$00^h47^m13^s$	$-27°02'02''$	(J2000.0)
F0046	Q 0046–282	$00^h49^m13^s$	$-27°58'24''$	(J2000.0)
F0103	Q 0103–294	$01^h06^m09^s$	$-29°10'28''$	(J2000.0)
F0103b	Q 0103–260	$01^h06^m03^s$	$-25°44'46''$	(J2000.0)

Trial photometry of the brightest objects in the four pre-selected fields was done in a special effort. A comparison of the DSS magnitudes via aperture photometry with HST Guide Star Catalog magnitudes was not successful resulting in deviations of larger than one magnitude. The most reliable estimate of apparent magnitudes turned out from an investigation of the UKSTU Southern Sky Object catalogue based on scans performed on blue-sensitive Schmidt plates using the famous COSMOS machine at the Royal Observatory Edinburgh. It shows that it becomes hard to find a field without stars brighter than 17 mag due to the large size of the Fors 7'x7' field. The last pre-selected field F0103b is an extreme case in this respect. It contains extraordinarily low star counts and brightness, extending also in its surrounding areas. This freedom in fine positioning on the sky allows optimum placing of the QSO and its environment on the detector. Therefore, F0103b appeared as the most promising of all four fields.

Nevertheless, short-term exposures were taken from all four pre-selected fields in order to check on the requesting catalogue items. An inspection of those frames confirmed the results especially those with the highest uncertainty on field contamination through unknown galaxy clustering at higher redshifts. Three fields appeared not optimal due to conspicuous galaxy clusters within the frame, and one of them turned out as to lack a suitable guide star for the active optic system of the VLT. The test exposures confirmed that field F0103b matches all the selection criteria a) to o) in the best possible way. Hence, the decision for the Fors Deep Field fell onto F0103b centred on the coordinates: $\alpha=01^h06^m03^s$ and $\delta=-25°45'46''$ (J2000).

In order to check the properties of the finally selected 'empty' field with the request catalogue, the characteristics of the FDF are listed in Table 9.2. The coordinates of the field centre reflect that it is located very close to the South Galactic Pole and close to the geographic latitude of the Paranal Observatory, the latter causing the field to pass the meridian near zenith. This is an advantageous position for commissioning purposes, for instance instrumental flexure measurements via image motion determination. Therefore, the different commissioning phases of the two instruments could be used in order to take frames for image motion determination which already contained scientifically useful data.

9.2.4 Comparison of Deep Field Candidates

The selected region of the FDF on the sky has to withstand any comparison on emptiness with the other deep fields and for instance competing fields at the Galactic poles. Seven arcmin^2 frames on the Digital Sky Survey (DSS) underline the matching with the selection criteria of Table 9.1, at least partly. For this reason, a sample of frames of the DSS is printed with the exact size of the Fors 7' FOV. Reproduced for comparative inspection are here the FDF (Fig. 9.1), the NTT Deep Field (Fig. 9.2), the South Galactic Pole (Fig. 9.3), the North Galactic Pole (Fig. 9.4) and the Hubble Deep Field – North (Fig. 9.5) and South (Fig. 9.6).

Both Hubble Deep Fields, the Northern and the Southern one, appear fairly unsuited for the

No.	Criterium	Rationale	Specification	Remark
a	Lack of stars	crowding by foreground stars & blooming on CCD	$* > 19^{mag}$ within FOV	DSS, POSS & COSMOS
b	Lack of very bright stars nearby	increased background by sky straylight & internal reflections	$* < 5^{mag}$ outside 5° radius	SIMBAD & HST-GSC
c	Lack of bright extended galaxies	foreground crowding	–	DSS & POSS etc.
d	Lack of strong radio & X-ray sources	indicators for galaxy clusters at medium redshifts	< 1mJy/Sterad at 3.6 cm	FIRST & RASS
e	Lack of known galaxy clusters	foreground crowding & affecting number counts	outside of 1° radius	NASA–NED
f	Lack of unknown galaxy clusters	foreground crowding & affecting number counts	Test observations pre-selected fields	TBC
g	Lack of IR cirrus	Infrared flux	–	IRAS 100μm
h	Low HI column dens.	low absorption in other wavebands e.g.follow-ups	$< 2 \cdot 10^{20} cm^{-2}$	EXSAS cf Lockman1990
i	No field contamination by QSO environment	galaxy excess affecting number counts	–	
j	QSO within FOV	probing the IGM along the line-of-sight& QSO environ.	$z > 3$; within 10° from SGP	Veron-Cetty &Veron 1997
k	Ly$_\alpha$ detection	QSO environment underlying galaxy	detectable in B	
l	High galactic latitude	Galactic extinction far from South Galactic Pole	$E_{B-V} < 0.02^{mag}$ –22°> δ >–32°	NED-NASA Extragal.Dat.
m	Sighting opportunities	atmospheric extinction highly above horizon for long periods	declination close to site latitude –20°> δ >–30°	
n	Early access to observations	data gathering in the commissioning e.g.confirm of image stability on detector	declination close to site latitude –20°> δ >–30°	
o	Comparable to HDF	data evaluation with HDF	–	TBC

Table 9.1: Selection criteria for the FORS DEEP FIELD.

	Item	Property
a	Coordinate field centre	α=01^{h}06^{m}03^s (J2000.0) δ=−25°45′46″(J2000.0)
b	Bright stars $<$ 5^{mag}	none within 5°
c	Radio sources	radio flux $< 2.5\,\mathrm{mJy}$
d	Cluster contamination	none via test exposures
e	IRAS cirrus (100 μm)	IR flux $< 0.035\,\mathrm{Jy}$
f	H I column density	$1.92 \cdot 10^{20} cm^{-2}$
g	E_{B-V}	0.018^{mag}

Table 9.2: Characteristics of the FORS DEEP FIELD.

ten times larger size of the FORS field of view. The Hubble choice is mostly determined by the accessibility of the field within the earth orbit and was driven by other criteria, as the absence of the atmosphere, the zones of avoidance for the sun, and earth obscuration. Even when star density is as low as for the HDF-N, the frame contains at least one 'bright' object. The visual inspection of the displayed frames confirms that the selection of the FDF is properly done, especially through the additional requests of the other criteria in the selection catalogue that are not visible in these DSS frames.
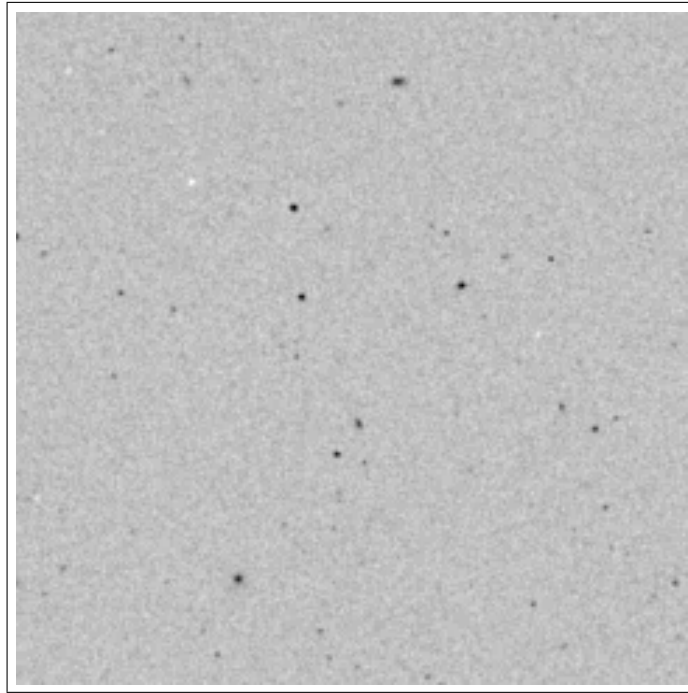
Figure 9.1: 6.8′x6.8′ field on the DSS, centred on the Fors Deep Field at $\alpha=01^h06^m03^s$, $\delta=-25°45'46''$(J2000.0) .
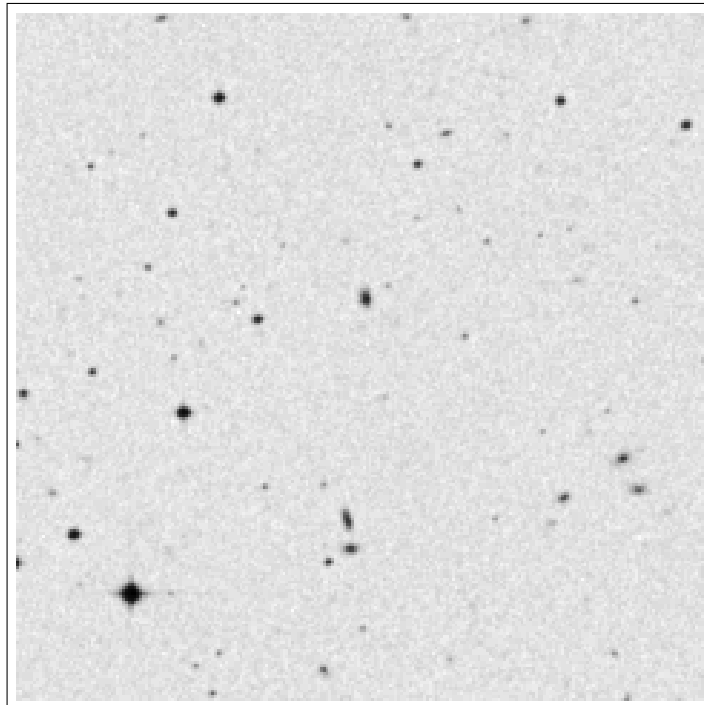
Figure 9.2: 6.8′x6.8′ field on the DSS, centred on the NTT Deep Field at $\alpha=10^h45^m00^s$, $\delta=-00°14'00''$(J2000.0) .

104
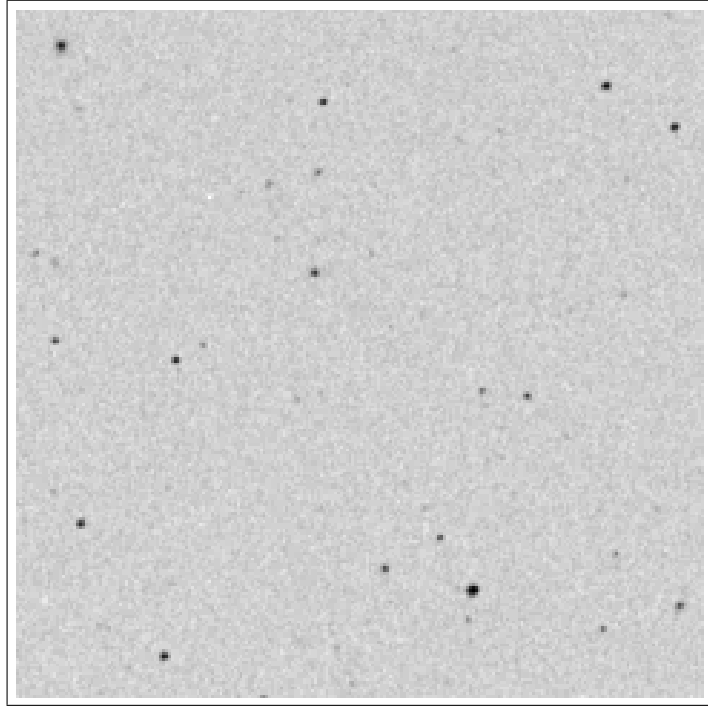
Figure 9.3:   6.8′x6.8′ field on DSS, centred on the Southern Galactic Pole at $\alpha=00^h51^m26^s$, $\delta=-27°07'42''$(J2000.0) .
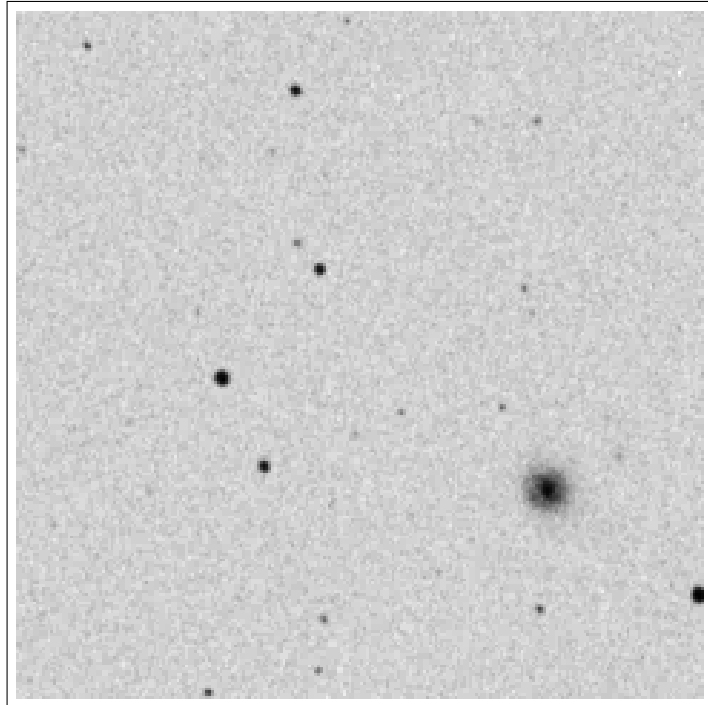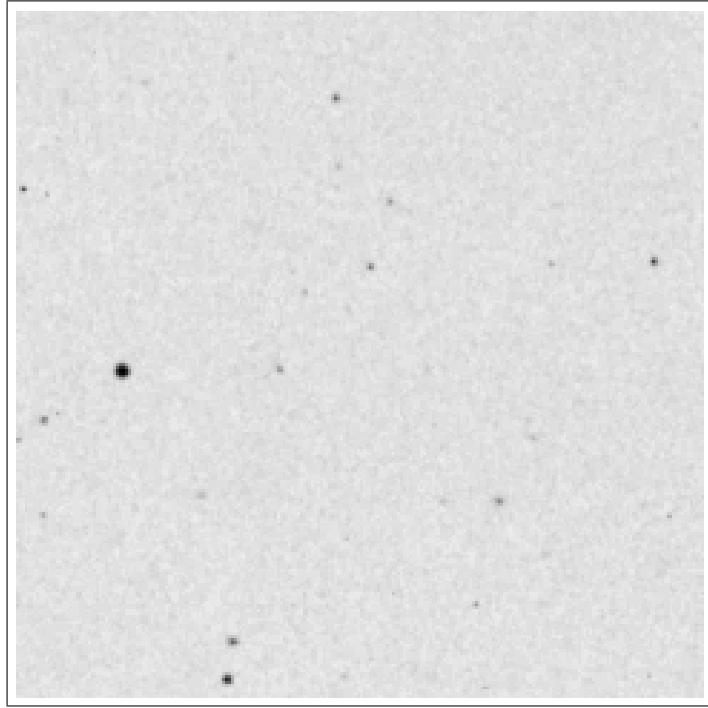

Figure 9.4:   6.8′x6.8′ field on DSS, centred on the Northern Galactic Pole at $\alpha=12^h51^m26^s$, $\delta=+27°07'42''$(J2000.0) .

Figure 9.5: 6.8′x6.8′ field on the DSS, centred on the Hubble Deep Field North – HDF-N at α=12^{h}36^{m}49^s, δ=+62°12′58″(J2000.0) which comprises $\frac{1}{10}$ of that size in the central region.
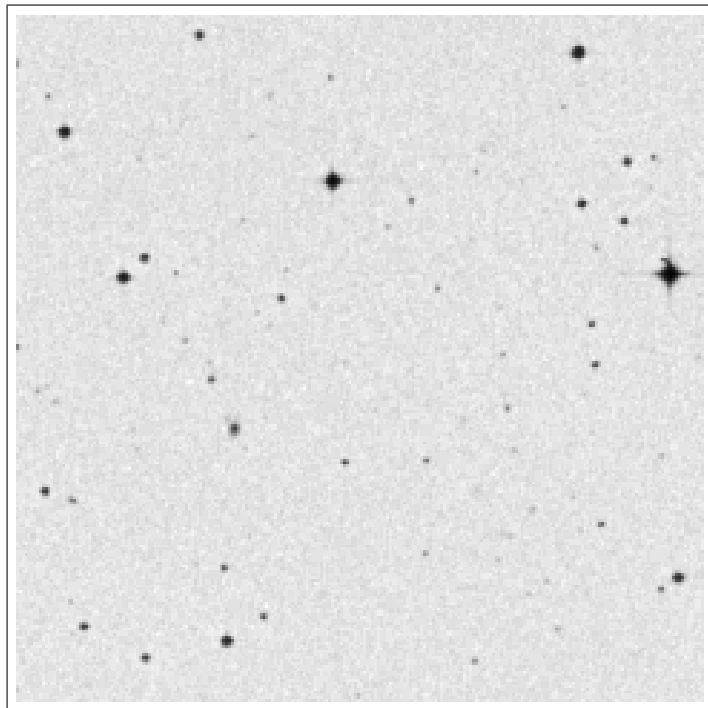
Figure 9.6: 6.8′x6.8′ field on the DSS, centred on the Hubble Deep Field South – HDF-S at α=22^{h}32^{m}56^s, δ=−60°33′02″(J2000.0) which comprises $\frac{1}{10}$ of that size in the central region.

Filter	Photometric system	Expos.time /frame[sec]	Number of frames	Expos.time total[ksec]	Limiting Magnitude	Seeing FWHM
U	Bessel	1 200	37	44.4 ($12^h.3$)	$25^m.64$	$0''.97$
B	Bessel	515	44	22.6 ($6^h.3$)	$27^m.69$	$0''.60$
g	Gunn	515	43	22.1 ($6^h.2$)	$26^m.86$	$0''.87$
R	Bessel	240	110	26.4 ($7^h.3$)	$26^m.68$	$0''.75$
I	Bessel	300	83	24.9 ($6^h.9$)	$26^m.37$	$0''.53$
J	Bessel	4 800	80	4.8 ($1^h.3$)	$23^m.60$	$1''.20$
Ks	Bessel	4 800	80	4.8 ($1^h.3$)	$21^m.57$	$1''.24$
SUM	in total	–	477	150.0 ($41^h.6$)	$<27^m.70$	$<1''.24$

Table 9.3: Characteristics of the Data Set.

9.2.5 Data Reduction and Photometry

The data frames for the FDF programme were obtained in the GTO period. Most of them were obtained in five observing runs (plus one run at the NTT/SofI for the IR data) between August'99 and August'00. In total, 477 frames were taken in 42 hours of integration time which contain 477×8.536 MByte/frame=4 000 MByte of scientific data, not covering all the necessary calibration data files that outnumber this amount.

The limiting magnitudes that could be reached within the total exposure times for each filter are listed in Table 9.3 as well as other characteristics of the data set. In order to get a homogeneous set of data, the reduction of the raw frames was performed in an identical fashion for all five observing runs. First of all, the bias correction took place. Due to the four-port-readout of the CCD, the four overscan regions were used to determine a scaled median level of up to 20 frames to subtract the bias of each port individually.

Flat fielding the frames turned out to be a complex task. Two different kinds of variation had to be compensated for, the pixel-to-pixel difference in sensitivity and a large scale sensitivity variation across the CCD chips. During data reduction it turned out that the twilight flats were not sufficient to correct for the latter variation due to strong gradients within the flat field frames. Therefore, twilight flats were applied to the science frames, which were then grouped according to their large scale variation residuals, normalized, and stacked with a clipped median. Then the correction was applied with two-dimensional 2nd order polynomial fits to each median frame on a grid of 50x50 points with a 40 pixel box width for median values. At the end, reduced frames with 0.2 % peak-to-peak residuals at the maximum resulted from this procedure.

Cosmic ray events had to be removed before source detection started. Two-dimensional Gaussian profile were then fitted to each local maximum in a frame. Signals narrower than 1.5 pixel at FWHM and also larger than eight times the background noise were considered to be produced by cosmic-ray events. Those were removed and replaced by the mean of the surrounding pixels. Bad pixels or regions were flagged out by a bad pixel mask which contained all pixels where a flat field correction of larger than 20 % had to be applied.

Before co-adding multiple frames, image alignment and field distortion corrections were applied to the frames simultaneously. An image taken in the I band in Oct.'99 was used as a reference frame with the position of 25 stars used as reference points. The FORS field distortion was derived once and applied as a correction during the shifting process of each frame. Co-adding the images followed this procedure according to the following steps. The sky contributions had to be estimated for each frame and subtracted. The seeing of each frame was measured for 10 stars as well as the flux of unsaturated stars. This led to a weight factor of the frame during co-adding proportional to the seeing quality. The co-added images had to be calibrated photometrically via 'reference' standard stars. Later it turned out, that the photometry was very stable in 1999 but considerably different in 2000 which was due to the fact that the telescope's efficiency i.e. the reflectivity of its primary dropped and the CCD detector suffered from contamination. Combining these effects led to a loss of 0.3 mag in the achievable depth of the data.

The co-added images obtained that way look similar to the image given in Fig. 9.7 that displays the I band image representative of the other filter bands. The central $6'\mathrm{x}6'$ is shown there that contains up to 6,100 galaxies which are fairly well equally distributed across the field. The only distortion from this equal distribution can be found in the lower right corner where apparently a galaxy cluster (around $z \sim 0.3$) appears. The quasar Q0103–260 already mentioned in the field selection process can be seen at about 7 o'clock near the centre, marked with an arrow. The brightest object within the field is the elliptical galaxy at the lower left with $16\overset{\mathrm{m}}{.}5$ at $z \sim 0.2$. The characteristics of all co-added images are summarized in Table 9.3.

For the photometry and the source detection, the so-called SExtractor from Bertin and Arnouts [39] was used. The source detection is dominated by three parameters:

- the threshold which determines the minimum signal-to-noise ratio for detecting a single pixel,

- the number of contiguous pixels that must exceed this threshold   and

- the filtering prior to detection, in our case a Gaussian filter, characterized only by its width.

These three parameters had to be optimized in order to maximize the numbers of detected objects and to minimize false detections. After a laborious procedure which is described in every detail in [84], the following parameters were found as optimal: a threshold of SNR=1.7, 3 consecutive pixel with a Gaussian filter width of 2 pixel. These parameters led to an almost perfectly symmetric distribution in the pixel-value histogram that stands for flat sky without objects representing photon-noise and correlated noise of co-adding and data reduction. The same parameters were used for all filter bands. The photometric accuracy was estimated to be better than 5σ leading to an optimal extraction above noise-level with quite small false detections. It has to be pointed out that the detection parameters were chosen in such a way, that the number of *real* detections was optimized for reliable photometry and photometric redshifts at the cost of the maximum in galaxy number counts at the faint limit.
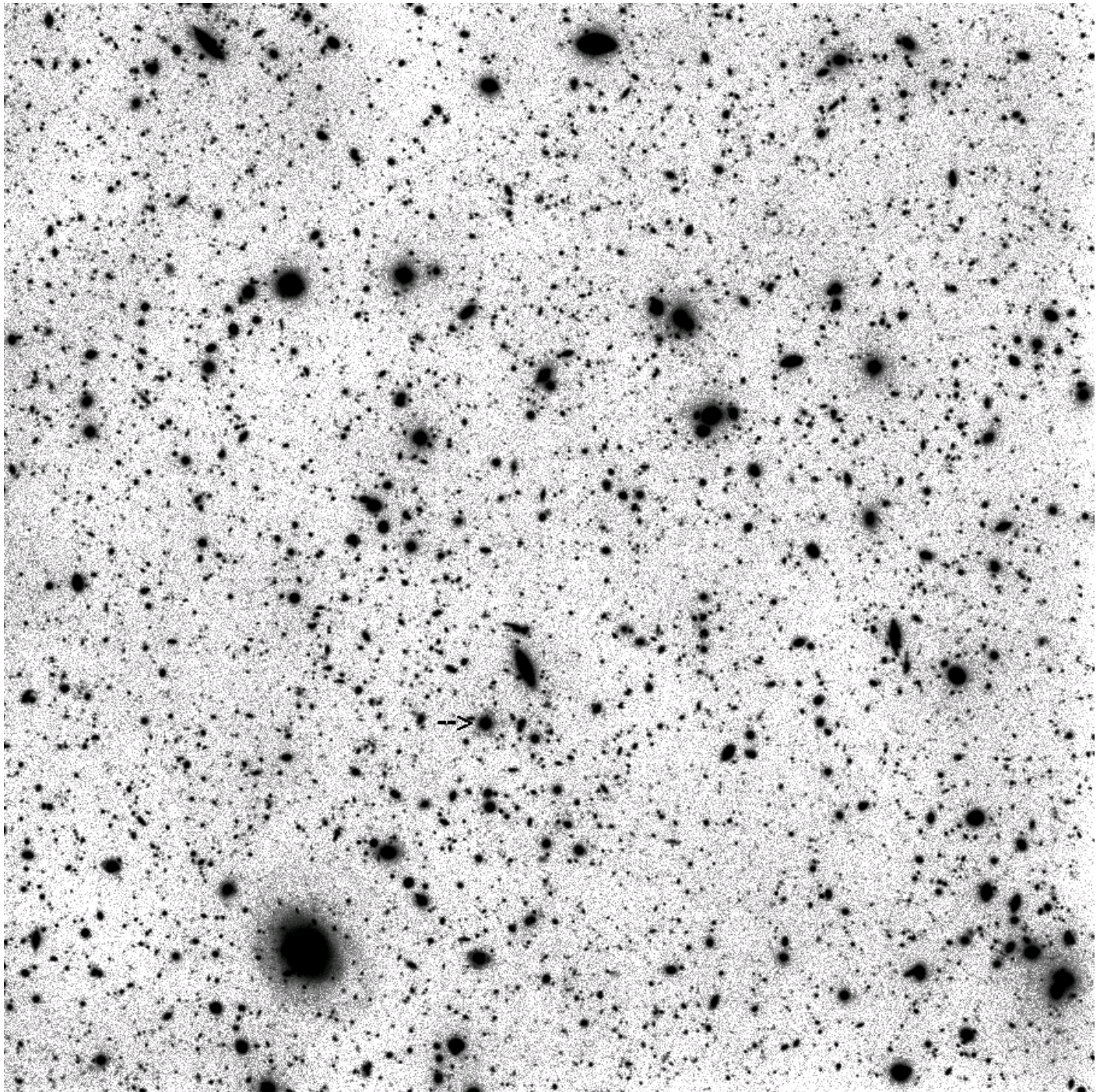
Figure 9.7: The FORS DEEP FIELD in the I-band. It shows only the 'central' part of the image common to all of the input frames corresponding to 6′x6′. It covers at least 6 100 galaxies and the QSO Q0103–260 south of the center, marked by an arrow. The integration time totals 7 hours and results in a limiting magnitude of about 27^m. North is up and east is to the left.
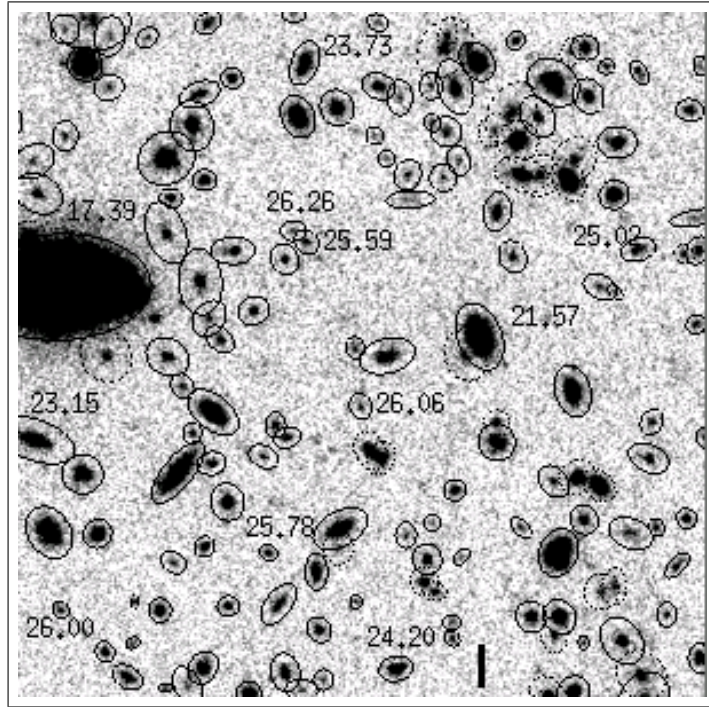
Figure 9.8: Image returned from the extracting software. The $1'$x$1'$sub-picture demonstrates the quality of source detection and photometry. The numbers attached to some sources represent integrated magnitudes. Dashed contour lines denote blended objects.

9.2.6 Scientific Output

Photometric Catalogue

One of the numerous scientific outputs of the FORS DEEP FIELD is a photometric catalogue of some 9 000 objects. Additional to the printing [85], the photometric catalogue was also published electronically and can be obtained via an anonymous ftp-account at the `cdsarc.u-strasbg.fr` or via the web-site `http://cdsweb.u-strasbg.fr/cgi-bin/qcat?J/A+A/398/49`.

The final catalogue was created by merging the two catalogues that were obtained with SExtractor from the reduced filter frames in the B and in the I band. Both finally reduced frames exhibit the best seeing conditions and offer the highest chance that most types of objects were detected in at least one of these two filter bands. Both, the B and the I catalogue contained initially 7 206 and 6 900 objects, respectively. Merging these two catalogues led to a final catalogue of 8 753 objects in total. The overwhelming part of them (5 327 objects or 61 %) were detected in both, the B and the I band. Out of the total of 8 753, 1 864 (21 %) and 1 562 objects (18 %) could be detected only either in the B or in the I band, respectively.

Total as well as aperture magnitudes were derived for the 8 753 objects in the available filter bands $UBgRIJKs$. The aperture chosen was 2 arcsec to minimize errors due to blending and final object size. Apart from the seven aperture magnitudes and the two total magnitudes in B and I, the final catalogue delivers for each object the celestial position (RA,Dec) in J2000.0 coordinates with an accuracy better than 0.5 arcsec. A Gaussian fit to the core delivers the FWHM together with an elongation ratio and position angle relative to the north. Finally,

110

different flags indicate blending, single catalogue detection and preliminary classification.

The galactic absorption could also be estimated from the photometry. The values for the $UBgRIJKs$ filter bands were calculated to 0.087, 0.076, 0.062, 0.041, 0.035, 0.016 and 0.007 magnitudes respectively. They agree well within 0.01 mag with the data obtained so far from the NASA Extragalactic Database NED already mentioned as a selection criterion in Table 9.1. The finally published catalogue was not corrected for it, but the derived galaxy number counts, however, were corrected for the galactic extinction.

Galaxy Number Counts

Galaxy number counts were performed as a quick check for the photometric quality and depth because they were already done several times for earlier deep fields and nothing surprisingly new was expected from our data. Therefore, not much effort was put into separating stars and galaxies accurately since the galaxies will outnumber them anyway at the faint end. At the bright end, the automatic routine of SExtractor was able to disentangle the profile of stars and galaxies. The incompleteness at the faint end was also not corrected. But a 50 % completeness limit was estimated and drawn into the graphs of which only the Galaxy number counts in the B-band will be given as an example in Fig. 9.9.
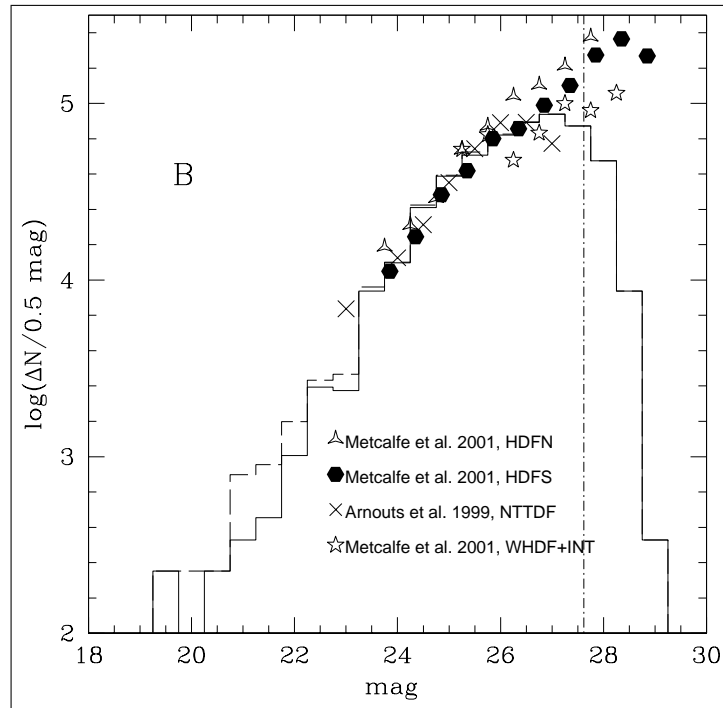
Figure 9.9: Galaxy number count of the FORS DEEP FIELD in the B-band (solid histogram) in comparison to other number counts of Deep Fields, especially the Hubble Deep Field in the North and in the South. The data agree very well with earlier results which indicates a good and precise photometry of the FDF. The vertical dash-dotted line indicates a 50 % completeness limit at 27.7 mag. The dashed histogram shows the total counts, not corrected for obvious stellar objects. Galaxy number counts in the other filter bands U,g,R,I,J and K can be found in [84].

Photometric Redshifts

Photometric redshifts are a combination of photometry with a redshift measurement [78]. This is a powerful tool to obtain a three-dimensional image of the galaxy distribution up to the outskirts of the universe which can be reached by today's telescope and instrument technology. Such redshifts can also provide peculiar velocities of galaxies that depart from the Hubble flow and add information on the galaxy luminosity function.

From the FORS DEEP FIELD catalogue, the photometric redshifts of roughly 6 300 objects could be obtained [88]. The distribution of the galaxy number as a function of distance shows an increase in density at the redshift of $z = 3.3$–3.5 in the histogram of Fig. 9.10. Spectroscopic follow-up observations have been made for more than 400 galaxies of them in order to confirm the method of obtaining photometric redshifts with automatic routines and to pin down more exactly the redshifts of a few specific candidates. Most of the 400 candidates were above $z = 1$ with up to $z = 5$. The Mask Exchange Unit (MXU) of FORS2 came into use during this programme since it provides highest efficiency in Multi Object Spectroscopy with more than a hundred spectra in a single shot.

The spectral resolution of 5 was quite low but sufficient for the study of continuum and absorption features at a $SNR > 10$. The redshift of about 250 galaxies could be derived safely from those spectroscopies. They reflect exactly the redshift distribution of the photometric method as given in Fig. 9.10. They perfectly confirm the method of photometric redshift with the applied routines.

A few of the specific candidates for reliable redshifts by spectroscopy were the galaxies in the vicinity of the QSO. They could be obtained as well and are discussed in the following.
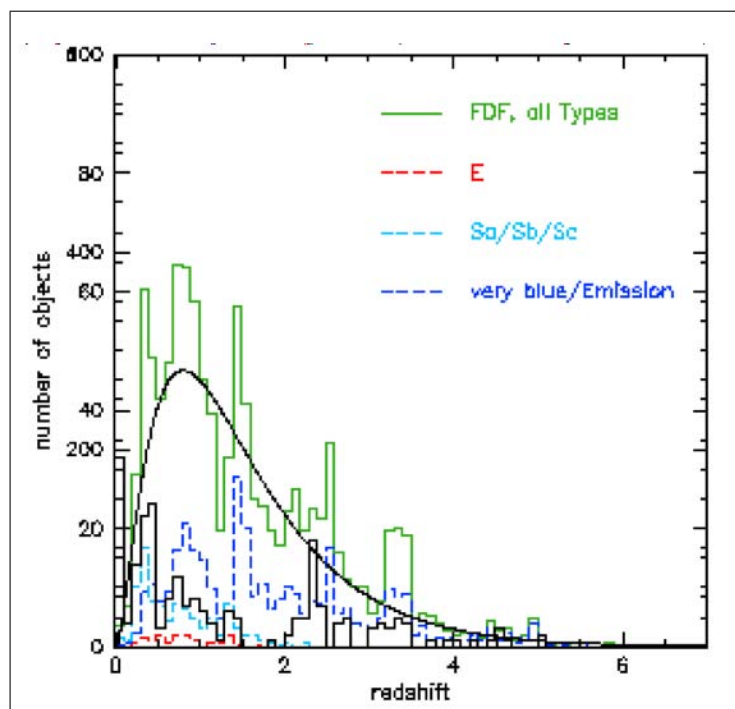

Figure 9.10: The distribution of the photometric redshifts of roughly 6 300 galaxies, obtained within the FORS DEEP FIELD, taken from [88].

9.3 The Quasar Q0103–260 in the FDF

The FORS DEEP FIELD allows also the investigation of a quasar and its environment at extremely large distance [88]. The QSO Q0103–260 is located at a distance of z=3.365 and was observed with a red-shifted Lyman α narrow-band filter at 530 nm. In this narrow-band image, at least three accompanying galaxies could be fairly well identified only a few arcseconds away from the QSO, which were not detected in a second narrow-band filter at 485 nm. Two of them are also faintly visible in the broad I-band image (Fig. 9.11) south- and north-west of the QSO with photometric redshifts of 3.08 and 3.06. Given a 10 % photometric distance error, the values are close to the redshift 3.365 of the QSO, which appears to be surrounded by a small group of galaxies with at least these three members. A spectroscopic follow-up of the three galaxies and of other candidates could confirm the physical association of the faint companions at redshifts of 3.368 (north-west), 3.374 (south-west) and 3.302 (south-east) with the QSO. Seven other candidates could be measured in a redshift interval 3.36–3.40 with less than 0.005 redshift errors. The results suggest that the QSO may be part of a (proto?)-cluster at z = 3.365 . In the meanwhile, VLA observations of the FORS DEEP FIELD have been carried out that show low-level radio emission of about 1 mJy at 5 GHz which confirm that radio emitters can be found in regions of high galaxy density in the young universe.
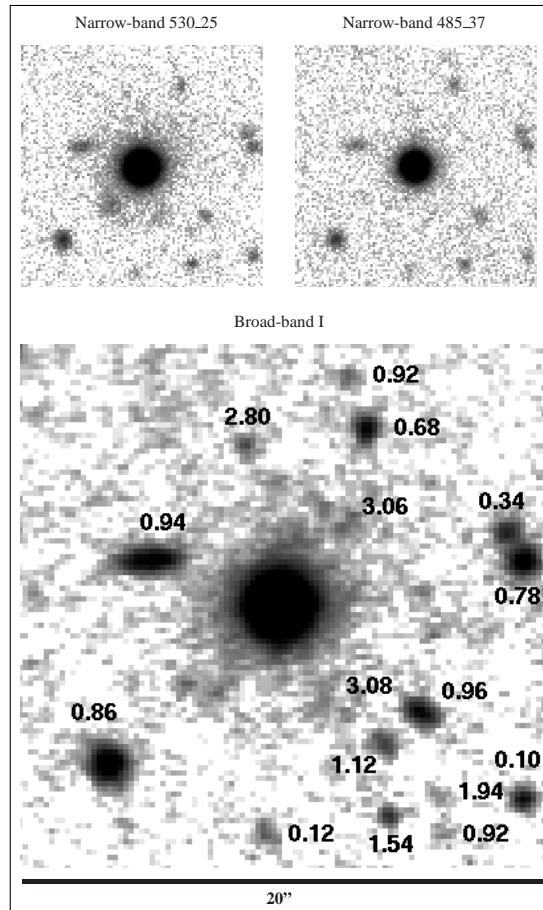

Figure 9.11: The I-band image of QSO Q0103–260, taken from [88], shows the close environment of the quasar at z=3.365 in the FORS DEEP FIELD and the surrounding galaxies with their photometric redshifts. At least three companions could be found by follow-up spectroscopy.

9.4   Scientific potentials

An example from the other extreme end of observation is for instance the use of FORS in detecting very dim objects of the solar system, the Trans-Neptunian-Objects (TNOs). The deep images taken with FORS are well suited for this kind of investigation. Searching for TNOs does not require separate observing time but is a spin-off from existing programmes such as the FORS DEEP FIELD with its deep image frames, not only showing faintest galaxies at the cutting edge of our current observing technology but also this type of nearby objects. They are believed to populate the ecliptic plane outside of the orbit of Neptune and the Kuiper Belt. TNOs are very dim objects due to their small size and to their large solar distance. The original observing plan could not be realized but part of the observing time at the 'Science Verification' phase and GTO was spend to investigate these fast moving objects. The FORS instruments were used to detect them with direct imaging and to spectroscopy them directly afterwards [75]. Five spectra could be recorded for the first time with FORS.

On the other hand, the FORS instruments did demonstrate their suitability for observational cosmology. They were used already during commissioning to detect the cosmic shear which is also known as weak lensing. Due to general relativity, high mass concentrations can deflect the light of background galaxies, that appear close to that gravitational lens, into multiple or highly stretched images such as giant arcs around galaxy clusters, also known as strong lensing. If the background galaxy is located far away from the gravitational lens, its image will only slightly distorted and thus produces only a weak signal. This weak lensing effect can be used to probe directly the gravitational field of any mass distribution, even that of the large scale structure of the universe itself. The light rays of very distant galaxies are continuously deflected while travelling through space with inhomogeneous mass distribution leading to distorted images of those galaxies, called the cosmic shear. This distortion is a tiny effect, but it can be observed as an uneven distribution in the ellipticity of those background galaxies.

Since cosmic shear produces such a weak signal, it demands excellent instrument performances for its detection which requires a very clean and stable instrument profile of the point-spread-function. This profile is controlled via stellar images in the field of view as perfectly circular calibration sources that will be subtracted from the elliptically deformed galaxies. Their intrinsic elliptical shape adds complexity to the task. Nevertheless, the quality of the mass detection threshold and distribution depends strongly on the instrument profile. The design and realization of the two FORS instruments turned out in the real observational test that they are perfectly suited in this respect. They showed a very high imaging fidelity and additionally an outstanding stability of their PSF throughout the observing campaign [41]. Both are the merit – beside the optical parameters – of positioning the optics with high accuracy and stability through the instrument mechanics. The VLT/FORS combination produced an unprecedented high quality and homogeneous data set in cosmic shear detection so far [40].

These instruments delivers astronomers new and powerful tools for observational cosmology with cosmic shear. This kind of astrophysics enables us to probe directly the structuring of the 'Dark Matter' without making any assumptions about its nature and relation to the luminous matter. Mapping the image of distant sources very accurately after a roller coasting travel of their light rays through the curved space-time opens the opportunity to detect the invisible and still unknown content of 'Dark Matter' in our universe. Newest observation of the cosmic shear on scales of $0.'5-50'$ argue for a constraint of $\Omega_m = 0.3 \pm 0.06$ in the mass density of the baryonic content of the universe.

I expect that I could demonstrate with these examples that the FORS instruments support or even enable very widespread application of astronomical observations that ranges from the nearest objects in the solar system to the most remote objects at the edge of our known universe. Both instruments will be extremely suitable to tackle a broad range of astrophysical issues.

Chapter 10

Conclusion and Perspectives

Instrumental development has entered a new era in designing postfocus instruments for the next generation telescopes of the 8–10 metre class. To the first order, the size of the instrument optics and the mechanical dimensions scale with the linear size of the feeding telescope. Adaptive optics now open up new possibilities to depart from that scaling law with a smaller-sized entrance angle than the natural seeing disk.

Building the two FORS as competing imager and spectrographs was a very ambitious project for a consortium of three university institutes in order to provide the workhorses for the 16-metre 'Very Large Telescope'. To justify that naming, the instruments had to bear a high functionality in very different observing modes. The technical goals were set very high, thus leading to large efforts in designing, constructing, testing and installing the instruments at the observatory, lasting in total more than 10 years and consuming financially more than 180 man-years and 2.3 Million EURO for hardware costs thus totaling to approximately 12 MEUR. It was demonstrated in the course of the project that all technical and scientific specifications were met well within their limits, first at the telescope and star simulator, later under real observing conditions at the VLT unit telescope. The observing statistics confirm for the time being that the majority of the scheduled observations were carried out with them and that the European Astronomical Community can rely upon that two focal reducing instruments.

The sharpness of the image, a result of its stability on the detector, is one the most important instrumental parameters in order to maintain the telescope imaging quality with its active optics. This demand was achieved at highest level. The *passive* flexure compensation beating image motion and wandering on the detector could be tuned for each single optical train as low as tenths of a pixel per 24 hours. Due to the fact that two imaging scales with separate collimating optics are offered to the observer a compromise between standard and high-resolution imaging stability had to be installed. Both optical trains use different collimating focal length which behaves diametrically in compensation. Optimum compensation could be achieved by identifying the correct stiffening set-up for which both imaging modes show the least diameter in image wandering simultaneously. With this optimization, the specification of maximal $\frac{1}{4}$ pixel per 0.5–1^h in the standard and maximal $\frac{1}{4}$ pixel per 2^h in the high resolution imaging mode could be achieved. All these achievements were obtained at the telescope and star simulator in the integration hall. It turned out during commissioning at the telescope that this high degree of image stability became undetectable at the real sky since this small scale image motion was totally covered by the noise of seeing and tracking uncertainties.

One competing project, the Low Resolution Imager and Spectrograph (LRIS) of *Caltech's* 10 m Keck telescope for instance, was not that successful in this respect. The image stability on the detector turned out reciprocal to its specification. Instead of the $\frac{1}{3}$ pixel goal, only 6 pixel stability [7] were reached by its designers. Several sources of instrumental flexure were identified after commissioning at the telescope. The major contributions come from central structural parts (spectrograph body, grating turret and telescope flange module) with the consequence that a replacement of those parts will effectively equal a major re-construction and the procurement of a new instrument.

Another instrumental highlight of the FORS project became the multiple object spectroscopy with either movable slitlets or the additional mask exchanger. Both masking units perform well within their design goals which specify the slit quality to about $10\,\mu$m in width variation whereas the stability in slit parallelism is demanded as high as $2.5\,\mu$m/edge. This covers only a few aspects of the project. In total, the FORS project can be regarded as a project of great success for the three participating university institutes, for the German 'Verbundforschung Astronomie', who financed the project to 70 % amount, and for the European Southern Observatory and its astronomical community.

For the future, the FORS spectrographs probably could be one of the last instruments of the large telescope era that was built with a *passive* instrumental flexure compensation. Numerous proposals and design concepts already exist that will utilize *active* compensation mechanisms against instrumental flexure (e.g. [25], [26], [27], [28]). Those active flexure compensation are becoming integral part of the instrument design and depend on closed-loop control. The concepts differ mainly by the parts that will be actively moved – beam optics or the detector directly – and by the kind of sensing system, sensor type and wavelength. Except for the issues in its technical realization, one has to consider carefully the possible cross-talk and/or additional straylight and contamination, introduced into the optical beam and electronic systems. This will raise new uncertainties in the reliability of the overall system because these instruments totally rely on the active function to reach their performance specification. In contrary, a passive compensation will not fail, once it is established in the design and adjusted during hardware initialization.

On the other hand, in view of the giant telescopes with 30–100m aperture which already appear at the horizon, active instrument systems seem to be the only solution in order to meet the demands on future instruments. Actuating the instrument mechanics and optics opens new degrees of freedom in design, compensation and stability therefore surpassing passive ones. But first a running system as well as field tests on the robustness in the harsh environment of a telescope will reveal how long it takes that active compensation becomes state of the art for instruments. All signs indicate that instrument builders are standing now at the edge where telescope builders have been two decades ago. As a logical step further in instrumental techniques, we are currently entering the transition phase where the passive instruments will turn into active ones as it already took place for the telescope optics. This leap in instrument technique appears as mandatory as it does the adaptive optics for the next generation of giant telescopes. Both have to become integral part, on instrument and on telescope side, which otherwise would become useless.

Bibliography

Reference Publication List

[1] A.B. Meinel: Astrophys. Journal **124**, 652, 1956

[2] R. Florence: The perfect machine – Building the Palomar telescope, HarperCollins, 1994

[3] H. Nyquist: AIEE Trans. **47**, 617, 1928

[4] C.J. Shannon: Proc. I.R.E. **37**, 10, 1949

[5] W.H. Press, B.P. Flannery, S.A. Teukolsky, W.T. Vetterling: Numerical Recipies, Cambridge University Press, p. 500, 1989

[6] J.R. Walsh, I.J. Danziger: Science with the VLT, Springer, Berlin 1995

[7] J.B. Oke, J.G. Cohen, M. Carr, J. Cromer, A. Dingizian, F.H. Harris, S. Labrecque, R. Lucinio, W. Schaal, H. Epps, J. Miller: The Keck Low-Resolution Imaging Spectrometer, PASP **107**, 375, 1995

[8] T. Sasaki, : Iye, T. Yamashita, N. Kashikawa, K. Ohta, M. Yoshida, G. Kosugi, T. Yamada, Y. Yadoumaru, T. Ozawa: Capability of Multiobject Spectroscopy over Optical to Infrared Wavelength with FOCAS for the Subaru Telescope, in 'Scientific and Engineering Frontiers of 8-10m Telescopes', Eds. M. Iye, T. Nishimura, Universal Academic Press, Tokyo, 1995

[9] K. Bahner: Teleskope, Handbuch d. Physik **XXIX**, 227, Springer 1967

[10] K. Schwarzschild: Untersuchungen zur geometrischen Optik I, II & III, Abhandlungen Königl. Gesell. d. Wissenschaft zu Göttingen, Band **IV**, No.1, 1905

[11] R.N. Wilson: Reflecting Telescope Optics I, Sect.4.5.2, p.392-402, Springer, 1999

[12] W. Seifert, R. Östreicher: An optical study of the UV-Visual Focal Reducer/Low Dispersion Spectrograph for the ESO-VLT, Tech. Report, Landessternwarte Heidelberg, Oct. 1990.

[13] M. Born, E. Wolf: Principles of Optics – Electromagnetic theory of propagation, interference and diffraction of light, Pergamon Press, 1959

[14] R.N. Wilson: Reflecting Telescope Optics I & II, Springer, 1999

[15] L. Noethe: Active optics in modern, large optical telescopes, in 'Progress in Optics' Ed. E. Wolf, Vol.**43**, 2002

[16] P. Dierickx: VLT Optics: design of telescope optics, ESO-Report, VLT-TRE-ESO-10000-0526, 1994 and VLT-TRE-ESO-10000-0587, 1995

[17] P. Dierickx: J. Mod. Opt. **39**(3), 569, 1992

[18] F. Roddier: The effects of atmospheric turbulence in optical astronomy, in 'Progress in Optics' Ed. E. Wolf, Vol.**XIX**, 281, 1981

[19] W.B. Wetherell: The calculation of image quality, Applied Optics and Optical Engineering, Vol.**VIII**, 171, Academic Press, 1980

[20] W. Beitz, K.H. Küttner: Dubbel, Para. 2.4.8, Springer, Berlin 1995

[21] H.R. Schwarz: Methode der finiten Elemente, Teubner, Stuttgart 1984.

[22] K.-J. Bathe: Finite-Elemente-Methoden, Springer, New York 1990.

[23] E. Brunetto: Cassegrain Adaptor-Rotators FE Analysis Report, ESO Technical Report No. VLT-TRE-ESO-11410-1279, 1997

[24] M. Serrurier: Structural features of the 200-inch telescope for Mt. Palomar Observatory, Civil Engineering, p.524, August 1938

[25] B.M. Sutin: ESI - a new spectrograph for the Keck II telescope, in 'Optical telescopes of today and tomorrow', A. Ardeberg (Ed.), SPIE Proc. **2871**, 1116, 1997.

[26] R.L. Davies et al.: GMOS - The GEMINI Multiple Object Spectrographs, in 'Optical telescopes of today and tomorrow', A. Ardeberg (Ed.), SPIE Proc. **2871**, 1099, 1997.

[27] P. Hastings: Focus and translation mechanism for the Gemini Multi-Object Spectrograph, in 'Optical telescopes of today and tomorrow', A. Ardeberg(Ed.), SPIE Proc. **2871**, 1216, 1997.

[28] P.D. Arrigo et al.: Active compensation of flexure on the High-Resolution Optical Spectrograph for Gemini, in 'Optical telescopes of today and tomorrow', A. Ardeberg (Ed.), SPIE Proc. **2871**, 1306, 1997.

[29] B.A. Peterson, R.S. Ellis, G. Efstathiou, T. Shanks, A.J. Bean, R. Fong, Z. Zen-Long: A complete galaxy redshift sample. III - Methods and catalogue, MNRAS **221**, 233, 1986

[30] R.P. Kirshner, A. Oemler, P.L. Schechter, S.A. Shectman: A deep survey of galaxies, Astron. Journal **88**, 1285, 1983

[31] T.J. Broadhurst, R.S. Ellis, T. Shanks: The Durham/Anglo-Australian Telescope faint galaxy redshift survey, MNRAS **235**, 827, 1988

[32] T.J. Broadhurst, R.S. Ellis, D.C. Koo, A.S. Szalay: Large-scale distribution of galaxies at the Galactic poles, Nature **343**, 726, 1990

[33] B.A. Peterson, S. D'Odorico, M. Tarenghi, E.J. Wampler: The NTT provides the deepest look into space, The ESO Messenger No.**64**, 1, 1991

[34] Proposals for FORS and FORS2 Garanteed Time Observations, http://www.eso.org/ observing/ proposals/ gto/ fors1/

[35] S. Arnouts, S. D'Odorico, S. Christiani et al.: The NTT SUSI deep field, Astron. & Astrophys. **341**, 641, 1999.

[36] R.E. Williams, B. Blacker, M. Dickinson et al.: The Hubble Deep Field Observations, Astron. Journal **112**, 1335, 1996.

[37] R.E. Williams, S. Baum, L. Bergeron et al.: The Hubble Deep Field South: Formulation of the Observing Campaign, Astron. Journal **120**, 2735, 2000.

[38] N. Metcalfe, T. Shanks, A. Campos, H.J. McCracken, R. Fong: Galaxy number counts - V. Ultradeep counts: the Herschel and Hubble Deep Fields, MNRAS **323**, 795, 2001.

[39] E. Bertin, S. Arnouts: SExtractor: Software for source extraction, Astron. & Astrophys. Suppl. **117**, 393, 1996.

[40] R. Maoli, L. van Waerbeke, Y. Mellier, P. Schneider, B. Jain, F. Bernardeau, T. Erben, B. Fort: Cosmic shear analysis in 50 uncorrelated VLT fields. Implications for Ω_0, σ_8, Astron. & Astrophys. **368**, 766, 2001.

[41] Y. Mellier: private communication

Related Personal Publication List – ordered by years

[42] H. Nicklas, K.J. Fricke: Wissenschaftlich-Technisches Konzept eines 12-Meter Teleskopes für den optisch/infraroten Spektralbereich, Report to Federal and Lower-Saxony Administration, 65 pages plus 140 p. Annex, Universitäts-Sternwarte Göttingen, June 1991.

[43] I. Appenzeller, K. Fricke, R.-P. Kudritzki, B. Muschielok, H. Nicklas, R. Östreicher, W. Seifert: F O R S – Proposal, Technical Report of the 'VLT-Instrument- Consortium' as a *Proposal* for building two Focal Reducer/Spectrographs for the 16-m Very Large Telescope of the 'European Southern Observatory ESO', 211 pages; Göttingen, Heidelberg, München, Feb. 1991

[44] I. Appenzeller, K.H Duensing, K. Fricke, S. Gong, H.-J. Hess, S. Kiesewetter, R.-P. Kudritzki, S. Möhler, B. Muschielok, H. Nicklas, R. Östreicher, M. Roth, G. Rupprecht, W. Seifert, O. Stahl: FORS – A Multi-Purpose Instrument for the ESO VLT, ESO Conf.& Work. Proceedings No. **42**, 577, 1992

[45] I. Appenzeller, F. Fricke, W. Fürtig, S. Gong, A. Hebenstreit, R.-P. Kudritzki, W. Mitsch, S. Möhler, B. Muschielok, H. Nicklas, R. Östreicher, W. Seifert: F O R S – Preliminary Design Report, Technical Report of the 'VLT-Instrument- Consortium' on the *Preliminary Design* of the two Focal Reducer/Spectrographs for the 16-m Very Large Telescope of the 'European Southern Observatory ESO', 288 pages; Göttingen, Heidelberg, München, March 1992

[46] K.H. Duensing, R. Harke, H. Nicklas, H. Renziehausen, H. Böhnhardt, H.-J. Hess, S. Kiesewetter, W. Mitsch: Prototype for the FORS Multiple-Object Spectroscopy Unit under Test, ESO Messenger No. **71**, 43, 1993

[47] I. Appenzeller, H. Böhnhardt, K. Fricke, W. Fürtig, S. Gong, A. Hebenstreit, S. Kiesewetter, R.-P. Kudritzki, W. Mitsch, S. Möhler, B. Muschielok, H. Nicklas, R. Östreicher, W. Seifert, O. Stahl: F O R S – Final Design Report, Technical Report of the 'VLT-Instrument- Consortium' on the *Final Design* of the two Focal Reducer/Spectrographs for the 16-m Very Large Telescope of the 'European Southern Observatory ESO', 382 pages; Göttingen, Heidelberg, München, Dec. 1993

[48] I. Appenzeller, G. Rupprecht: FORS – The Focal Reducer for the VLT, ESO Messenger No. **67**, 18, 1992

[49] W. Seifert, W. Mitsch, H. Nicklas, G. Rupprecht: FORS - a workhorse instrument for the ESO-VLT, in 'Instrumentation in Astronomy VIII', SPIE Proc. **2198**, 213, 1994

[50] W. Mitsch, G. Rupprecht, W. Seifert, H. Nicklas, S. Kiesewetter, S.: Versatile multi object spectroscopy with FORS at the ESO Very Large Telescope, in 'Instrumentation in Astronomy VIII', SPIE Proc. **2198**, 317, 1994

[51] W. Seifert, W. Fürtig, H. Böhnhardt, H. Nicklas: Imaging and Spectroscopy with Focal Reducers, IAU Colloquium on 'Tridimensional Optical Spectroscopic Methods in Astrophysics', Eds. G. Comte and M. Marcelin, IAU Coll. No.**149**, ASP Conf. Series, Vol.**71**, 18, 1995

[52] H. Böhnhardt, S. Möhler, H.-J. Hess, S. Kiesewetter, H. Nicklas, H.: Design Benchmarks of the FORS Instrument for the ESO VLT, in 'Scientific and Engineering Frontiers of 8-10m Telescopes', Eds. M. Iye, T. Nishimura, Universal Academic Press, Tokyo, 1995

[53] H. Nicklas, H. Böhnhardt, S. Kiesewetter-Köbinger, W. Seifert, G. Rupprecht: Construction of the FORS Focal Reducer/Spectrographs: Status report and first test results, in 'Optical Telescopes of Today and Tomorrow', Ed. A. Ardeberg, SPIE Proc. **2871**, 1222, 1996

[54] I. Appenzeller, W. Fürtig, R. Harke, H.-J. Hess, S. Kiesewetter, B. Muschielok, H. Nicklas, W. Seifert: The FORS Instruments for the ESO VLT, ESO-Workshop on 'The Early Universe with the VLT', ESO TP No. **72**, 1996

[55] O. Stahl, W. Seifert, W. Fürtig, H. Böhnhardt, S. Kiesewetter-Köbinger, A. Reeg, H. Nicklas: Spectroscopy with FORS, Conference on 'Wide-Field Spectroscopy', Eds. Koutizas, Morgan, Vettolani, Kluwer Press, 1997

[56] I. Appenzeller, O. Stahl, S. Kiesewetter, R.P. Kudritzki, H. Nicklas, G. Rupprecht: Spectroscopy of Faint Distant Objects with FORS, in 'The Early Universe with the VLT', Ed. J. Bergeron. Berlin 1997

[57] H. Nicklas, H. Böhnhardt, W. Fürtig, R. Harke, H.J. Hess, P. Jürgens, B. Muschielok, W. Seifert, O. Stahl, K. Tarantik: Image motion and flexure compensation of the FORS spectrographs, in 'Optical Astronomical Instrumentation', Ed. S. D'Odorico, SPIE Proc. **3355**, 93, 1998

[58] T. Szeifert, I. Appenzeller, W. Fürtig, W. Seifert, O. Stahl, H. Böhnhardt, W. Gässler, R. Häfner, H.J. Hess, K.H. Mantel, W. Meisl, B. Muschielok, K. Tarantik, R. Harke, P. Jürgens, H. Nicklas, G. Rupprecht: Testing FORS – the first focal reducer for the ESO VLT, in 'Optical Astronomical Instrumentation', Ed. S. D'Odorico, SPIE Proc. **3355**, 20, 1998

[59] I. Appenzeller, K. Fricke, W. Fürtig, W. Gässler, R. Häfner, R. Harke, H.J. Hess, W. Hummel, P. Jürgens, R.P. Kudritzki, K.H. Mantel, W. Meisl, B. Muschielok, H. Nicklas, G. Rupprecht, W. Seifert, O. Stahl, T. Szeifert, K. Tarantik: Successful commissioning of FORS1 – the First Optical Instrument on the VLT, The ESO Messenger No. **94**, 1, 1998

[60] M. Dietrich, I. Appenzeller, S.J. Wagner, W. Gässler, R. Häfner, H.J. Hess, W. Hummel, B. Muschielok, H. Nicklas, G. Rupprecht, W. Seifert, O. Stahl, T. Szeifert, K. Tarantik: Spectroscopic study of high redshift quasars, Astron. & Astrophys. **352**, L1, 1999

[61] C. Möllenhoff, I. Appenzeller, W. Gässler, R. Häfner, J. Heidt, W. Hummel, B. Muschielok, H. Nicklas, G. Rupprecht, W. Seifert, O. Stahl, T. Szeifert: Morphological structure and colors of NGC 1232 and NGC 1288, Astron. & Astrophys. **352**, L5, 1999

[62] J. Heidt, K. Nilsson, I. Appenzeller, K. Jäger, W. Seifert, T. Szeifert, W. Gässler, R. Häfner, W. Hummel, B. Muschielok, H. Nicklas, O. Stahl: Observations of the host galaxies of the BL Lacertae objects H 0414+009 and OJ 287 with FORS1 at VLT-UT1, Astron. & Astrophys. **352**, L11, 1999

[63] K. Jäger, K. Fricke, I. Appenzeller, T. Szeifert, J. Heidt, W. Gässler, R. Häfner, W. Hummel, B. Muschielok, H. Nicklas, W. Seifert, O. Stahl: Imaging and spectroscopy with FORS1 in the field of Q 0307-0015, Astron. & Astrophys. **352**, L17, 1999

[64] K. Beuermann, F.V. Hessman, K. Reinsch, H. Nicklas, P.M. Vreeswijk, T.J. Galama, E. Rol, J. van Paradijs, C. Kouveliotou, F. Frontera, N. Masetti, E. Palazzi, E. Pian: VLT observations of GRB 990510 and its environment, Astron. & Astrophys. **352**, L26, 1999

[65] P. Papaderos, K. Fricke, T.X. Thuan, Y.I. Izotov, H. Nicklas: Optical studies of the blue compact dwarf galaxy Tol 65 with the VLT, Astron. & Astrophys. **352**, L57, 1999

[66] K. Jäger, J. Heidt, I. Appenzeller, R. Bender, K. Fricke & the FORS Deep-Field Team: The FORS Deep Field (FDF): Selcetion and first impressions, Astron. Ges. Abstr. Ser. **15**, 43, 1999

[67] I. Appenzeller, R. Bender, H. Böhnhardt, S. Cristiani, M. Dietrich, K. Fricke, W. Fürtig, W. Gässler, R. Gilmozzi, R. Häfner, R. Harke, J. Heidt, H.J. Hess, W. Hummel, U. Hopp, W. Hummel, K. Jäger, P. Jürgens, R.P. Kudritzki, M. Kümmel, K.H. Mantel, D. Mehlert, W. Meisl, C. Möllenhoff, B. Muschielok, H. Nicklas, A. Renzini, P. Rosati, G. Rupprecht, R. Saglia, W. Seifert, S. Seitz, J. Spyromilio, O. Stahl, T. Szeifert, K. Tarantik: Science with FORS, in 'VLT Opening Symposium', ESO Astrophys. Symp. **3**, 2000

[68] W. Seifert, I. Appenzeller, W. Fürtig, O. Stahl, E. Sutorius, W. Xu, W. Gässler, R. Häfner, H.J. Hess, W. Hummel, K.H. Mantel, W. Meisl, B. Muschielok, K. Tarantik, H. Nicklas, G. Rupprecht, C. Cumani, T. Szeifert, J. Spyromilio: Commissioning of the FORS instruments at the ESO VLT, in 'Optical and IR Telescopes Instrumentation and Detectors', Eds. M. Iye, A. Moorwood, SPIE Proc. **4008**, 96, 2000

[69] H. Schink, H. Nicklas, R. Harke, R. Häfner, H.J. Hess, W. Hummel, K.H. Mantel, W. Meisl, B. Muschielok, K. Tarantik, W. Seifert: Masking techniques at the focal plane of the FORS instruments, in 'Optical and IR Telescopes Instrumentation and Detectors', Eds. M. Iye, A. Moorwood, SPIE Proc. **4008**, 175, 2000

[70] W. Hummel, W. Gässler, B. Muschielok, H. Schink, H. Nicklas, G. Conti, D. Maccagni, S. Keller, K.H. Mantel, I. Appenzeller, G. Rupprecht, W. Seifert, O. Stahl, K. Tarantik: VLT FORS spectra of Be stars in the SMC cluster NGC 330, in 'Discoveries and Research Prospects from 8–10-Meter-Class Telescopes', Ed. J. Bergeron, SPIE Proc. **4005**, 2000

[71] I. Appenzeller, R. Bender, A. Böhm, N. Drory, K. Fricke, R. Häfner, J. Heidt, U. Hopp, K. Jäger, M. Kümmel, D. Mehlert, C. Möllenhoff, A. Moorwood, H. Nicklas, S. Noll, R. Saglia, S. Seitz, O. Stahl, E. Sutorius, T. Szeifert, S. Wagner, B. Ziegler: The FORS Deep Field, The ESO Messenger No. **100**, 44, 2000,

[72] J. Heidt, I. Appenzeller, R. Bender, A. Boehm, N. Drory, K.J. Fricke, A. Gabasch, U. Hopp, K. Jaeger, M. Kuemmel, D. Mehlert, C. Möllenhoff, A. Moorwood, H. Nicklas, S. Noll, R. Saglia, W. Seifert, S. Seitz, O. Stahl, E. Sutorius, T. Szeifert, S.J. Wagner, B. Ziegler: The FORS Deep Field, Reviews in Modern Astronomy, Vol. **14**, 209, 2001

[73] W. Hummel, W. Gässler, B. Muschielok, H. Schink, H. Nicklas, G. Conti, E. Mattaini, S. Keller, K.H. Mantel, I. Appenzeller, G. Rupprecht, W. Seifert, O. Stahl, K. Tarantik: Hα emission line spectroscopy in NGC 330 – On the hybrid model for global oscillations in Be star circumstellar disks, Astron. & Astrophys. **371**, 932, 2001

[74] P.M. Vreeswijk, A. Fruchter, L. Kaper, E. Rol, T.J. Galama, J. van Paradijs, C. Kouveliotou, R.A.M.J. Wijers, E. Pian, E. Palazzi, N. Masetti, F. Frontera, S. Savaglio, K. Reinsch, F.V. Hessman, K. Beuermann, H. Nicklas, E.P.J. van den Heuvel: VLT spectroscopy of GRB 990510 and GRB 990712; probing the faint and bright end of the GRB host galaxy population, Astrophys. Journal **546**, 672, 2001

[75] H. Böhnhardt, G.P. Tozzi, K. Birkle, O. Hainaut, T. Sekiguchi, M. Vair, J. Watanabe, G. Rupprecht & FORS Instrument Team: Visible and near-IR observations of transneptunian objects. Results from ESO and Calar Alto Telescopes, Astron. & Astrophys. **378**, 653, 2001

[76] J. Heidt, I. Appenzeller, R. Bender, K.J. Fricke & the FORS Deep-Field Team: The FORS Deep Field, Astrophys. Space Sci., Suppl. Ser. **277**, 539, 2001

[77] I. Appenzeller, D. Mehlert, S. Noll, R. Bender, A. Böhm, A. Gabasch, J. Heidt, U. Hopp, K. Jäger, M. Kümmel, S. Seitz, & the FORS Deep-Field Team: High Redshift Galaxies in the FORS Deep Field, in 'Studies of Galaxies in the Young Universe with New Generation Telescopes', (Ed.) N. Arimoto, ADS Electronic Publication, 2001

[78] R. Bender, I. Appenzeller, A. Böhm, N. Drory, K.J. Fricke, A. Gabasch, J. Heidt, U. Hopp, K. Jäger, M. Kümmel, D. Mehlert, C. Möllenhoff, A. Moorwood, H. Nicklas, S. Noll, R. Saglia, W. Seifert, S. Seitz, O. Stahl, E. Sutorius, R. Szeifert, S. Wagner, B. Ziegler: The FORS Deep Field: Photometric Data and Photometric Redshifts, Proc. ESO/ST-ECF/STScI Workshop 'Deep Fields', Eds. S. Cristiani, A. Renzini, R.Williams, ESO Astrophys. Symp. **26**, 96, 2001

[79] D. Mehlert, S. Noll, I. Appenzeller, R. Bender, S. Seitz & the FORS Deep-Field Team: The FORS Deep Field: First Spectroscopic Results, Proc. ESO/ST-ECF/STScI Workshop 'Deep Fields', Eds. S. Cristiani, A. Renzini, R.Williams, ESO Astrophys. Symp. **26**, 162, 2001

[80] M. Kümmel, J. Heidt, S. Wagner, I. Appenzeller, R. Bender, K. Fricke & the FORS Deep Field Team: Number Counts and Angular Correlation Functions in the FORS Deep Field, Proc. ESO/ST-ECF/STScI Workshop 'Deep Fields', Eds. S. Cristiani, A. Renzini, R.Williams, ESO Astrophys. Symp. **26**, 159, 2001

[81] B. Ziegler, A. Böhm, K.J. Fricke, K. Jäger, H. Nicklas, R. Bender, N. Drory, A. Gabasch, R.P. Saglia, S. Seitz, J. Heidt, D. Mehlert, C. Möllenhoff, S. Noll, E. Sutorius: The evolution of the Tully-Fisher relation of spiral galaxies, Astrophys. Journal **564**, L69-L72, 2002

[82] G.L. Israel, W. Hummel, S. Covino, S. Campana, I. Appenzeller, W. Gässler, K.-H. Mantel, G. Marconi, C.W. Mauche, U. Munari, I. Negueruela, H. Nicklas, G. Rupprecht, R.L. Smart, O. Stahl, L. Stella: RXJ0806.3+1527: a double degenerate binary with the shortest known orbital period (321s), Astron. & Astrophys. **386**, L13-L17, 2002

[83] J. Heidt, I. Appenzeller, R. Bender, K.J. Fricke & the FORS Deep-Field Team: The FORS Deep Field: Photometry, photometric redshifts and first spectroscopic results, Astrophys. Space Sci. **281**, 539, 2002

[84] J. Heidt, I. Appenzeller, A. Gabasch, K. Jäger, S. Seitz, R. Bender, A. Böhm, J. Snigula, K. J. Fricke, U. Hopp, M. Kümmel, C. Möllenhoff, T. Szeifert, B. Ziegler, N. Drory, D. Mehlert, A. Moorwood, H. Nicklas, S. Noll, R.P. Saglia, W. Seifert, O. Stahl, E. Sutorius, S. J. Wagner: The FORS Deep Field: Field selection, photometric observations and photometric catalog, Astron. & Astrophys. **398**, 49-61, 2003

[85] J. Heidt, I. Appenzeller, A. Gabasch, K. Jäger, S. Seitz, R. Bender, A. Böhm, J. Snigula, K. J. Fricke, U. Hopp, M. Kümmel, C. Möllenhoff, T. Szeifert, B. Ziegler, N. Drory, D. Mehlert, A. Moorwood, H. Nicklas, S. Noll, R.P. Saglia, W. Seifert, O. Stahl, E. Sutorius, S. J. Wagner: UBgRIJKs photometry in the FORS Deep Field (Heidt+,2003), Astron. &

Astrophys. **398**, 49H, 2003, On-line catalog availbale at CDS-service
http://cdsweb.u-strasbg.fr/cgi-bin/qcat?J/A+A/398/49

[86] J. Heidt, I. Appenzeller, A. Gabasch, K. Jäger, S. Seitz & the FORS Deep-Field Team:
The FORS Deep Field: the photometric catalogue, Astrophys. Space Sci. **284**, 385, 2003

[87] A. Böhm, B.L. Ziegler, K.J. Fricke & the FORS Deep-Field Team: Scaling relations of Field
spirals at intermediate redshift, Astrophys. Space Sci. **284**, 689, 2003

[88] J. Heidt, I. Appenzeller, S. Noll & the FORS Deep-Field Team: The QSO Q0103-260
(z=3.36) in the FORS Deep Field, Carnegie Obs. Astrophys. Ser. **1**, 2003,
http://www.ociw.edu/ociw/symposia/series/symposium1/proceedings.html

List of Abbreviations and Acronyms

AO	Active/Adaptive Optics
CCD	Charge Coupling Device
CIR	Central Intensity Ratio
DGT	Deutsches Groß-Teleskop
DLR	Deutsches Zentrum für Luft- u. Raumfahrt, Oberpfaffenhofen
DSS	Digital Sky Survey
EFOSC	ESO Faint Object Spectrograph and Camera
EMC	Electro-Magnetic Compatibility
EMMI	ESO Multi-Mode Instrument
ESO	European Southern Observatory
FDF	FORS Deep Field
FEA	Finite-Element Analysis
FORS	Focal-Reducer/Spectrograph
FOV	Field of View
FWHM	Full Width Half Maximum
GRB	Gamma Ray Burst
GTO	Guaranteed Time Observations
HDF	Hubble Deep Field
HDFN	Hubble Deep Field North
HDFS	Hubble Deep Field South
HR	High spatial Resolution imaging mode
HST	Hubble Space Telescope
IR	Infra-Red
LRU	Line Replaceable Unit
MOS	Multi Object Spectroscopy
MXU	Mask Exchange Unit
NTT	New Technology Telescope
PI	Principle Investigator
PSF	Point Spread Function
QSO	Quasi Stellar Object
RC	Ritchey-Chrétien system
RMS	Root Mean Square
SIR	Strehl Intensity Ration
SNR	Signal to Noise Ratio
SR	Standard spatial Resolution imaging mode
TBC	To Be Confirmed
TNO	Trans Neptunian Objects
USG	Universitäts-Sternwarte Göttingen
UT	Unit Telescope of the ESO/VLT
UV	Ultra-Violet
VIC	VLT Instrument Consortium
VLA	Very Large Array
VLT	Very Large Telescope

.

.

Lebenslauf

Name:	Nicklas
Vorname:	Harald
Geboren:	15. Juli 1958, in Prüm
Nationalität:	Deutsch

Ausbildung:

1964 - 1977	Grundschule und Gymnasium
1978 - 1985	Studium der Physik und Astronomie an der Friedrich-Wilhelms-Universität Bonn
1984 - 1985	Studentischer Mitarbeiter am Observatorium 'Hoher List' der Universität Bonn
1985, Mai	Physik-Diplom, Friedrich-Wilhelms-Universität Bonn

Diplomarbeit

Titel:	Astro-Spektralphotometrie mit dem *SIT-Vidicon Optical-Multichannel-Analysator-2* Detektorsystem
Universität:	Fakultät für Physik, Friedrich-Wilhelms-Universität Bonn, Mai 1985
Betreuer:	Prof. Dr. E.H. Geyer

Beruflicher Werdegang:

1985 - 1987	Wiss. Mitarbeiter an der Landessternwarte Heidelberg
seit 1988	Wiss. Mitarbeiter an der Universitäts-Sternwarte Göttingen
1985 - 1991	Projekt Wissenschaftler u. Manager in der 'Arbeitsgemeinschaft Deutsches Großteleskop' (AG-DGT) zum Nachweis der Realisierbarkeit und Begründung eines nationalen optischen Teleskops der 12-Meter Klasse für die astrophysikalische Forschung in Deutschland
1990 - 2002	Projekt-Verantwortlicher an der Göttinger Sternwarte für Design, Herstellung, Konstruktion, Test und Installation von zwei FORS *Fokal-Reduktor/Spektrographen* am 'Very Large Telescope' des Paranal Observatoriums der ESO
seit 2000	Projekt-Verantwortlicher an der Göttinger Sternwarte für Design, Herstellung, Konstruktion, Test und Installation der OMEGACAM Viertel-Giga Pixel Durchmusterungskamera am 'VLT Survey Telescope' des Paranal Observatoriums der ESO
seit 2005	Projekt-Verantwortlicher am Institut für Astrophysik der Universität Göttingen – vormals Universitäts-Sternwarte – für das 2nd Generation VLT-Instrument *Multi Unit Spectroscopic Explorer* MUSE am 'Very Large Telescope' des Paranal Observatoriums der ESO, zugleich Testlauf für die Instrumenten-Entwicklung des geplanten europäischen 100-Meter OWL *Overwhelmingly Large Telescope*